EVALUATION OF A DOPPLER SONAR SYSTEM FOR MEASUREMENTS OF FISH SWIMMING VELOCITY

CRISTINA DAWN SPANU TOLLEFSEN

EVALUATION OF A DOPPLER SONAR SYSTEM FOR MEASUREMENTS OF FISH SWIMMING VELOCITY

by

© Cristina Dawn Spanu Tollefsen

A thesis submitted to the
School of Graduate Studies
in partial fulfillment of the
requirements for the degree of
Doctor of Philosophy

Department of Physics and Physical Oceanography
Memorial University of Newfoundland

St. John's Newfoundland

Your file Votre référence
ISBN: 978-0-494-15664-3
Our file Notre référence
ISBN: 978-0-494-15664-3

Abstract

Good measurements of fish swimming velocity would add another piece of valuable scientific information to the toolkit of the fisheries acoustician; however, previous investigations of Doppler sonar measurements of fish velocity have been relatively sparse, and no previous study has explored the possibilities available with newer coherent Doppler sonar systems. Comprehensive field and laboratory studies were undertaken to characterize the performance of a 250-kHz, 10-kHz bandwidth coherent Doppler sonar when applied to measurements of fish swimming velocity. A computer model was designed to assist in understanding experimental results and broaden the range of parameters investigated. The quality of velocity estimates was quantified by calculating the error and the standard deviation for estimates of Doppler velocity for individual targets. The effect of sonar parameters (pulse length, pulse coding, lag, ping rate, bandwidth) and environmental conditions (target and water velocity, target spacing, signal-to-noise ratio) on the quality of velocity estimates was examined through four experiments with simulated fish targets, three experiments with live fish targets, and the computer model. With signal-to-noise ratio ranging from 0 dB to 75 dB, typical velocity errors of 1–2 cm s^{-1} and standard deviations of 5–13 cm s^{-1} were realized with the test instrument, amounting to 4–11% uncertainty if a fish swimming velocity of 30 cm s^{-1} is assumed. Experimental, theoretical, and model results taken together suggest that useful estimates of fish swimming velocity could be obtained using a coherent Doppler sonar with the following specifications: a transmit frequency of 200–300 kHz with a 16% bandwidth, a beamwidth of 4–6°, and several beams to measure multiple components of fish velocity.

Acknowledgements

A wise man told a group of students that the reason they got as far as they did was because of two groups of people: their families, and their teachers. And he was right.

First and foremost, thanks to my husband, Dag, for his patience and support. He was a jack-of-all trades during this journey: technical support, counsellor, personal trainer, chauffeur, caretaker, cook, dishwasher, comedian, and best friend. Right behind Dag are our families, Spanus and Tollefsens alike. I couldn't have gone this far without that fan base.

Second, thanks to my supervisor, Len Zedel. His door was always open for questions, and I could rely on him to give me and this project the necessary attention. Along with thanks to Len goes thanks to Liz, Alida, and Fern: I know he takes his work seriously and sometimes takes it home with him, and I thank you for sharing your husband/father's time with me.

Thanks to the technical support crew in various places – I believe they're terribly undervalued – without them, the field work doesn't get done: Jack Foley, Jim Gosse, Darrell Green, Andrew Kuczora, Chris Steveson, and Yunbo Xie. Thanks also to various organizations I worked with: the Institute for Ocean Technology, the Ocean Engineering and Research Centre, the Ocean Sciences Centre, and the Pacific Salmon Commission. And thanks to the financial backers of this project: the Link Foundation, NSERC, and the Petro-Canada Young Innovators Program.

Finally, thanks to my friends: Reg and Judy Cantwell; Liz, Paul, Joey, Robert, and Kathleen Ring; Rebecca Ford; Darren Hunt, Kay Lem, and Jada; Nora and Dominic Lippa; and the whole crowd at the former Cantwell's Olympic Taekwondo. It's you who made St. John's feel like home, and provided the good times which are vital to balance out the hard work.

Contents

List of Figures

List of Tables

List of Abbreviations

ADCP	-	acoustic Doppler current profiler
dB	-	decibels
fps	-	frames per second
FFT	-	fast Fourier transform
FOV	-	field of view
HTI	-	Hydroacoustic Technology, Inc.
IOT	-	Institute for Ocean Technology, formerly Institute for Marine Dynamics, St. John's, Newfoundland
ISA	-	Industry Standard Architecture
OERC	-	Ocean Engineering Research Centre, Department of Engineering, Memorial University of Newfoundland, St. John's, Newfoundland
OSC	-	Ocean Sciences Centre, Memorial University of Newfoundland, St. John's, Newfoundland
PSC	-	Pacific Salmon Commission
RDI	-	R. D. Instruments
SNR	-	signal-to-noise ratio

List of Symbols

Chapter 2

f_0, f	-	transmit frequency
f_r	-	received frequency
f_d	-	Doppler shift frequency
f_n	-	Nyquist frequency
λ_0	-	transmit wavelength
$n_\lambda, n'_\lambda, N_\lambda$	-	number of wavelengths
c	-	speed of sound in water
t	-	time
v	-	target velocity
τ	-	lag
T	-	pulse length
$W(f)$	-	spectral density
$R(\tau)$	-	covariance function
$A(\tau)$	-	amplitude of covariance function
$\phi(\tau)$	-	phase of covariance function
μ_k	-	k^{th} spectral moment
$\overline{\mu}$	-	mean spectral frequency
σ_μ^2	-	spectral width
δ_v	-	velocity estimate error
σ_v	-	velocity estimate standard deviation
σ_{vP}	-	predicted velocity estimate standard deviation (Zrnic, 1977)
R_{max}	-	maximum unambiguous range for coherent Doppler sonar
Δv	-	ambiguity velocity
w	-	signal bandwidth (Zrnic, 1977)
M	-	number of pulse pairs (Zrnic, 1977)
P_N	-	noise power per sample (Zrnic, 1977)
P_S	-	signal power per sample (Zrnic, 1977)
ρ	-	complex correlation coefficient

Chapter 3

I_{raw}	-	raw sonar intensity output
I'	-	sonar intensity with logarithmic amplifier correction
V_{in}	-	voltage input to secondary transducer during amplifier calibration
b, a_0	-	y-intercept of linear fit
m, a_1	-	slope of linear fit
$S_i, S_i', S_i'', \overline{S}$	-	quadrature or sine part of phase samples
$C_i, C_i', C_i'', \overline{C}$	-	in-phase or cosine part of phase samples
s_i	-	recombined phase samples
r_i	-	correlation between recombined phase samples
R	-	range to target
$I_{S,j}$	-	signal intensity sample
$I_{N,j}$	-	noise intensity sample
v_{slope}	-	fish velocity estimated by fitting fish position as a function of time
θ	-	angle of fish swimming direction relative to beam normal in v_{slope} model
ϕ	-	angle of fish position reative to beam axis in v_{slope} model
$\mathbf{r_{fish}}$	-	vector to fish centre from centre of transducer face
$\mathbf{r_{head}}$	-	vector to fish head from centre of transducer face
$\mathbf{r_{tail}}$	-	vector to fish tail from centre of transducer face
L	-	fish length
T_{beam}	-	target time-in-beam
v_{true}	-	true target velocity

Chapter 4

N	-	number of velocity estimates averaged for a single fish
r	-	(statistics) linear correlation coefficient for fits
R	-	(statistics) square of r for fits
F-value	-	(statistics) ratio of variance in linear term to residual variance
p-value	-	(statistics) probability of observing an F-value equal to or higher than observed, if the slope is truly zero
α	-	(statistics) level of significance
R_{mp}	-	ratio of measured to predicted standard deviation
ΔR_{min}	-	smallest resolvable target spacing
R_T	-	pulse length expressed as equivalent range

Chapter 5

BW_{Xmt} - (model) transmit bandwidth
BW_{rec} - (model) receive bandwidth
f_m - (model) sampling frequency of modelled pulse
Δt_m - (model) model timestep ($1/f_m$)
f_s - (model) final sampling frequency
Δt_s - (model) final sampling interval
n_p - (model) number density of weak targets
O_{filt} - (model) filter order
n_rep - (model) number of model repetitions
$s(t_i)$ - (model) transmit pulse template
A_{rel} - (model) relative amplitude of weak targets and strong targets
$S(t)$ - (model) backscattered pulse
S_{rect} - (model) rectified backscattered pulse
S_{dB} - (model) backscatter intensity
$I(t)$ - in-phase component of a received signal
$Q(t)$ - quadrature component of a received signal
v_A - velocity calculated using analog demodulation
v_D - velocity calculated using digital demodulation
M_{eff} - effective number of independent samples in broadband water model
BW_{eff} - effective bandwidth in broadband water model
σ_{vT} - target velocity standard deviation
v_{target} - target velocity
v_{water} - water velocity
σ_{vW} - water velocity standard deviation
Δ_R - distance between modelled strong targets
$n_{samples}$ - number of samples in one transmit pulse length
ρ_{fish} - correlation coefficient for fish
ρ_{water} - correlation coefficient for water

Chapter 6

V_s - sample volume
ϕ - full beam angle (-3 dB)
δ_R - spatial sampling interval
f_s - sampling frequency
N_F - characteristic fish density
$r(\tau)$ - autocorrelation (Zrnic, 1977)
ω_0 - mean angular frequency (Zrnic, 1977)
$\delta_{\tau,0}$ - Dirac delta function
v_T - tail velocity
f_W - frequency of fish 'wiggling' motion
f_{DT} - additional Doppler shift due to tail motion
ϵ - total uncertainty in Doppler velocity measurement
H_{ext} - horizontal extent between opposing sonar beams
V_{ext} - vertical extent of measurements made with opposing sonar beams
F_{fish} - fish per unit time passing through a sample volume
A - area of sample volume
$v_\perp$ - velocity perpendicular to beam direction
N - number density of fish
PRF - pulse repetition frequency
F_{time} - number of fish observed per unit time

Chapter 1

Introduction

1.1 Motivation

Acoustics provides a powerful tool for probing processes in the ocean which would otherwise be invisible, since light does not penetrate significantly into salt water (Medwin and Clay, 1998). Ocean acousticians use passive (receive only) or active (transmit and receive) sonar techniques for observing the ocean. The scatter observed using an active sonar will contain information about the location and size of the target which is the scattering source. In addition, measuring the Doppler frequency shift of scattered sound can provide an estimate of target velocity.

Scatter of transmitted sound in the ocean can arise from particles passively moving at the water velocity, solid targets such as fish, the ocean surface, or the ocean bottom. Physical oceanographers have exploited acoustic Doppler techniques to study a variety of ocean processes: surface waves (Smith, 1989), internal waves (Pinkel et al., 1987; Pinkel and Smith, 1987), sediment transport (Zedel et al., 1995; Zedel et al., 1996;

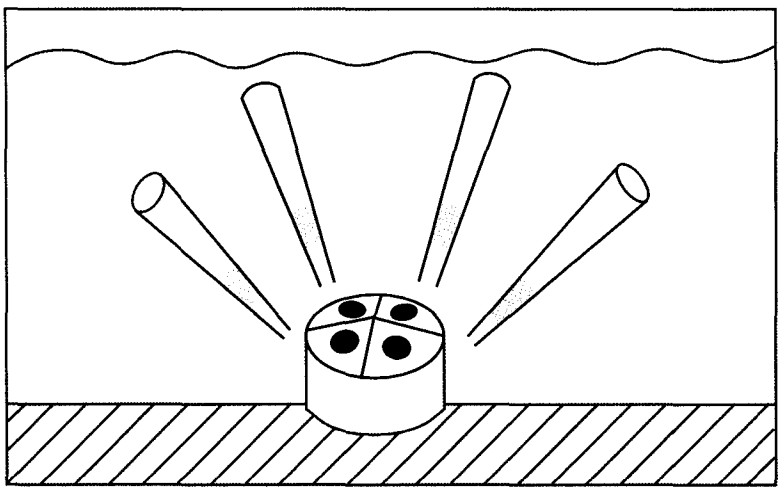

Figure 1.1: Diagram of an acoustic Doppler current profiler (ADCP). A typical ADCP has four beams inclined at 20° or 30° to the vertical, at increments of 90° in the azimuth, as shown. The grey part of the beam illustrates a range bin created by gating the returned signal.

Zedel and Hay, 1999), turbulence (Lhermitte and Lemmin, 1990), and most commonly, current velocities (Lhermitte, 1983; Lhermitte and Serafin, 1984; Pinkel, 1986; Theriault, 1986; Bugnon and Whitehouse, 1991; Pinkel and Smith, 1992; Trevorrow and Farmer, 1992). Doppler sonar current measurement is now so widespread that a number of companies produce sonars specifically designed to measure current velocity, such as RD Instruments' acoustic Doppler current profilers (ADCPs, shown schematically in Figure 1.1), and Sontek's acoustic Doppler velocimeters (ADVs) and acoustic Doppler profilers (ADPs), most of which are capable of being deployed for long-term, stand-alone current measurements.

While the physical oceanographers were developing instruments optimized for the study of physical phenomena, fisheries biologists developed the field of fisheries acoustics, in which observations of acoustic backscatter originating from fish or zooplankton

are collected. In a typical fisheries acoustics survey a sonar is mounted on a ship which undertakes a prescribed survey pattern in the area of interest. The echoes recorded by the sonar can be used to provide a biomass estimate for the entire area surveyed (MacLennan and Simmonds, 1992).

There are, however, drawbacks to the standard fisheries survey procedure: a research vessel is expensive to operate, and a single survey will require days to weeks of ship time, resulting in spatial and temporal coverage that is sparse at best. Furthermore, fisheries biologists generally only measure where the fish *are*, and not where they are *going*. Although in many cases it is sufficient to know only the fishes' location, there are times when their movement is of interest, be it diurnal or seasonal migration (Benoit-Bird and Au, 2002), movement in response to human activity (Slotte et al., 2002), or even an avoidance response when observing fish with a ship-mounted sonar (Olsen et al., 1983). In addition, fish movement can bias biomass estimates (MacLennan and Simmonds, 1992); although a well-designed survey should minimize the resulting bias, unknown movement may inadvertently introduce bias which would be difficult if not impossible to detect. Therefore, it would be useful in some cases for fisheries biologists to have a tool to accurately determine the velocity of swimming fish, and to do so not from a vessel but from a stationary long-term mooring, resulting in a time series of fish swimming behaviour in a given location, rather than a 'snapshot' of their spatial distribution at some particular time.

Fisheries sonars which can measure fish velocity without making use of Doppler techniques already exist but their measurement capabilities are limited. A single-beam sonar with a relatively narrow beam could be used to measure a single component of fish swimming velocity by differentiating the range to the fish as a function of

time. However, large velocity errors can result from differentiating fish position in all but very specific cases (see Section 3.5.3). A split-beam sonar can be used to track the location of a target in three dimensions and derive fish velocity by differentiating fish position as a function of time (e. g. Xie et al. 1997, Xie et al. 2002). Split-beam sonar velocity measurements are generally accurate when made in 'high' signal-to-noise ratio (SNR) environments (SNR $>$ 20 dB); however, in low-SNR environments, the measured fish position can be severely biased toward the beam axis, resulting in significant errors in fish velocity estimation (Kieser et al., 2000). Therefore, measurement of velocity by differentiation of position with either single-beam or split-beam sonars will only provide accurate measurements under limited conditions.

Doppler techniques, however, have the potential to provide accurate measurements of fish velocity under a wide variety of conditions, and implementing the Doppler approach in a stationary long-term moored instrument would result in an improvement in temporal coverage by providing a time series of fish 'traffic' in and out of a given area. A sonar optimized for Doppler measurements of fish velocity would provide a useful alternative to multiple ship-based surveys; however, this approach has never been given serious consideration before in the field of fisheries acoustics, which is surprising since similar oceanographic instruments (e. g. ADCPs) already exist. This thesis will explore the optimization of instrument hardware and signal processing specifically for measurements of individual fish swimming velocity.

1.2 Previous work

Two types of Doppler shifts can be associated with swimming fish: observation from the side aspect will result in the measurement of the tailbeat frequency, while observation from the nose or tail aspect will result in the measurement of the swimming velocity. The latter is the more intuitive measurement, although a careful laboratory experiment by Bainbridge (1958) related the swimming speed of a fish to the frequency and amplitude of the tailbeat. It should be easier to measure swimming velocity than tailbeat frequency for fish with swim bladders, since the bulk of the backscatter from a fish arises from the air-filled swim bladder. However, lack of a swim bladder would not preclude the use of the Doppler technique; the signal-to-noise ratio would simply be lower than for a fish with a swimbladder.

Doppler sonar has been used from time to time in fisheries acoustics to study the motion of fish or fish schools, but has never been widely accepted. Previous experiments fall into three categories: one-time experiments designed for very specific circumstances, experiments in rivers where some uniformity in fish swimming direction is expected, and experiments involving commercial ADCPs.

1.2.1 First experiments

The earliest use of Doppler sonar for observations of fish motion was that of Hester (1967), who identified three classes of targets from different types of Doppler shifts. Using a 70-kHz sonar with a high-resolution frequency analyzer, targets were classified as stationary (no Doppler shift), targets that showed gross motion (narrow-band Doppler shift), or targets that showed complex motion (broadband Doppler shift).

Using the relationship among fish swimming speed, tailbeat frequency, and tailbeat amplitude developed by Bainbridge (1958), the size of the detected fish was estimated from the broadband Doppler shift which was presumed to originate from the undulatory motion of the fish bodies.

Holliday (1974, 1977) measured both the side- and tail-aspect Doppler shifts from a fish school. An 11-kHz sonar was first used to localize the fish school, and a relatively long (0.5-s) pulse was used to insonify the school for the measurement of the Doppler shift. The relative motion between the water and the ship was determined through the Doppler shift of the volume backscatter. The tailbeat frequency was related to fish length (Bainbridge, 1958), while the tail-aspect Doppler shift was related to swimming speed and compared favourably with observations of the overall motion of the school. Holliday's work showed in a broad sense that fish velocity can be measured with a Doppler sonar, but highlighted the need for better spatial resolution.

Olsen (1983) observed the Doppler shift of a fish school during passage of a vessel to confirm that the school was moving downwards, away from the ship. Plueddemann (1989) observed the diel migration of a sound scattering layer with a Doppler sonar, and compared the Doppler velocity with that calculated by differentiating the position of the sound-scattering layer over time. The two velocities agreed within $\pm 25\%$, demonstrating the validity of technique, considering that the observed velocities were quite low (1–5 $\mathrm{cm\,s^{-1}}$). It was noted that if a only a small proportion of scatterers in a sample volume are moving, the Doppler shift velocity will be biased toward zero; however, this is not expected to be a problem when observing fish, which are much stronger scatterers than the sound scattering layer observed by Plueddemann in this context.

1.2.2 Riverine experiments

At first glance, the use of Doppler sonars in riverine applications seems straightforward and perhaps simpler than open-ocean applications. Most of the fish are travelling in the same direction, because experiments are usually performed in rivers where anadromous species are returning to their birthplace to spawn. The geographical constraints imposed by a river also make it far easier to count each individual fish as it swims upstream. However, rivers can be problematic acoustic environments: minimizing surface and bottom reflections from the main beam and sidelobes can be difficult, and there is often substantial debris being carried downstream which may introduce unwanted strong scatterers into the detected signal. The challenges of making shallow-water acoustical measurements can thus result in noise obscuring the Doppler measurements.

Pincock and Easton (1978) considered the parameters necessary for a sonar to detect tail-beat Doppler shifts in a river. They developed two sets of parameters which would work for fish detection: a continuous wave Doppler sonar (30–100 kHz), which offers no spatial resolution but would still detect the presence or absence of fish; and a pulsed Doppler sonar, which would require a higher transmit frequency (1 MHz) to provide greater power, and thus would only be suitable for a narrow channel (a few metres wide). Hendershot et al. (1984) used a 420-kHz incoherent bistatic system with a spatial resolution of 10 m and target ranges from 3–25 m to assist in fish counting. Stationary targets (the river bottom) and targets moving downriver (water) were excluded from the fish count by filtering the Doppler return. Targets moving upstream were assumed to be fish and added to the fish count, while no use was made of the measurements of fish velocity itself. Waite and Belcher (1985)

designed a detection algorithm using a 420-kHz Doppler sonar system which averaged multiple estimates of the velocity to determine whether or not a target was a fish. Again the Doppler information was merely used to identify and count fish targets, and then discarded. Johnston and Hopelain (1990) used a similar technique to count fish targets using Doppler sonar, and counted only upstream-moving targets as fish. They admitted that the Doppler system as designed would likely count some fish twice, as the fish were observed to be milling and the Doppler system was designed under the assumption that downstream-moving targets were not fish. The riverine Doppler approach failed to become popular and has, for the most part, been abandoned by fisheries sonar manufacturers.

1.2.3 ADCP experiments

Commercial ADCPs intended for ocean current measurement have been used by a few investigators to measure fish velocity. Current velocities measured by ADCPs can be biased by the presence of fish or zooplankton (Hansen, 1986; Freitag et al., 1992; Wilson and Firing, 1992; Plimpton et al., 1997), which suggests the possibility of using ADCPs specifically to measure fish velocity. However, ADCPs are optimized for detecting Doppler shifts from volume backscatter rather than solid targets. They are also designed with fish-rejection algorithms to reduce the errors introduced by fish in the beams (Plimpton et al., 1997); therefore, attempts to measure fish velocity with ADCPs have had limited success.

Demer et al. (2000) used a 150-kHz RDI broadband ADCP to observe fish schools and measure nearby current velocities, and identified the conditions under which such observations would be successful: the fish school must have a large enough

horizontal extent to encounter at least three of the four beams, the school must be moving homogeneously, the velocities of the school must exceed the ADCP precision, and the relative ship and water movement must be quantifiable in order to measure fish swimming velocity relative to the water. Zedel and Knutsen (2000) reported a velocity standard deviation of 10 $\mathrm{cm\,s^{-1}}$ in towtank tests of a 300-kHz ADCP and found that single solid targets were identifiable in the data, although complex target arrangements caused some measurement problems. A field test (Zedel et al., 2003) of ADCP observations of large schools of herring showed in principle that fish velocities could be successfully measured. The observed velocity variance was greater than that predicted theoretically, and it was inferred that fish movement was probably the source of the increase in variance. In both experiments (Zedel and Knutsen, 2000; Zedel et al., 2003) a desire for better spatial resolution was expressed (20 cm was the limit imposed by the RDI ADCP firmware for the 300-kHz ADCP used in the experiments).

Problems with ADCP measurements arise from the fact that unless it is carefully configured, an ADCP tends to discard data which is of poor quality in the context of current measurement, although the same data would be useful for fish velocity measurement. For example, the fish-rejection algorithm compares the differences in backscatter intensities observed between beams to a threshold and rejects velocity data if the threshold is exceeded; the assumption is that fish are contaminating the water velocity measurement in one or more beams. Another restriction is that the scattering layer is expected to move homogeneously, which is implemented by calculating the 'error velocity' (the difference between the two vertical velocity estimates for each ping). Velocity data are rejected if the error velocity exceeds a

user-defined threshold. Both the fish-rejection and error-velocity algorithms can be disabled; however, the default settings are not conducive to fish velocity measurement. Furthermore, the assumption of a uniform scattering layer for velocity reconstruction is not valid in general for swimming fish. An instrument designed specifically for the measurement of fish velocity would not be subject to the restrictions which are an essential component of the ADCP's basic design.

1.2.4 Weaknesses in previous work

All the earlier attempts at fish velocity measurement with Doppler sonar have certain weaknesses in common. First, none have exploited coherent processing, widely used in ADCPs and described in detail in Chapter 2, to reduce uncertainties in velocity estimates. The experiments using commercial ADCPs (Demer et al., 2000; Zedel and Knutsen, 2000; Zedel et al., 2003) implicitly make use of coherent processing but the user has no control over its implementation; the commercial ADCP is essentially a 'black box' which provides velocity data. Second, much of the work has focussed on fish schools and their gross motion, rather than individual fish swimming velocity, with the exception of the riverine work. However, the individual fish swimming velocity measured by the Doppler sonars in riverine applications was merely used for fish identification and then discarded! Third, previous authors were not considering the possibility of developing a new instrument particularly suited to measurements of fish swimming velocity, so there is a lack of thorough investigation of the limitations and advantages of Doppler processing. Fourth, the focus has remained on ship-based surveying, and so immediately discounts one of the inherent advantages possible with Doppler sonars, that of independent long-term deployments.

This thesis is based on experimental work with a test instrument which has the potential to improve upon previous work in all of the above areas. First, the test instrument is a coherent Doppler sonar. Second, the swimming velocity of individual fish rather than schools will be measured. Third, the sonar will be subject to a variety of tests in different measurement conditions to fully explore its capabilities. Finally, all the testing and signal processing has been developed keeping in mind the goal of independent long-term deployment.

1.3 Objectives

Despite the utility of the Doppler technique in medicine, weather radar, and oceanography, it has not been subjected to a thorough investigation specifically for measurements of fish velocity. The primary goal of this thesis is to address the need for a full systematic evaluation of the performance of a Doppler sonar under a variety of conditions. It will then be possible to determine the conditions under which a Doppler sonar could make reliable and useful measurements of fish swimming velocity.

There are several fundamental differences between Doppler measurement of velocities of single solid targets (e. g. fish) and a diffuse collection of weak scatterers (e. g. blood flow, atmospheric phenomena, ocean currents). First, the primary model for most theoretical Doppler work has been volume backscatter, consisting of many weak targets throughout a sample volume with a mean and standard deviation in velocity. There is no reason to expect that the statistical behaviour of the Doppler shift from a single strong target would be the same as that of volume backscatter, and comparisons with theory should provide some insight into any differences between the two

types of scattered signals. Second, the extensive range and time averaging used in all Doppler current profilers is inappropriate for discrete targets such as fish, which have a finite residence time in the sonar beam and are often smaller in spatial extent than the averaging interval. Without a purpose-built sonar it is often difficult to extract raw data; however, the test instrument (described in detail in Section 3.1) will allow for much more control over sonar parameters and in particular will allow access to the raw, unaveraged data, to allow for manipulation in any number of different ways. Third, a variety of pulse transmit and processing options exist for Doppler shift estimation (Section 2.3) and those appropriate for current velocity measurement may not be useful for the measurement of individual fish swimming velocity.

Both experimental and modelling approaches were employed in the investigation of the performance of the Doppler sonar. First, a series of laboratory and field experiments served to explore the capabilities of the test instrument. Then, a computer model of Doppler sonar operation was designed to reproduce experimental results, to ascertain that the operation of the sonar is reasonably well understood, and to allow for the exploration of some sonar parameters beyond what was possible with the test instrument.

Finally, after consideration of all the parameters affecting fish velocity measurement, it should be possible to propose the geometry, sonar parameters, and signal processing appropriate to fish velocity measurement. An examination of the advantages, disadvantages, and trade-offs among various parameters will result in an understanding of the parameters appropriate for a real system intended for a long-term deployment, capable of measuring a time series of fish velocities at a fixed spatial location, which is the goal of this research.

1.4 Outline

The remainder of this thesis will be organized as follows. In Chapter 2, the theoretical basis for Doppler shift measurement is outlined, and different types of signal transmission and associated signal processing are discussed. In Chapter 3, the test instrument, data processing, and experimental details are described. In Chapter 4, experimental results are presented. In Chapter 5, the results of the computer model are presented and compared with experimental results where possible. In Chapter 6, the experimental and model results are summarized, key findings are explained, and the implications for practical instrument design are discussed. In Chapter 7, the work is summarized, and suggestions for future work are outlined.

Chapter 2

Theory

2.1 The Doppler effect

The acoustic Doppler effect occurs when an object radiating sound of frequency f_0 has a component of relative motion toward or away from a receiver. The result is a frequency shift f_d observed by the receiver which is determined by the relative velocity between source and receiver. Therefore, measurements of the frequency shift can be inverted to find unknown velocities between sound sources and receivers.

2.1.1 Doppler frequency shift

Following the development presented by Rickey (2000), consider a monostatic transducer (the same transducer both transmits and receives sound) radiating sound of frequency f_0, and a target in its beam, as shown schematically in Figure 2.1a. The

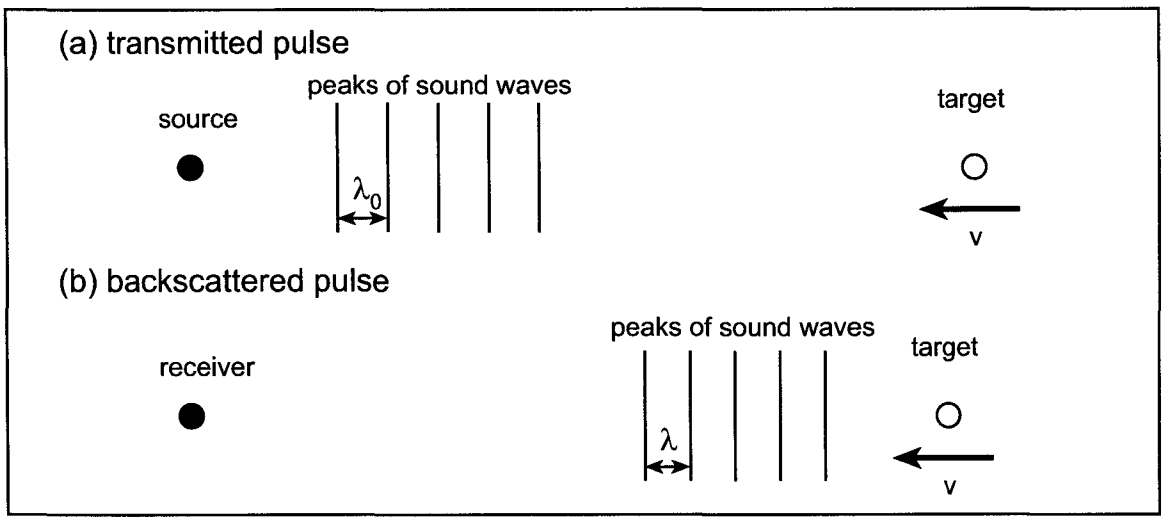

Figure 2.1: Diagram of Doppler shift geometry for a monostatic transducer. (a) The source (•) transmits sound of wavelength λ_0, which scatters off a moving target (○). (b) The moving target then scatters sound of wavelength λ back toward the source, which acts as receiver.

transmit frequency is related to the wavelength λ_0 and speed of sound c by

$$f_0 = \frac{c}{\lambda_0}$$

A stationary target will observe a number of wavelengths n_λ in a time t:

$$n_\lambda = \frac{ct}{\lambda_0}$$

while a target moving toward the transducer will move a distance vt in a time t and observe n'_λ 'extra' wavelengths

$$n'_\lambda = \frac{vt}{\lambda_0}$$

The total number of wavelengths N_λ observed by the target is then the sum of n_λ and n'_λ,

$$N_\lambda = \frac{t(c+v)}{\lambda_0}$$

The number of wavelengths per unit time N_λ/t gives the frequency f observed by the target:

$$f = \frac{(c+v)}{\lambda_0} \tag{2.1}$$

The sound has now reached the moving target and from the target's point of view has a frequency $f > f_0$ (in the case of motion toward the transducer). The sound is scattered from the target and some of the scattered sound will reach the transducer, as shown in Figure 2.1b. The distance the sound must travel during time t is reduced if the target is moving in the same direction as the sound propagation; therefore, the wavelength of radiated sound will not be $\lambda = c/f$ but

$$\lambda = \frac{(c-v)}{f}$$

The frequency f_r of the sound received by the transducer is then

$$f_r = \frac{c}{\lambda} = \frac{fc}{(c-v)} \tag{2.2}$$

Combining the equations for frequency shift for a stationary transducer and moving target (Equation 2.1), and frequency shift for a radiating target and stationary receiver (Equation 2.2) results in the expression relating the received frequency f_r and the transmitted frequency f_0:

$$f_r = f_0 \frac{(c+v)}{(c-v)} \tag{2.3}$$

In oceanographic acoustics, the speed of the objects we are interested in observing is typically 1–2 $\mathrm{m\,s^{-1}}$, while the speed of sound c is approximately 1500 $\mathrm{m\,s^{-1}}$. Therefore, the Doppler relation in Equation 2.3 is approximated using a Taylor expansion ($(1 \pm x)^n = 1 \pm nx + \frac{n(n-1)}{2!}x^2 + ...$). Beginning with a rearrangement of Equation 2.3,

$$f_r = f_0 \frac{(1 + \frac{v}{c})}{(1 - \frac{v}{c})} \tag{2.4}$$

the denominator can be approximated as

$$(1 - \frac{v}{c})^{-1} \approx 1 + \frac{v}{c} + O((\frac{v}{c})^2)$$

since $\frac{v}{c} \ll 1$. Substituting into Equation 2.4, expanding, and keeping terms of order less than $(\frac{v}{c})^2$ results in the following approximation, accurate to $\left(\frac{v}{c}\right)^2$, or 1×10^{-6} when $v = 1$ $\mathrm{m\,s^{-1}}$ and $c = 1500$ $\mathrm{m\,s^{-1}}$:

$$f_r = f_0(1 + \frac{2v}{c}) \tag{2.5}$$

Finally, by considering the received frequency f_r to be the sum of the transmit frequency f_0 and a Doppler shift frequency f_d, which may be positive or negative, Equation 2.5 can be written in the common form

$$f_d = f_0 \frac{2v}{c} \tag{2.6}$$

2.2 Mean frequency estimation

The previous section leads to the question: how is the frequency shift estimated? Furthermore, how reliable are the estimates, and under what circumstances are they reliable?

At first glance, it might seem sensible to estimate the Doppler shift by first estimating the spectrum of the backscattered signal using a Fourier transform, and then determining the mean frequency. In the early days of Doppler shift estimation (Sirmans and Doviak, 1973), Fourier transforms were computationally expensive. With the increasingly widespread use of the fast Fourier transform (FFT) algorithm beginning in the late 1960s, it was possible to implement Fourier transforms in hardware. However, the storage of all the data points necessary to perform the transform still presented a problem, and the FFT method (and spectral methods in general) also requires a tradeoff between range resolution and frequency resolution. In the present application, only the mean frequency of the spectrum (and perhaps the spectral width) is of interest, in which case the entire spectrum need not be calculated. By exploiting the relationship between the covariance of a function and the moments of its spectrum, the calculation of the spectrum can be circumvented while still providing an estimate of the mean Doppler frequency shift and spectral width (Levin, 1965; Miller and Rochwarger, 1970a; Miller and Rochwarger, 1970b; Miller and Rochwarger, 1972). The technique developed here is thus referred to as the covariance technique, and follows the development by Miller and Rochwarger (1972) .

Consider a random process with covariance function $R(\tau)$ (also referred to as the correlation or autocorrelation function) and spectral density $W(f)$. The covariance

function and spectral density form a Fourier transform pair, that is,

$$R(\tau) = \int_{-\infty}^{\infty} W(f) e^{i2\pi f\tau} df \tag{2.7}$$

$$W(f) = \int_{-\infty}^{\infty} R(\tau) e^{-i2\pi f\tau} d\tau \tag{2.8}$$

The spectral density is the probability distribution for the frequency; therefore, the k^{th} moment μ_k of the spectrum is given by

$$\mu_k(W) = \frac{\int_{-\infty}^{\infty} f^k W(f) df}{\int_{-\infty}^{\infty} W(f) df} \tag{2.9}$$

The key to relating the moments of the spectrum to the covariance function lies in the derivatives of the covariance function. The n^{th} derivative of Equation 2.7 is:

$$\frac{\partial^n R(\tau)}{\partial \tau^n} = \int_{-\infty}^{\infty} (-i2\pi f)^n W(f) e^{-i2\pi f\tau} df \tag{2.10}$$

The moments of interest for Doppler sonar are usually the first moment, giving the mean frequency $\overline{\mu}$, and the second moment, needed to calculate the spectral width $\sigma_\mu^2 = \overline{\mu^2} - \overline{\mu}^2$. Evaluation of the covariance and its first and second derivatives $\dot{R}(\tau)$ and $\ddot{R}(\tau)$ at lag $\tau = 0$ results in the moments of $W(f)$:

$$R(0) = \int_{-\infty}^{\infty} W(f) df \tag{2.11}$$

$$\dot{R}(0) = -i2\pi \int_{-\infty}^{\infty} f W(f) df \tag{2.12}$$

$$\ddot{R}(0) = -4\pi^2 \int_{-\infty}^{\infty} f^2 W(f) df \tag{2.13}$$

Rearrangement of Equations 2.9, 2.11, 2.12, and 2.13 results in relationships among the covariance and its derivatives, the mean frequency, and the spectral width:

$$\mu_1(W) = \frac{1}{i2\pi}\frac{\dot{R}(0)}{R(0)} \tag{2.14}$$

$$\sigma_\mu^2(W) = -\frac{1}{4\pi^2}\left[\frac{\ddot{R}(0)}{R(0)} - \left(\frac{\dot{R}(0)}{R(0)}\right)^2\right] \tag{2.15}$$

The covariance function is in general complex and can expressed in polar form as

$$R(\tau) = A(\tau)e^{i2\pi\phi(\tau)} \tag{2.16}$$

in which $A(\tau)$ is a real, even function of τ and $\phi(\tau)$ is a real, odd function of τ. The first and second derivatives of Equation 2.16 are

$$\dot{R}(\tau) = \left[\dot{A}(\tau) + i2\pi A(\tau)\dot{\phi}(\tau)\right] e^{i2\pi\phi(\tau)} \tag{2.17}$$

$$\ddot{R}(\tau) = \left[\ddot{A}(\tau) + i4\pi\dot{A}(\tau)\dot{\phi}(\tau) + i2\pi A(\tau)\left(\ddot{\phi}(\tau) + i2\pi\left(\dot{\phi}(\tau)\right)^2\right)\right] e^{i2\pi\phi(\tau)} \tag{2.18}$$

We are interested in Equations 2.17 and 2.18 evaluated at $\tau = 0$ for use in Equations 2.14 and 2.15. $\dot{A}(0) = 0$ since $A(\tau)$ is real and even, while $\phi(0) = 0$ since $\phi(\tau)$ is real and odd. Using similar arguments, it can be shown that $\ddot{R}(0) = 0$. Therefore, Equations 2.17 and 2.18 evaluated for $\tau = 0$ result in

$$\dot{R}(0) = A(0)i2\pi\dot{\phi}(0) \tag{2.19}$$

$$\ddot{R}(0) = \ddot{A}(0) - 4\pi^2 A(0)\left(\dot{\phi}(0)\right)^2 \tag{2.20}$$

By applying the simplifications for $\dot{R}(0)$ and $\ddot{R}(0)$ to Equations 2.14 and 2.15, we have

$$\mu_1(W) = \dot{\phi}(0) \tag{2.21}$$

$$\sigma_\mu^2(W) = -\frac{1}{4\pi}\frac{\ddot{A}(0)}{A(0)} \tag{2.22}$$

A first-order approximation for the derivative in Equation 2.21, for small values of $\tau \neq 0$, is

$$\mu(W) \approx \frac{\phi(\tau) - \phi(0)}{\tau} \approx \frac{\phi(\tau)}{\tau} \tag{2.23}$$

since $\phi(0) = 0$. The phase angle $2\pi\phi(\tau)$ of the covariance function is simply the argument of $R(\tau)$,

$$\phi(\tau) = \frac{1}{2\pi}\tan^{-1}\frac{\mathrm{Im}R(\tau)}{\mathrm{Re}R(\tau)} ;$$

therefore, the mean frequency $\mu(W)$ is

$$\mu(W) = \frac{1}{2\pi\tau}\tan^{-1}\frac{\mathrm{Im}R(\tau)}{\mathrm{Re}R(\tau)} \tag{2.24}$$

Finally, combining the Doppler relation (Equation 2.6) and Equation 2.24 for the mean frequency, we have

$$v = \frac{c}{4\pi f_0}\frac{1}{\tau}\tan^{-1}\frac{\mathrm{Im}R(\tau)}{\mathrm{Re}R(\tau)} \tag{2.25}$$

where v is the velocity of the target, c is the speed of sound in water, f_0 is the transmit frequency, τ is a time lag, and $R(\tau)$ is the covariance function.

In practice, there are several ways of applying Equation 2.24 to the extraction of the mean frequency shift. Incoherent sonars follow the phase evolution of the

backscatter from a single narrowband pulse. In contrast, coherent sonars maintain phase coherence between successive transmit pulses and calculate the phase shift at a lag equal to the time between pulses: this technique is known as the pulse-pair method of mean frequency estimation. The various methods of applying Equation 2.24 will be discussed in detail in Section 2.3.

Miller and Rochwarger (1970a, 1970b, 1972) examined Gaussian signals in both white noise and coloured noise to determine the properties of the mean frequency estimator given in Equation 2.24. In these cases the mean frequency estimator is (statistically) unbiased as the number of samples, the averaging time, or the signal-to-noise ratio (SNR) increase. In contrast, estimates of both the spectral width and the spectrum itself are biased regardless of number of samples or averaging time.

Zrnic (1977) examined the performance of the pulse-pair (coherent) method in detail, again considering a Gaussian spectrum in additive white noise. Since a coherent system is sampled at a frequency $f_s = 1/\tau$, where the lag τ is the time between pulses, frequencies higher than the Nyquist frequency $f_n = 1/2\tau$ are aliased into the frequency interval $[-1/2\tau, 1/2\tau]$. If the spectrum being examined is too wide relative to the Nyquist frequency, the aliasing will cause an increase in the variance of the mean frequency estimate (in practice this occurs when the spectral width w satisfies $w\tau > 0.25$).

The success of the pulse-pair method for Doppler velocity estimation depends on the specific application, and in particular the geometry, the type of scatterers, and the type of motion being observed. It has seen extensive use in Doppler weather radar (Sirmans and Doviak, 1973; Zrnic, 1977; Sachidananda and Zrnić, 2000), Doppler ultrasound measurements of blood flow (Barber et al., 1985), and measurements of

water velocity in physical oceanography (Lhermitte, 1983; Lhermitte and Serafin, 1984; Hansen, 1986; Brumley et al., 1987; Pinkel et al., 1987; Pinkel and Smith, 1987; Lhermitte and Lemmin, 1990; Brumley et al., 1991; Zedel et al., 1996; Zedel and Hay, 1999).

Apart from the covariance technique, other methods exist for computation of the mean frequency shift, including autoregressive models (Hansen, 1986; Ahn and Park, 1991), Fourier transform techniques (Sachidananda and Zrnić, 2000), and alternative sampling strategies (Peretto et al., 2001). Time-domain correlation (Foster et al., 1990) has been applied to oceanographic measurements (Bradley et al., 1991; Sutton and Jaffe, 1992) with some success. However, the covariance method has remained the preferred method for calculating the mean frequency shift.

One potential drawback with the pulse-pair method is that, although it works well with symmetric spectra, results can be unreliable when spectra are asymmetric or multimodal (Hansen, 1986; Lagö, 1999). There is no way of knowing *a priori* the symmetry properties of the spectrum for fish targets, but the potential for problems arising from spectral asymmetry should be kept in mind.

The size of the Nyquist interval $[-1/2\tau, 1/2\tau]$ is another source of potential problems. The spectrum from a single strong scatterer is unlikely to be wide compared with the Nyquist interval; however, aliasing will occur if the scatterer is moving faster than the so-called ambiguity velocity Δv (resulting from substitution of the Nyquist frequency into the Doppler relation, Equation 2.6):

$$\Delta v = \frac{c}{4 f_0 \tau} \tag{2.26}$$

Another way to look at the ambiguity velocity is that the measured phase must lie in the interval $[-\pi, \pi]$, and if the target moves farther than $\lambda_0/4$ between pulses, the measured phase will differ from the true phase by a factor of $\pm 2\pi$. Therefore, the lag must be carefully chosen for a given transmit frequency, so that the ambiguity velocity is greater than the velocities expected in a particular experiment.

Much of the work on the estimation of Doppler shifts using the pulse-pair method has focussed on models involving many small scatterers in a sample volume. It is not immediately clear that the theoretical results are applicable to a volume in which one very strong scatterer dominates the returned signal. The approach to mean frequency estimation is somewhat different with diffuse scatterers, as well: extensive averaging takes place in both the range and time domains, which is inappropriate for discrete targets with only a short residence time in the beam. Therefore one of the aims of this thesis is to determine how well the pulse-pair method works for speed estimation of extended solid targets, and to what extent current measurement techniques can or cannot be translated into the context of fish speed measurement.

2.3 Doppler sonar in oceanography

In any sonar, a transducer transmits an acoustic pulse into the water, and then records the backscattered sound as a function of time. Backscatter from more distant ranges will take longer to return to the transducer; therefore, time-gating the received signal will provide backscatter information as a function of range. Three basic approaches to Doppler sonar pulse transmission and processing exist: incoherent, coherent, and independent pulse-pair processing. In an incoherent sonar, Doppler velocity estimates

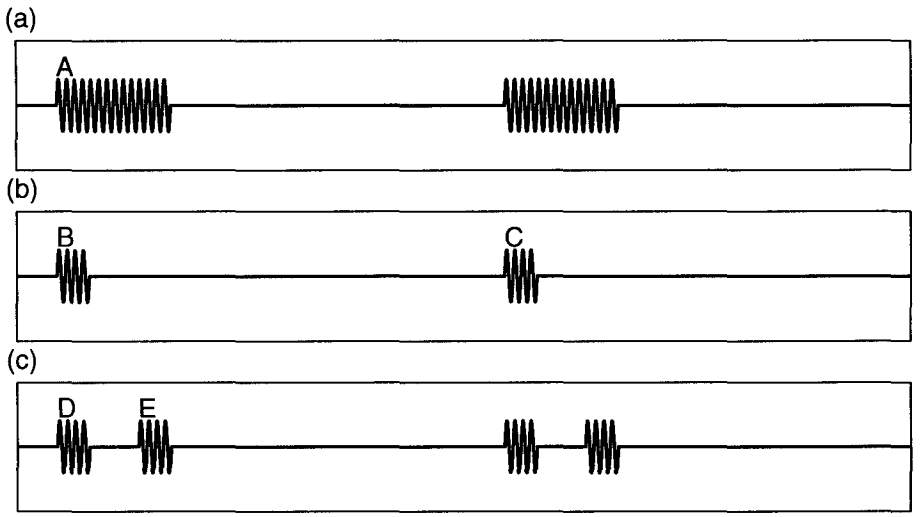

Figure 2.2: Overview of pulse processing schemes (a) Two incoherent pulses, (b) Two coherent pulses, (c) Two pairs of pulses.

are formed by observing the phase evolution of each backscattered pulse, independent of other pulses. In a coherent sonar, phase coherence is maintained between successive pulses, and Doppler velocity estimates are formed by observing the phase shift between successive pulses. In independent pulse-pair processing, two closely spaced coherent pulses are transmitted, followed by backscatter collection up to the range limit of the sonar; processing is the same as for coherent sonar, however, the presence of overlapping acoustic backscatter introduces increased variance in the velocity estimates.

The distinctions among incoherent, coherent, and independent pulse-pair processing are shown schematically in Figure 2.2. For the incoherent pulses in Figure 2.2a, the mean frequency shift is estimated from the phase evolution of a single pulse A, while for coherent pulses in Figure 2.2b, the mean frequency shift is estimated by

measuring the phase shift between pulses B and C. In contrast, with independent pulse pair processing in Figure 2.2c, the frequency shift is estimated by measuring the phase shift between the pair of transmit pulses D and E. The incoherent, coherent, and independent pulse-pair approaches are explained in detail in Sections 2.3.1, 2.3.2, 2.3.3, respectively.

Bandwidth is a measure of the range of frequencies contained in an acoustic signal and can limit the type of processing possible with a given instrument. Instrument bandwidth is generally limited by the sonar hardware itself (for example, by transducer construction or the maximum hardware sampling rate). A narrowband instrument will transmit and detect a small range of frequencies; while a broadband instrument will transmit and detect a larger range of frequencies. A typical narrowband instrument might have a 250-kHz transmit frequency with a 10-kHz bandwidth (4% bandwidth); that is, it would be sensitive to frequencies between 245 kHz and 255 kHz. A typical broadband instrument might have a 250-kHz transmit frequency with a 125-kHz bandwidth (50% bandwidth); that is, it would be sensitive to frequencies between 125 kHz and 375 kHz. Incoherent and narrowband sonar are often used interchangeably, as are coherent and broadband sonar. Independent pulse-pair processing may be performed with either a narrowband or broadband transducer.

Doppler sonar has seen extensive use in physical oceanography, primarily for the measurement of current velocities (Lhermitte, 1983; Lhermitte and Serafin, 1984; Rowe et al., 1986; Brumley et al., 1987; Cabrera et al., 1987; Brumley et al., 1990; Brumley et al., 1991; Trevorrow and Teichrob, 1994; Wilson Jr. et al., 1997; Mullison et al., 1997), but also for measurements of velocity shear (Pinkel et al., 1987), surface waves (Pinkel and Smith, 1987; Smith, 1989), scattering from turbulence (Lhermitte

and Lemmin, 1990; Seim et al., 1995), and sediment transport (Zedel et al., 1995; Zedel et al., 1996; Zedel and Hay, 1999). Incoherent, coherent, and independent pulse-pair processing have each found their niche for certain types of measurements, as described in the following sections.

2.3.1 Incoherent sonar

Incoherent or narrowband sonars are typically used for long-range current profiling. The mean Doppler shift frequency estimate is formed by following the phase evolution of the backscatter from a single narrowband pulse. Theriault (1986) derived a lower limit on the expected frequency standard deviation σ_ω for a single ping and a diffuse collection of scatterers, as a function of the the pulse length T

$$\sigma_\omega^2 \geq \frac{1}{T^2} \frac{\mathrm{SNR}^2 + 36\,\mathrm{SNR} + 30}{\mathrm{SNR}^2} \tag{2.27}$$

Considering the lower limit of Equation 2.27, and applying the Doppler relation, the expected velocity standard deviation σ_v would be

$$\sigma_v^2 = \left(\frac{c}{4\pi f_0}\right)^2 \frac{1}{T^2} \frac{\mathrm{SNR}^2 + 36\,\mathrm{SNR} + 30}{\mathrm{SNR}^2} \tag{2.28}$$

where c is the speed of sound in water and f_0 is the transmit frequency. In the limit of large SNR, Equation 2.28 further simplifies to

$$\sigma_v = \frac{c}{4\pi f_0 T} \tag{2.29}$$

For a typical operating frequency of $f_0 = 250\,\text{kHz}$ and a pulse length of $T = 1\,\text{ms}$, Equation 2.29 results in a single-ping standard deviation in the velocity estimate of $\sigma_v = 48\ \text{cm}\,\text{s}^{-1}$.

There are three options for reducing the narrowband value of σ_v: increase the transmit frequency, increase the pulse length, or perform some averaging to reduce the standard error $\sigma_{\overline{v}}$ in the mean value of v. If the transmit frequency is increased, increased absorption will correspondingly decrease the profiling range. Increasing the pulse length will only serve to reduce the already poor spatial resolution: with the example pulse length of 1 ms, the spatial resolution is 75 cm, which is already larger than a typical individual fish. Averaging velocity samples might seem to be a reasonable option until one considers the geometry specific to fish detection. A fish swimming at $50\ \text{cm}\,\text{s}^{-1}$ would require a 100-ping average to reduce the uncertainty in the mean velocity to 10% of its swimming speed ($5\ \text{cm}\,\text{s}^{-1}$) if the sonar was set up with parameters described above. In a 2-m wide beam the fish will only be in the beam for 4 s and to achieve 100 samples from the fish the ping rate would have to be 25 Hz. However, a ping rate of 25 Hz would only allow for a maximum profiling range of 30 m. The tradeoffs involved thus make narrowband sonar impractical for the measurement of individual fish speed in most situations.

2.3.2 Coherent sonar

The fundamental difference between coherent and incoherent sonar is that a coherent sonar measures the Doppler shift based on the change in phase *between* successive backscattered pulses, rather than the change in phase *during* one backscattered pulse. Therefore, the expression for velocity standard deviation in Equation 2.29 is not valid

for coherent sonar speed estimates. Also, since frequency shift information is no longer derived from a single long pulse, it is possible to make the pulses shorter to improve the spatial resolution.

The trade-off for coherent sonar is that the approach to signal processing results in limitations on the maximum range and unambiguous velocity which may be measured. First, backscatter from distant but strong targets insonified by an earlier pulse may overwhelm the backscatter received from weaker nearby targets at later pulses, resulting in range ambiguities. Therefore, the maximum unambiguous range R_{max} is related to the lag τ between transmissions by $R_{max} = c\tau/2$. Second, as demonstrated by Equation 2.26, if a scatterer moves further than $\lambda_0/4$ between transmissions, its speed will be aliased, so that the constraint on the maximum unambiguous velocity is $\Delta v = \lambda_0/4\tau$. Combination of the range and velocity limits results in an overall constraint on maximum range and velocity which can be observed with a coherent sonar:

$$\Delta v R_{max} = \frac{c\lambda_0}{8} = \frac{c^2}{8f_0} \tag{2.30}$$

Considering a typical fish swimming speed of 50 cm s^{-1} and a transmit frequency of 250 kHz, Equation 2.30 results in a maximum unambiguous range of 2.25 m. Lowering the transmit frequency would increase the maximum unambiguous range; however, the result would also be a loss of ability to detect smaller fish, which depends on the fish's size relative to the acoustic wavelength.

Zrnic (1977) developed an estimate of the velocity uncertainty for coherent sonar in the limit of large SNR, relatively narrow signal bandwidth w (such that $w\tau < 1/2\pi$),

$\mathbf{f_0}$ (kHz)	τ (ms)	w (s^{-1})	σ_v (cm s^{-1})	$\mathbf{R_{max}}$ (m)
28.1	13.0	7.7	29.7	10.0
62.5	6.0	16.7	27.9	4.5
250.0	1.5	66.7	28.9	1.1

Table 2.1: Example of parameters for fish speed measurement with a coherent sonar: transmit frequency f_0, lag τ, spectral width w, velocity standard deviation σ_v, maximum unambiguous range R_{max}.

and number of pulse pairs M that satisfies $Mw\tau \gg 1/2\pi$:

$$\sigma_v = \frac{c}{4f_0}\sqrt{\frac{w}{\tau\sqrt{\pi}}}\, e^{2\pi^2 w^2 \tau^2} \frac{1}{\sqrt{M}} \tag{2.31}$$

To understand the implications of Equations 2.30 and 2.31, consider a coherent system designed around an ambiguity velocity of 100 cm s^{-1}, which allows some headroom for measurement of fish speeds of 50 cm s^{-1}. Application of Equations 2.26, 2.30, and 2.31 for various transmit frequencies f_0 results in per-ping ($M = 1$) velocity standard deviations σ_v and maximum unambiguous ranges R_{max} shown in Table 2.1. The spectral widths w were chosen so that $w\tau = 0.1$, giving $w\tau < 1/2\pi$. In all three cases the per-ping velocity uncertainty is approximately 30 cm s^{-1}. However, none of the combinations is practical for fish velocity measurement: the unambiguous range varies between 1.1 m and 10 m and the transmit frequency varies between 28 kHz and 250 kHz.

The calculation for $M = 1$ is not strictly valid since Equation 2.31 was derived assuming that $Mw\tau \gg 1/2\pi$. If $w\tau = 0.1$, as used in the examples, then $M \gg 1.59$. To satisfy the requirement that $Mw\tau \gg 1/2\pi$ and also achieve an uncertainty in averaged velocity of 5 cm s^{-1}, it would be necessary to average $M = 36$ pulse pairs.

The longest lag in the example (τ = 13 ms) corresponds to a ping rate of 77 Hz, meaning the fish would only have to be in the beam for about 0.5 s to allow for 36 pulse-pair averages. Coherent processing begins to look feasible until one considers that the improvement in velocity uncertainty has been bought at the cost of serious limitations in either maximum range or minimum detectable target size.

2.3.3 Independent pulse-pair processing

A compromise between incoherent and coherent techniques is the broadband processing technique typefied in RD Instruments' (RDI) acoustic Doppler current profilers (ADCPs), in which a single pair of pulses is transmitted followed by a much longer lag to allow for collection of data to the range limit of the sonar. Significant advantages are realized with higher bandwidths, but it is not necessary to have a broadband transducer to apply the RDI technique, so a more general name for the technique is 'independent pulse pair processing'. With independent pulse-pair processing, two coherent pulses separated by a lag τ are transmitted, followed by collection of backscatter to the range limit of the sonar. The Doppler velocity estimates are then extracted from the phase change between the two pulses in the pair.

The expected velocity uncertainty in the independent pulse-pair case can be derived from Zrnic (1977):

$$\sigma_v = \frac{c}{4\sqrt{2}f_0\pi\tau}\frac{1}{\sqrt{M}}\sqrt{\frac{\left(1+\frac{P_N}{P_S}\right)^2-\rho^2}{\rho^2}} \tag{2.32}$$

where f_0 is the transmit frequency, τ is the lag between the pair of pulses, P_S and P_N are the signal and noise power per sample, ρ is the magnitude of the correlation

calculated from hard limited data (signal intensity removed), and M is the number of pulse pairs used to calculate the average. Using typical parameters of sound speed $c = 1500\ \mathrm{m\,s^{-1}}$, $\tau = 1$ ms, $f_0 = 250$ kHz, $\rho = 0.95$ and SNR = 20 dB (typical of strong scatterers such as fish), Equation 2.32 gives a single-ping velocity uncertainty of 12 $\mathrm{cm\,s^{-1}}$. Assuming only a single velocity sample per fish per ping, only 6 pings would be required to reduce the uncertainty to 5 $\mathrm{cm\,s^{-1}}$ (a level comparable to the previous examples). If the fish were in the sonar beam for more pings it would only improve the standard deviation of the velocity estimate. Furthermore, with a lag of 1 ms and a frequency $f_0 = 250$ kHz the ambiguity velocity is 150 $\mathrm{cm\,s^{-1}}$, high enough for the measurement of most fish speeds.

The independent pulse-pair technique therefore takes advantage of the coherent processing technique while removing the restriction on the maximum unambiguous range. The range resolution, which depends on the pulse length, is decoupled from the velocity standard deviation, which depends only on the time lag between pulses.

Phase-coded transmit pulses are one technique which has been used to reduce the variance in current velocity estimates by increasing pulse bandwidth while retaining the range resolution of shorter pulses and the increased power transmission of longer pulses. A transmit pulse is divided into a number of shorter sub-pulses or 'code elements', and the phase of each code element is varied according to a pattern (Farnett and Stevens, 1990). A code element typically consists of an integral number of full cycles of the transmit signal, for example, 18 cycles of a 99.225-kHz carrier for the sonar described by Trevorrow and Farmer (1992), or 8 cycles of a 250-kHz carrier for the test instrument investigated in this thesis. The most common type of phase code is a binary phase code, in which the code is either +1 or −1 and the corresponding

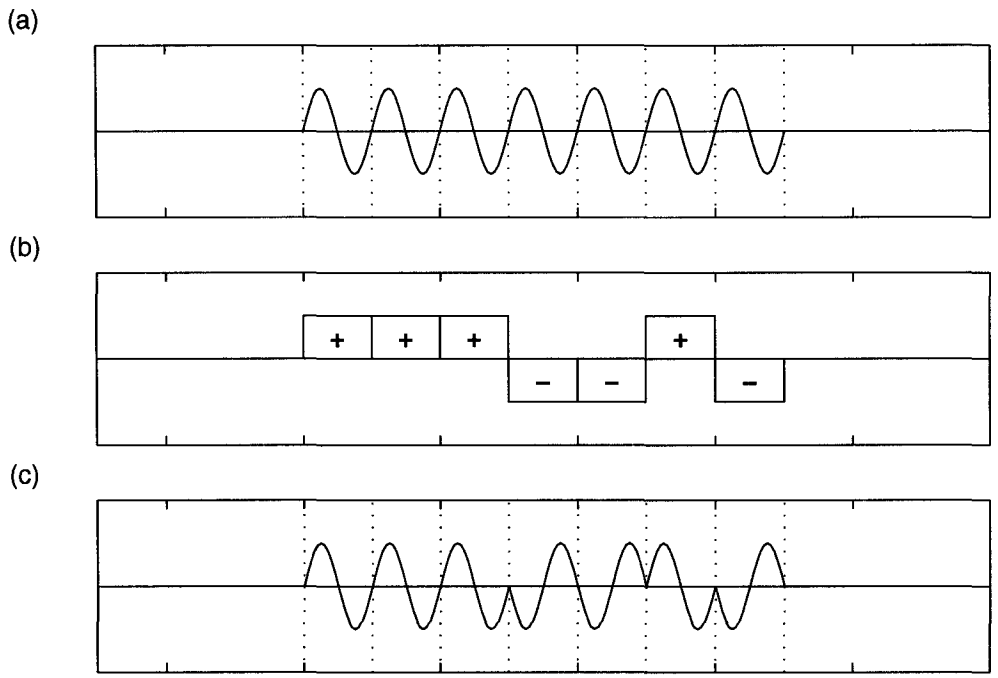

Figure 2.3: Application of binary phase codes. (a) Uncoded pulse, with 7 sub-pulses indicated by dotted lines, (b) 7-element binary Barker phase code, where + indicates 0° phase shift and − indicates 180° phase shift, (c) Pulse from (a) with phase code from (b) applied.

phases are 0° or 180°, as shown schematically in Figure 2.3. For example, the uncoded pulse in Figure 2.3a can be subdivided into 7 sub-pulses of one carrier cycle each, and the 7-element binary phase code in Figure 2.3b can be applied, resulting in the phase-coded pulse in Figure 2.3c.

'Repeat phase coding', in which a phase code is transmitted several times within a longer pulse, has been studied by several investigators for use in incoherent sonar (Trevorrow and Farmer, 1992; Pinkel and Smith, 1992; Trevorrow and Teichrob, 1994). Calculations of the correlation are performed at a lag corresponding to the code

length, resulting in more than one independent estimate of the correlation within the range bin defined by the pulse length. The repeat phase coding scheme has resulted in significant reductions in velocity variance in incoherent sonar systems. However, the repeat phase code technique is similar to the independent pulse-pair case: two repeated phase codes are equivalent to the independent pulse-pair case in which the lag is equal to the length of the code, and three or four repetitions of the code are equivalent to the transmission of adjacent code 'triplets' or 'quadruplets' instead of pairs. It is thus not surprising that in borrowing some coherent signal processing techniques, the standard deviation in velocity estimates made by narrowband sonars has been improved.

The pulses transmitted by the RDI broadband sonars are comparable in length to those transmitted by an incoherent sonar. By phase-coding the transmit pulses, many independent samples of the covariance can be made over a single range bin, rather than the one sample per range bin provided by an incoherent sonar. RDI investigated several methods of phase encoding (Brumley et al., 1987; Brumley et al., 1990; Brumley et al., 1991) before settling on codes chosen by brute force to have low correlation at lags other than the lag between pulse-pairs. Other types of phase codes commonly used are Barker phase codes (Farnett and Stevens, 1990); these have an autocorrelation function which has a peak at zero lag and sidelobes smaller than $1/N$, where N is the length of the code. Unfortunately, only a limited number of Barker codes exist (these are shown in Table 2.2). The usefulness of Barker phase codes for the measurement of fish speed will be evaluated in this thesis.

Length of code N	Code elements
2	+−
	++
3	++−
4	++−+
	+++−
5	+++−+
7	+++−−+−
11	+++−−−+−−+−
13	+++++−−++−+−+

Table 2.2: Barker codes.

2.4 Summary of theoretical concepts

At velocities of interest in oceanography, the Doppler shift is proportional to the radial velocity of the scatterer relative to the transducer. In oceanography, meteorology, and medical ultrasound, the most widely-used method for estimating mean Doppler frequency shifts is the covariance method, which is implemented as incoherent processing, coherent processing, or independent pulse-pair processing. Incoherent and coherent processing are subject to intrinsic restrictions which limit their usefulness in measuring the velocity of discrete targets such as fish. On the other hand, independent pulse-pair processing shows the most promise for individual fish velocity measurement, and can be combined with binary phase coding techniques. It is the combination of independent pulse-pair processing and binary phase coding techniques as applied to fish velocity measurement which will be explored in the remainder of this thesis.

Chapter 3

Instrumentation and Methods

In order to explore the applicability of Doppler sonar techniques to fish velocity measurement, it was necessary to have a custom-built instrument, which would allow a greater degree of control over sonar parameters and data processing than was possible with commercially available instruments. A general-purpose sonar was built for our group by Sontek/YSI and tested in a series of experiments designed to explore its capabilities when measuring fish velocity. Seven experiments were undertaken: four experiments used styrofoam balls in a towtank to simulate fish, and three experiments involved live fish. The styrofoam balls were not meant to precisely simulate swimming fish, but rather to provide a starting point for Doppler velocity measurements, which was built upon by the experiments involving live fish. In addition to the experiments, a computer model of Doppler sonar operation was designed to verify experimental results and to expand upon the range of parameters accessible with the test instrument. The experimental setup and procedures are discussed in this chapter, the experimental results are described in Chapter 4, and the computer model and

results are described in Chapter 5.

The experiments were designed to explore the effects on Doppler velocity estimates of experimental parameters including pulse length, pulse coding, lag, SNR, and type of targets, although each experiment did not employ all possible combinations of parameters. Doppler velocity estimates were compared to independent velocity estimates where possible to determine the error or accuracy, and the standard deviation in the Doppler velocity estimate for a given target was calculated as a measure of the precision. Error and standard deviation will be used as measures of the quality of Doppler sonar fish velocity measurements, and whether or not the Doppler technique can realistically be used to measure fish velocity in the field.

The remainder of this chapter is organized as follows. In Section 3.1, the sonar used in the experiments and the procedure for calibration of the transducer response are described. In Section 3.2, the procedures used to process the sonar data are outlined, and in Section 3.3, an overview of the experiments is presented. Following is a detailed description of the individual experiments: towtank experiments in Section 3.4, field experiments in Section 3.5, and a laboratory experiment in Section 3.6.

3.1 Hardware

In order to explore the capabilities of Doppler techniques applied to fish velocity measurement, a general-purpose coherent sonar was acquired from Sontek/YSI. The test instrument consisted of a single 250-kHz transducer with a beamwidth of 4° and a bandwidth of 30 kHz. Successive acoustic returns can be coherently sampled and the sonar interfaced directly with a laptop computer through a purpose-designed

Industry Standard Architecture (ISA) card. The pulse length, pulse lag, and pulse repetition rate could be set in increments of 32 μs and pulses could be binary phase coded in any pattern input by the user. The maximum ping rate was approximately 50 Hz. The intensity and phase (sine and cosine) components of the received signal were sampled with 8-bit resolution every third code element (this limit was imposed by the hardware), corresponding to a sampling frequency of 10.417 kHz or a range resolution of 7.2 cm, and output to the computer for storage on the hard disk.

No beam pattern measurement was available from the sonar manufacturer. Time and resources did not permit the direct measurement of the beam pattern; therefore, the beam pattern was assumed to follow the theoretical beam pattern resulting from a piston transducer (Medwin and Clay, 1998). Another consideration is the location of the transition from near-field to far-field, since measurements made in the near-field may be subject to unpredictable phase corruption. A conservative estimate for the range to the far-field of a sonar with transducer radius a transmitting at wavelength λ is $\pi a^2/\lambda$ (Medwin and Clay, 1998). Substitution of the test instrument values of $a = 0.06$ m and $\lambda = 0.00592$ m results in a range of 1.9 m to be safely in the far-field. Experiments with targets at ranges greater than 2–3 m should thus be free of phase effects characterstic of the near-field.

The computer controlling the sonar was an IBM ThinkPad 760XL with a docking bay for the ISA card. The ThinkPad had a 166-MHz Pentium processor, 32 MB of RAM, and a 2.1-GB hard drive. The data acquisition software which originally shipped with the sonar did not provide for easy adjustment of the sonar settings, nor did it have a routine to save the sonar output to disk, so the software was modified to make the system more adjustable. The new version of the software allowed the user

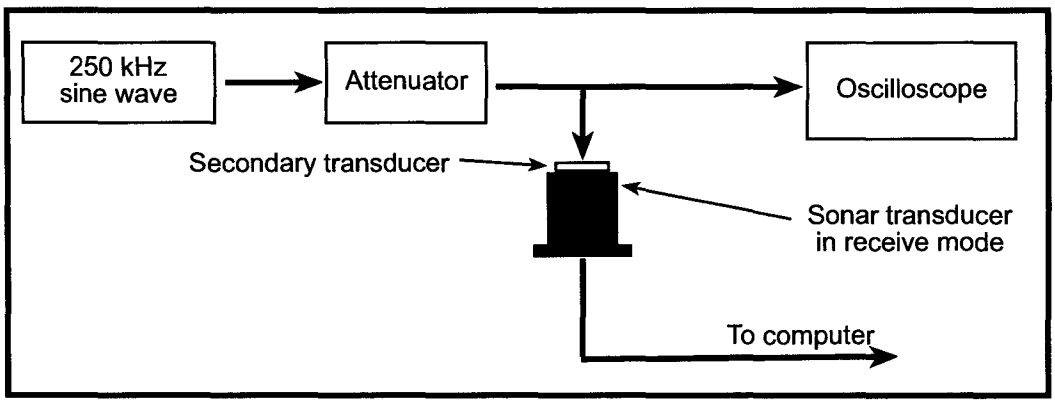

Figure 3.1: Schematic diagram of the sonar logarithmic amplifier calibration.

to control pulse length and coding, lag, pulse repetition rate, number of pings, and destination directory for data files. The software was also designed to limit file sizes to 500 KB, and file naming was automated so that the sonar could run continuously and unattended.

3.1.1 Logarithmic amplifier calibration

The Doppler sonar uses a logarithmic receive amplifier, and output levels from this circuit are recorded as the received intensity. In order to quantify backscatter in absolute terms, the receive circuit response had to be calibrated. A relative calibration was achieved by varying the intensity of a signal delivered into the sonar transducer through a secondary transducer, and measuring the sonar output.

The calibration experimental setup is shown schematically in Figure 3.1. A 250-kHz sine wave (equal to the transmit frequency of the sonar) was input through an attenuator to a 2.7-cm diameter secondary transducer, which was physically coupled to the sonar transducer using gel. Using an attenuator, the voltage input to the

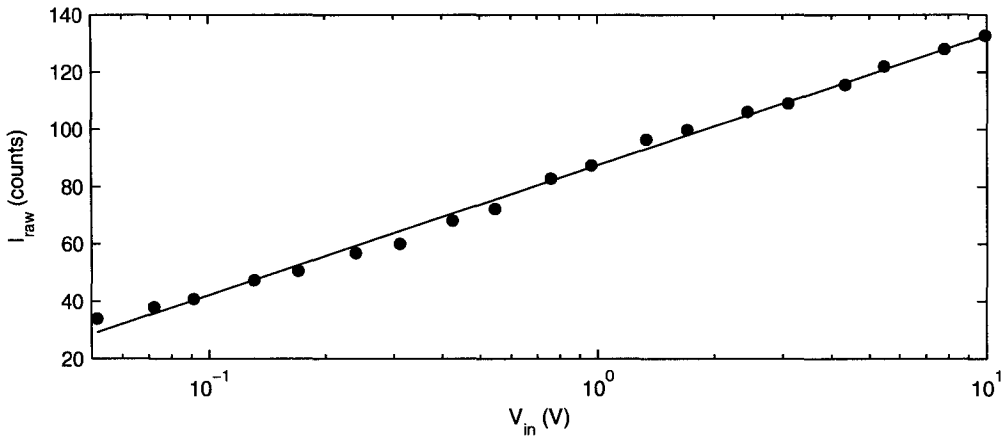

Figure 3.2: Semi-log plot of sonar output as a function of the voltage input to secondary transducer. Error bars are smaller than the plot points at this scale. The equation of the fit line is $I_{raw} = (45.3 \pm 0.8) \log_{10} V_{in} + (87.5 \pm 0.6)$.

secondary transducer was varied between 51.7 mV and 9.9 V as measured with an oscilloscope. A Doppler sonar output file was recorded for each input voltage, with the transmit pulse turned off and sonar set to receive only.

The sonar output I_{raw} is plotted as a function of the logarithm of the voltage input to the secondary transducer V_{in} in Figure 3.2, and a linear fit resulted in the following parameters:

$$I_{raw} = (45.3 \pm 0.8) \log_{10} V_{in} + (87.5 \pm 0.6) \tag{3.1}$$

Recasting Equation 3.1 resulted in an equation to convert raw intensity counts I_{raw} to base-10 decibels I:

$$I = \frac{I_{raw} - I'}{m'} \tag{3.2}$$

where

$$\begin{aligned} m' &= \frac{45.3 \pm 0.8 \text{ counts}/\log_{10}\text{V}}{20 \text{ dB}/\log_{10}\text{V}} \\ &= 2.27 \pm 0.04 \text{ counts/dB} \\ I' &= 87.5 \pm 0.6 \text{ counts} \end{aligned}$$

The corrected intensities calculated by application of Equation 3.2 are referred to an unknown reference intensity, and are therefore only meaningful when added or subtracted, for example, when calculating the SNR or correcting for range effects. The attenuator itself was limited in its range; therefore, there may be other effects near the limits of the output intensity (0 and 255 counts) that were not observed during the amplifier calibration.

3.2 Data processing

Raw data manipulation, target identification, and velocity calculation were all performed using the Matlab programming environment (Matlab, 2002). Targets were identified by treating the backscatter intensity time series as an image and using image processing techniques available in the Matlab software package DIPimage (Luengo et al., 2003). The same procedure was used in all experiments to identify targets, with some details of the processing tailored to particular cases. Once targets were identified, mean Doppler velocity, standard deviation, correlation coefficient, and SNR were calculated for each target.

3.2.1 Velocity and correlation coefficient calculation

Phase data from the Doppler sonar are recorded as positive integers ranging from 0 to 255, which are derived from two separate analog-to-digital (A/D) converters in the sonar and are subject to different offsets and scaling factors. Transformations were applied to force the phase values to lie between -1 and $+1$. First, the mean values of sine $\bar{S}$ and cosine $\bar{C}$ were used to shift the sine S_i and cosine C_i samples to be symmetric about zero:

$$S_i' = S_i - \bar{S} \tag{3.3}$$

$$C_i' = C_i - \bar{C} \tag{3.4}$$

Next, a scaling correction A_i was applied to each corrected pair of samples S_i' and C_i' so that the sum of the squares of corresponding sine and cosine samples was equal to unity:

$$A_i = \sqrt{{S_i}^2 + {C_i}^2} \tag{3.5}$$

$$S_i'' = \frac{S_i'}{A_i} \tag{3.6}$$

$$C_i'' = \frac{C_i'}{A_i} \tag{3.7}$$

The corrected sine and cosine samples were used to calculate velocity v by first recombining them:

$$s_i = C_i'' + iS_i'' \tag{3.8}$$

and then calculating the correlation r_i between samples separated by the lag τ which corresponded to L samples:

$$r_i = s_i \times (s_{i+L})^* \tag{3.9}$$

where * indicates the complex conjugate. Finally, the velocity for a given sample v_i was extracted by scaling the argument of r_i using the ambiguity velocity Δv:

$$v_i = \frac{\Delta v}{\pi} \arg r_i \tag{3.10}$$

In the experiments, receding targets resulted in positive values of velocity and approaching targets resulted in negative values. The complex correlation coefficient ρ was calculated by averaging the correlation r_i (Equation 3.9) of two adjacent samples, giving a measure of the change in phase angle from one sample to the next:

$$\rho_i = |\frac{r_i + r_{i+1}}{2}| \tag{3.11}$$

3.2.2 Target identification

Sine and cosine data were converted to velocity as described in Section 3.2.1, and intensity data were converted from raw counts to decibels using Equation 3.2. The intensity was corrected for range spreading by applying the appropriate correction for discrete targets

$$I' = I + 40 \log_{10} R \tag{3.12}$$

where R is the range in metres (MacLennan and Simmonds, 1992). Strictly speaking, Equation 3.12 should include an additional term to account for absorption (approxi-

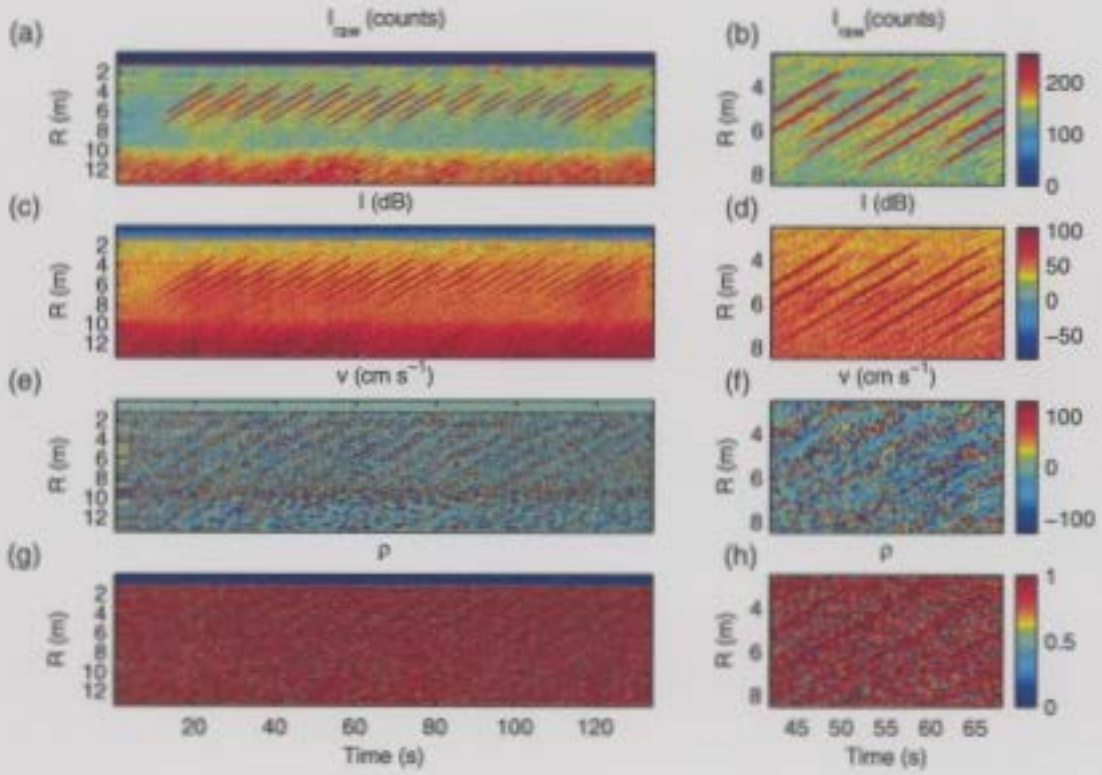

Figure 3.3: Sample sonar data from a towtank experiment (short-range experiment) showing styrofoam targets passing through the sonar beam. The data were collected with a 224-μs pulse, an 1152-μs lag ($\Delta v = 129$ cm s^{-1}), and a tow speed of 24 cm s^{-1} in the beam direction. (a) and (b) Raw backscatter intensity (counts), (c) and (d) Corrected backscatter intensity (dB), (e) and (f) Velocity (cm s^{-1}), (g) and (e) Correlation coefficient ρ.

mately 0.013 dB m^{-1} in fresh water at 20°C (Medwin and Clay, 1998)). For targets at the maximum range of 70 m, the result is a two-way absorption loss of 1.8 dB. Compared with a range spreading loss of 73.8 dB for 70 m range, the absorption term is small, and was thus ignored.

The target identification procedure is most easily demonstrated by examining a series of sample images of intensity, velocity, and correlation data. Figure 3.3 is a set of images from one of the towtank experiments, showing the full data set in

the first column, and an enlargement of the region between 42 and 68 s, 2.5 and 8.5 m in the second column. The transducer was mounted on a tow carriage and aimed horizontally, and styrofoam targets were positioned at the same depth as the transducer (further details can be found in Section 3.4.2). Figure 3.3a is a false-colour image of the raw intensity time series, in which styrofoam targets are visible between 3 m and 8 m range, and the tank wall can be seen at 10 m range, and Figure 3.3b is an enlargement of the same data. Each target appears twice in the backscatter intensity because a pair of pulses was transmitted. Figures 3.3c and d show the same intensity image as Figures 3.3a and b with the amplifier (Equation 3.2) and range-spreading (Equation 3.12) corrections applied.

The velocity was calculated for each sample point in the intensity image, resulting in the velocity images of Figures 3.3e and f. The velocity in the regions corresponding to higher-backscatter targets varies less than the velocity in the lower-backscatter regions where there are no targets. Figures 3.3g and h are images of the correlation coefficient ρ calculated at each sample point. The correlation coefficient is higher in the regions corresponding to the high-backscatter targets than the regions corresponding to the low-backscatter water.

In order to identify which samples corresponded to the targets, a series of operations was performed on the intensity image generated by displaying the intensity data from a series of pings. For the towtank experiments, data acquired during one pass of the tow carriage (traversing all the targets) were treated as a single image; the acquisition time varied with tow speed and ranged between 1 and 20 minutes. For field experiments, intensity data from each file (about 50 s of acquisition time) were treated together as a single image. The image processing parameters particular to

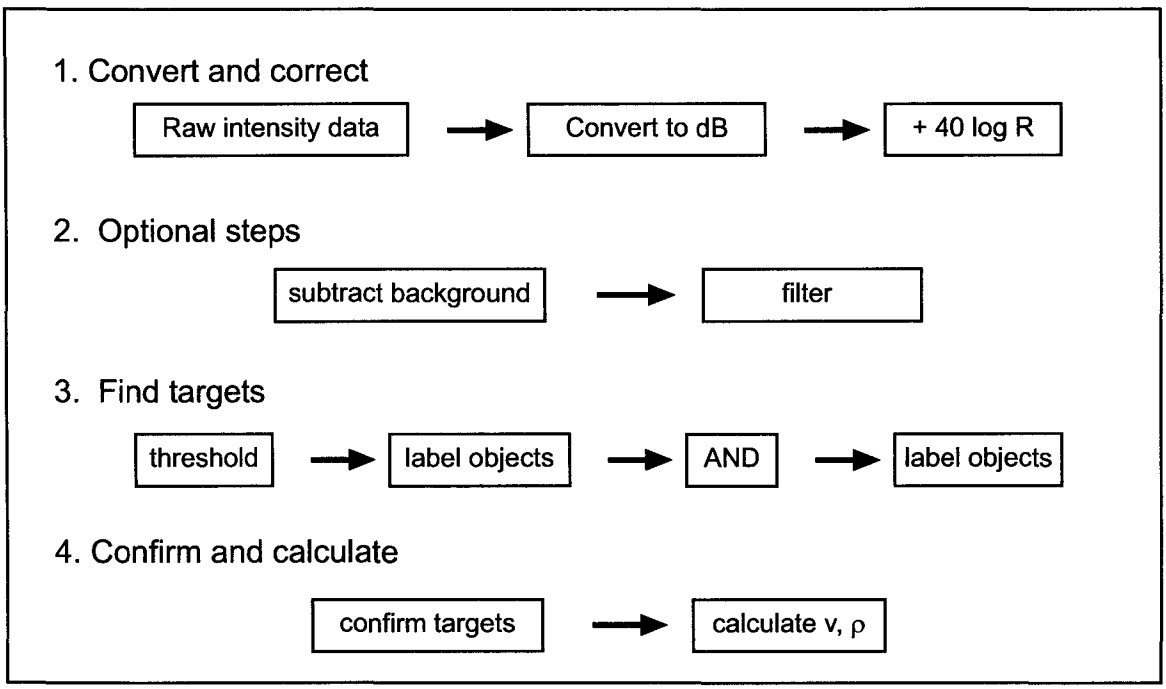

Figure 3.4: Flowchart of the steps involved in target identification.

each experiment are included in Appendix A.1, and a flowchart of the steps in Figure 3.4 illustrates the procedure.

Intensity data were first converted to decibels (Equation 3.2) and corrected for range-spreading (Equation 3.12). Figure 3.5a is the same intensity data shown in Figure 3.3b, in which the amplifier and range-spreading corrections have been applied. The corrections were followed by optional processing for some datasets: average intensity as a function of range was subtracted (necessary for some of the field experiment datasets since there were bands of interference at fixed ranges from bottom or surface reflections), and a Gaussian smoothing filter was applied. The next step for all datasets was to threshold the resulting intensity image with one of two thresholding techniques, either a fixed threshold or one calculated for each image based on the

observed intensities. Figure 3.5b is the binary image resulting from applying a fixed threshold of 80 dB to the data in Figure 3.5a. After thresholding, an object-finding routine in DIPimage was used to label targets (groups of adjacent pixels) of a minimum size. Figure 3.5c is an image of the labelled targets from Figure 3.5b, with labels indicated by different colours. The labelled image was then ANDed with itself at the known value of the lag to eliminate the double targets which appeared because of the transmit pulse pair, and the remaining pixels were again processed with the labelling routine. Figure 3.5d shows the result of the application of the AND operator, followed by another labelling step, on the data of Figure 3.5c. Additional shape and size criteria as well as some human input were used to exclude false targets.

Details of the target identification parameters varied little from experiment to experiment, and can be found in Appendix A.1. Once targets were identified, the data points corresponding to the target were thresholded a second time using the correlation coefficient. The data points which survived the intensity image processing and passed the correlation threshold were used to calculate mean, standard deviation, and standard error of the target velocity, mean target correlation coefficient, signal-to-noise ratio (SNR), and target range.

3.2.3 Signal-to-noise ratio

The signal-to-noise ratio (SNR) was calculated for every target identified in every experiment. In all cases the samples considered to be noise were chosen to be representative of the backscatter from the water near the target region, while the samples considered to be signal were those identified by the target-finding routines as originating from the target (target identification details are in Appendix A.1). Samples

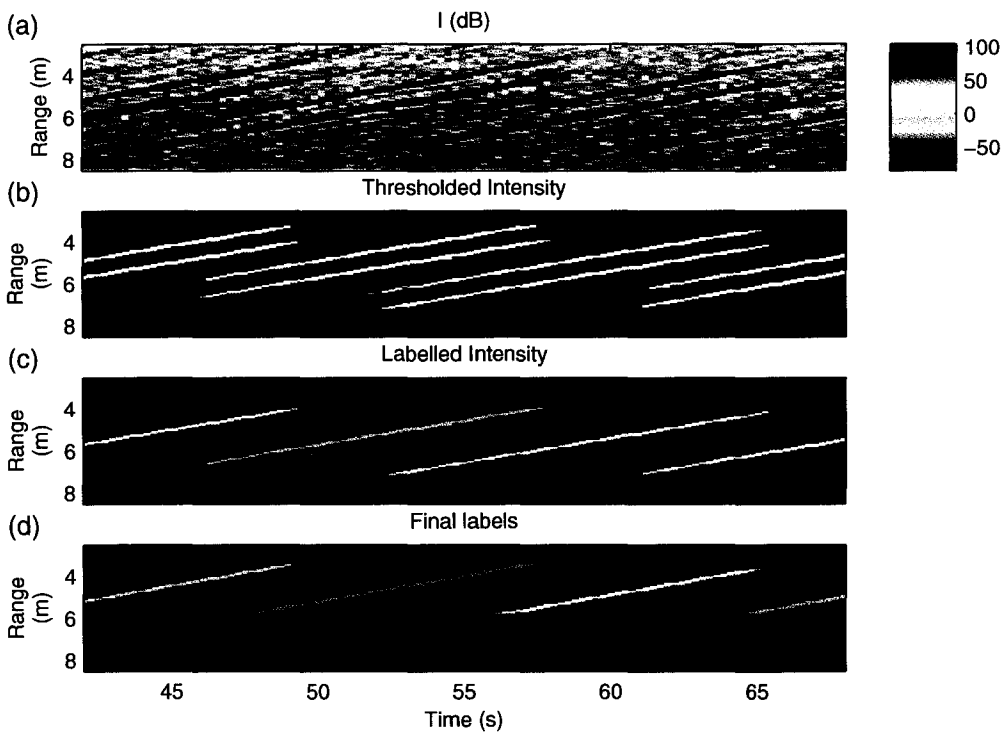

Figure 3.5: Illustration of the steps involved in target identification, using the sample data from Figure 3.3: (a) corrected intensity (dB), (b) a threshold (80 dB) has been applied to the backscatter intensity (white indicates the points which have surpassed the threshold), (c) objects of a minimum size (4 samples) have been labelled (different colours indicate different labels), (d) AND operator has been used to remove double targets caused by two pulses, the remaining objects have be re-labelled (different colours indicate different labels).

corresponding to the second high-intensity return from each target were considered neither noise (as they were comparable in intensity to the targets) nor signal (as they did not correspond to regions of high correlation and uniform velocity).

The SNR is the difference between the average of m signal intensities $I_{S,i}$ and the average of n noise intensities $I_{N,j}$ where intensities had been measured in dB:

$$\text{SNR(dB)} = 10 \log_{10} \left(\frac{1}{m} \sum_{i=1}^{m} 10^{\frac{I_{S,i}}{10}} \right) - 10 \log_{10} \left(\frac{1}{n} \sum_{j=1}^{n} 10^{\frac{I_{N,j}}{10}} \right) \tag{3.13}$$

3.3 Overview of experiments

Laboratory and field experiments were used to determine the capabilities and limitations of the coherent sonar system. In the towtank tests, stationary targets were positioned in a tank, and the sonar was mounted on a carriage which was towed past the targets. In the field tests, the sonar was deployed in a region with known patterns of fish migration. In the laboratory test, live fish were simultaneously observed with both the sonar and a video camera.

A preliminary system performance test was undertaken at the National Research Council's Institute for Ocean Technology (formerly the Institute for Marine Dynamics) in St. John's, using styrofoam balls as targets. This was followed by a preliminary field test during the 2001 migration of pink salmon *(Oncorhynchus gorbuscha)* in the Fraser River in British Columbia. A second field test was undertaken during the 2002 sockeye salmon *(Oncorhynchus nerka)* migration in the Fraser River. Three follow-up towtank tests were undertaken: the first two at the Ocean Engineering Research Centre at Memorial University of Newfoundland, and the third at the Institute for

Ocean Technology. Finally, an experiment in which farm-raised Atlantic cod *(Gadus morhua)* were observed with a video camera and the sonar simultaneously was undertaken at the Ocean Sciences Centre, Memorial University of Newfoundland. Detailed descriptions of the experiments are found in Sections 3.4, 3.5, and 3.6.

3.4 Towtank tests

Four towtank tests were undertaken to explore the performance of the Doppler sonar in controlled conditions with an accurately known velocity for comparison with Doppler estimates. The sonar was mounted on a carriage which was towed past targets submerged in a tank; the sonar and targets were arranged in a variety of different geometries. Stationary styrofoam balls and a moving transducer do not perfectly reproduce field conditions in which a fish moves relative to a stationary transducer. In particular, bubbles associated with motion will be produced near the transducer in the towtank, but near the fish in a field experiment. However, bubble effects are expected to be minimal, and towtank experiments have the distinct advantage of allowing for instrument testing in strictly controlled conditions.

In the target-array experiment, targets were arranged in groups of three with centre-to-centre spacing ranging from 5 cm to 60 cm, and in such a way as to pass through the beam at ranges between 4–6 m. In the short-range towtank experiment, single targets were arranged so as to pass through the beam at ranges between 4–12 m. In the two long-range towtank experiments, single targets were arranged near or on the beam axis, with the sonar aligned along the towtank axis, so that the targets were continuously in the beam at ranges up to 80 m while the sonar moved directly

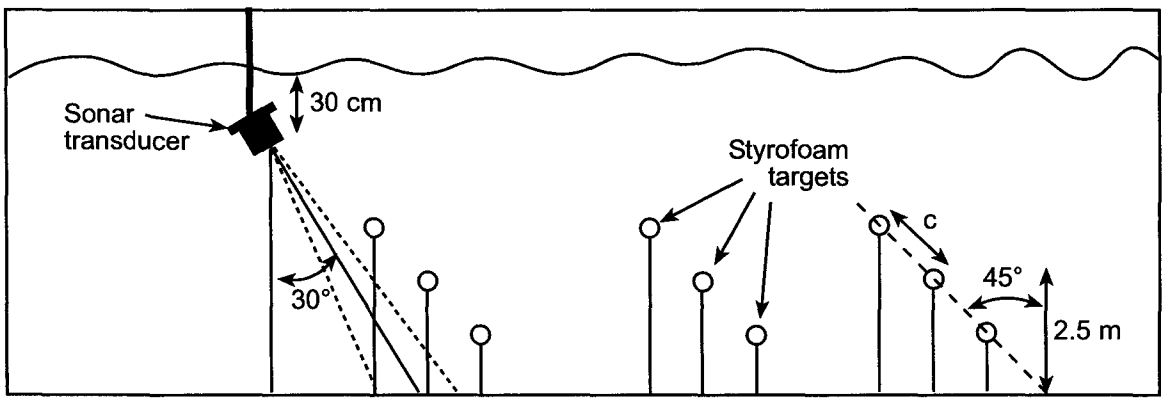

Figure 3.6: Diagram of target-array towtank experiment, side view (not to scale). The sonar transducer was towed past the styrofoam targets which were arranged in groups along a 45° line. The inter-target spacing c differed for the various groups of targets (Table A.1). The sonar beam is shown as dotted lines.

toward or away from the targets.

3.4.1 Target-array experiment

The first experiment using the test instrument was the target-array experiment, which was a preliminary test with four simple goals: to ascertain that the practical operation of the sonar was understood, to find any problems in the sonar software, to determine if the sonar was measuring target velocity accurately, and to explore the limits of the sonar spatial resolution.

The target-array experiment took place in the clear water towtank at the Institute for Ocean Technology (IOT), which is 200 m long, 12 m wide, and 7 m deep, and has a tow carriage that can move in both directions along the tank at precisely controlled speeds. The sonar was mounted on a frame attached to the tow carriage, directed at an angle of 30° from the vertical in the direction of travel of the tow carriage, as shown schematically in Figure 3.6. Both positive and negative resolved tow speeds

were used, from ± 2.5 cm s^{-1} to ± 100 cm s^{-1} in the beam direction (± 5 cm s^{-1} to ± 200 cm s^{-1} horizontally).

Styrofoam balls of density 0.03 g cm^{-3} with diameters of 2.5 cm, 5.1 cm, 7.6 cm, 10.2 cm, and 12.7 cm were used as targets to represent swim bladders of fish. Targets were arranged in groups of three along a 45° line, parallel to the sonar axis, which was originally aligned at 45° to the vertical. The surface sidelobes for the 45° arrangement interfered with target identification so the original mounting bracket was exchanged for a 30° bracket without repositioning the targets. Therefore the target groups were aligned at an angle of 15° to the beam direction. The middle target of each group was 2.5 m above the bottom of the towtank, and the spacing between balls in a group varied from 5 cm to 60 cm (Table A.1). In addition to the oblique target groups, four target groups were arranged horizontally.

Datasets were acquired using coded pulses from 96 μs to 416 μs in length combined with lags ranging from 768 μs to 3168 μs, as detailed in Table A.2. Target identification and data processing parameters are listed in Table A.3.

3.4.2 Short-range experiment

The short-range experiment took place after the two field experiments (Sections 3.5.1 and 3.5.2), and was intended to obtain towtank data with the same pulse length, pulse code, and lag combinations used in the field experiments to allow for direct comparisons of the datasets.

The short-range experiment took place in the towtank at the Ocean Engineering Research Centre (OERC) at Memorial University of Newfoundland, which is 42.5 m long, 2.4 m wide, and 4.8 m deep. The tow carriage can run the length of the tank

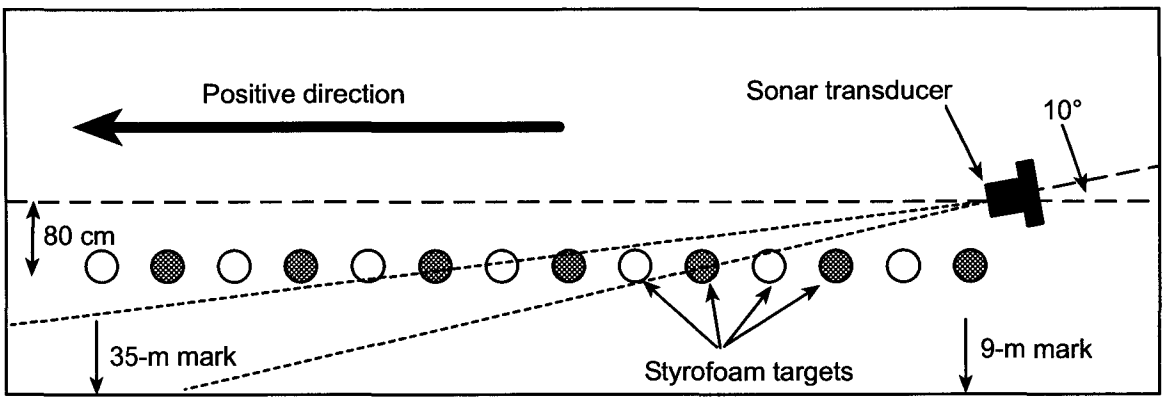

Figure 3.7: Diagram of the short-range towtank experiment, top view (not to scale). The sonar transducer was towed past styrofoam targets which were spaced at 2-m intervals. Targets in grey were removed for runs with lag = 2304 μs to avoid target overlap in the detected backscatter. The tank axis is indicated by a dashed line, and the sonar beam is indicated by a dotted line.

in both directions at precisely controlled speeds. The transducer was attached to a mounting bracket below the tow carriage at a distance of 1.35 m from the tank bottom, pointing horizontally, and the targets were arranged to be at the same depth as the transducer.

Two different target geometries (A and B) were investigated, resulting in 'short-range' and 'long-range' data, respectively. The short-range geometry will be discussed here, while the long-range geometry will be discussed in Section 3.4.3. In the short-range geometry, the targets (Table A.4) were positioned 80 cm from the centreline, and the transducer was aimed at an angle of 10° from the centreline so that the targets passed through the beam between 3 m and 8 m range, as shown schematically in Figure 3.7. Tow velocities used were between ± 5 cm s^{-1} and ± 100 cm s^{-1}, resulting in resolved velocities of between 4.9–98 cm s^{-1}.

Uncoded and coded pulses between 96 μs and 416 μs in length were used in com-

bination with lags from 576 μs to 2304 μs, as listed in Table A.5. Target identification and data processing parameters are listed in Table A.6.

3.4.3 Long-range experiments

The two long-range experiments were designed to complement the results of the stationary field experiment (Section 3.5.2), in which targets had been observed at ranges up to 60 m. The first long-range experiment took place at the Ocean Engineering and Research Centre (described in Section 3.4.2), and the second long-range experiment took place at the Institute for Ocean Technology (described in Section 3.4.1).

In the first long-range experiment, four styrofoam targets were arranged 32 cm from the centreline near one end of the tank, with the sonar aimed directly along the tank axis, so that the targets (Table A.7) were continuously in the beam at ranges between 5 m and 35 m, as shown schematically in Figure 3.8. Tow velocities ranged from ± 5 cm s^{-1} to ± 100 cm s^{-1}. Target identification and data processing parameters are listed in Table A.9. One value for the lag (1152 μs) was combined with uncoded and coded pulses of 96 μs to 416 μs in length (Table A.8).

In the second long-range experiment, five targets were positioned along the axis of the sonar transducer which was aligned with the centreline of the tank and pointing horizontally, 192 cm below the surface (see Figure 3.9). The targets (five styrofoam balls with diameters of 2.5 cm, 5.1 cm, 7.6 cm, 10.2 cm, and 12.7 cm) were placed at 2-m intervals between the 30-m and the 38-m mark of the tank. Tows with velocities between ± 5 cm s^{-1} and ± 100 cm s^{-1} were made between the 50-m and 110-m marks on the tank, resulting in minimum and maximum target ranges of 12 m and 80 m. Uncoded and coded pulses of 96 μs to 416 μs were used in combination with lags of

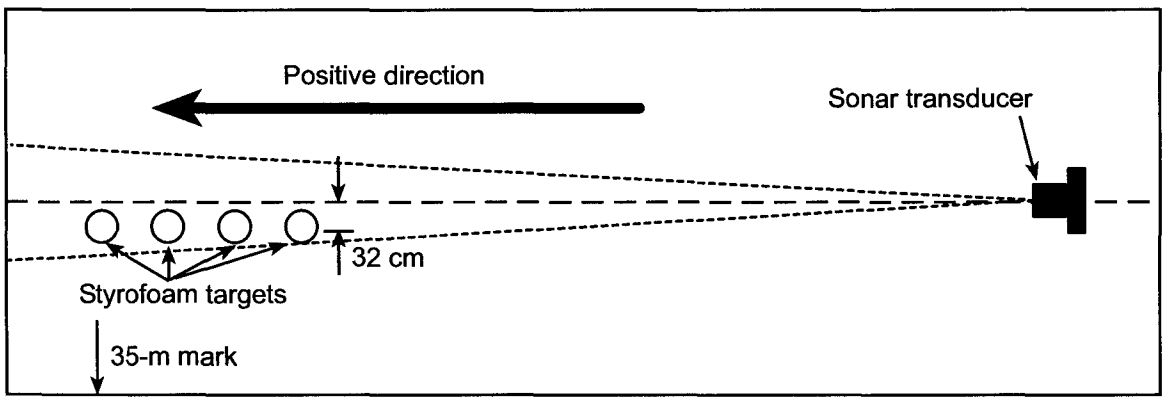

Figure 3.8: Diagram of long-range 1 towtank experiment, top view (not to scale). The sonar transducer was towed toward and away from styrofoam targets which were spaced at 2-m intervals. The tank axis is indicated by a dashed line, and the sonar beam is indicated by a dotted line.

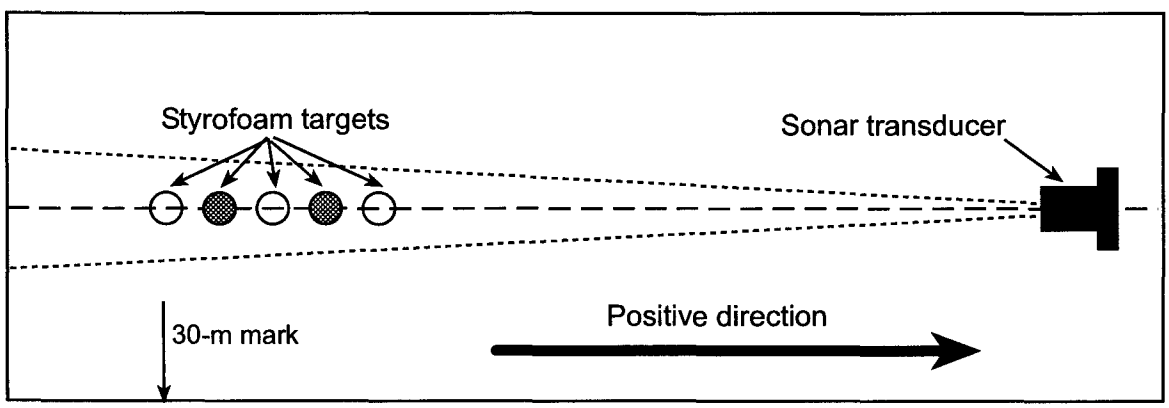

Figure 3.9: Diagram of long-range 2 towtank experiment, top view (not to scale). The targets were spaced at 2-m intervals, and the targets in grey were removed for the runs with lag = 2304 μs. The tank axis is indicated by a dashed line, and the sonar beam is indicated by a dotted line.

576 μs to 2304 μs to allow for comparisons with the other experiments (Table A.10). When the 2304-μs lag was used, the 5.1-cm and 10.2-cm targets were removed to eliminate overlap in the detected backscatter. Table A.11 contains the parameters used for target identification and data processing.

3.5 Field experiments

Two field experiments were undertaken at the Pacific Salmon Commission's hydroacoustic site on the Fraser River near Mission, British Columbia, in order to take advantage of the high densities of migrating fish as well as the practical field support of the crew at the Mission hydroacoustic site. The Doppler sonar was never intended to replace the Pacific Salmon Commission's instrumentation; the Mission field site was chosen specifically because of the sheer number of fish targets present in the Fraser River during salmon migration. The first test took place in September 2001 during the pink salmon *(Oncorhynchus gorbuscha)* migration. The second field test took place in August 2002 during the sockeye salmon *(Oncorhynchus nerka)* migration.

For both field tests, a great number of fish were visible in the data, but not all fish were used for Doppler velocity estimates. The purpose of the experiments was to test the Doppler method of velocity measurement, rather than produce a time series of fish passage. Fish were not selected randomly for Doppler velocity estimation, but were chosen to maximize the numbers of identified targets for which Doppler velocity calculation was straightforward. The chosen fish had to be well-separated from other fish and from the bottom, targets had to be clearly identifiable as fish, equal numbers of targets from each pulse length and lag combination were sought, and fish with

velocity aliasing were not used. Any time series of fish velocities measured by the Doppler sonar would have been skewed by the method of target selection, because conforming to the above requirements resulted in targets that, on average, were well-separated from the bottom, were generally moving upstream, were selected only on days when the sonar was transmitting certain pulse length and lag combinations, and were swimming more slowly. Therefore, direct comparisons were not made between the Pacific Salmon Commission split-beam sonar estimates of fish speed for either field test.

3.5.1 Mobile field experiment

The mobile field experiment was intended to ascertain that the instrument was indeed capable of making measurements of fish swimming velocity in the field. In addition, various pulse length, coding, and lag combinations were explored.

For the field observations made in the Fraser River between 6 and 20 September 2001, the sonar was deployed from a strut mounted on a 5-m boat. The transducer was 40 cm below the surface with the beam oriented 30° from the vertical and directed upstream as shown in Figure 3.10a. The boat was moored near the south river bank, 50 m downstream of the PSC's split-beam transducers (Figure 3.10b).

Uncoded and coded pulses of 96 μs to 416 μs were used in combination with lags of 576 μs to 1152 μs, as detailed in Table A.12. Table A.13 contains the parameters used for target identification and data processing. A total of 177 fish were identified over the course of the mobile field experiment.

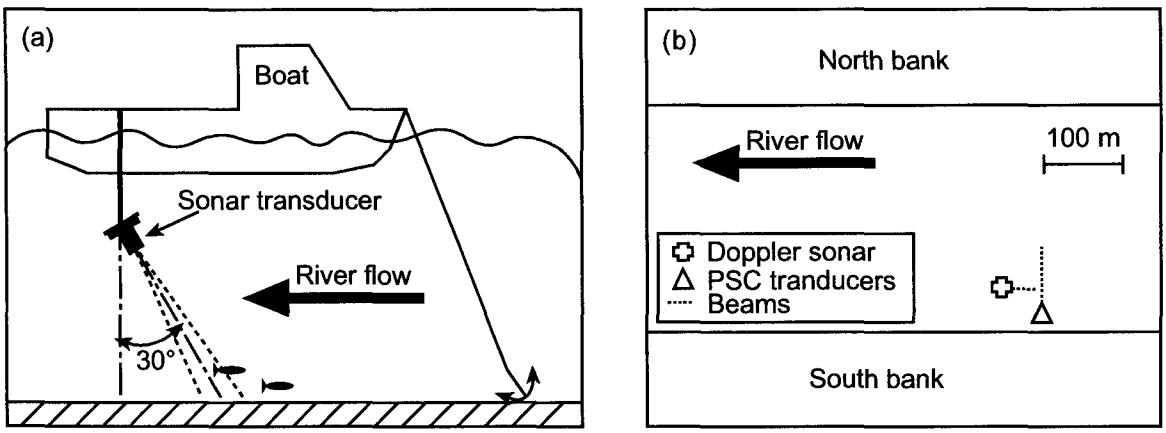

Figure 3.10: (a) Diagram clarifying transducer orientation (not to scale) for the mobile field experiment. The sonar was deployed from a small boat at an angle of 30° to the vertical. Fish were, on average, swimming upriver. (b) Scale diagram of the experimental test site on the Fraser River for the mobile field experiment. River flow direction is indicated by a large arrow, the PSC split-beam transducers are indicated by a triangle, and our boat location is indicated by a plus sign. The sonar beams (not to scale) are indicated as dotted lines.

3.5.2 Stationary field experiment

The follow-up experiment on the Fraser River in British Columbia was meant to expand upon the preliminary data gathered during the first experiment. The deployment geometry was improved so that the sonar could collect data 24 hours a day, and the range of lags, pulse lengths, and coding was expanded.

For the stationary field experiment, the data collection took place from 15 to 27 August 2002. The sonar was deployed on a stationary bracket, aimed horizontally and approximately upstream as shown in Figure 3.11a, resulting in measurement of a greater component of the target velocity than in the mobile field experiment (Section 3.5.1). The sonar orientation was slightly changed several times during the experiment in an attempt to maximize fish numbers while minimizing surface and

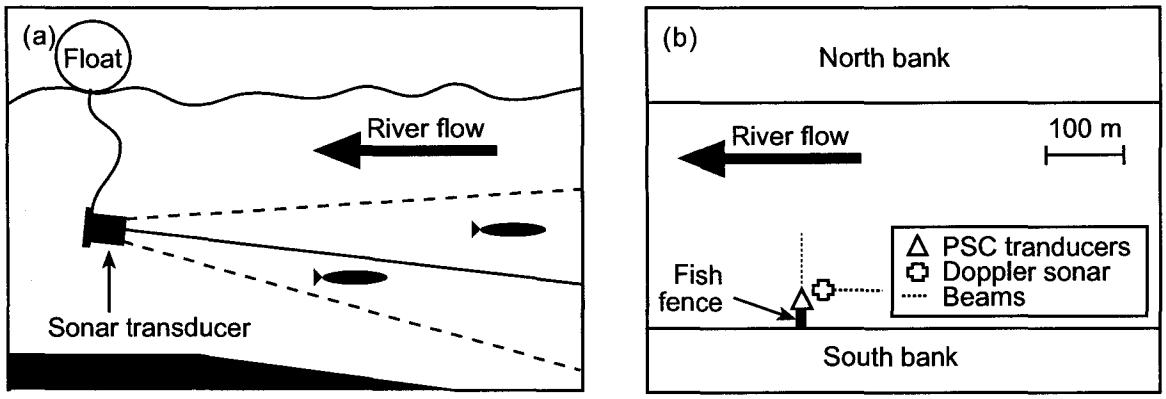

Figure 3.11: (a) Diagram (not to scale) of the setup for the stationary field experiment. The sonar was deployed 80 cm from the bottom, looking upriver 2° below horizontal. (b) Scale diagram of the stationary experimental test site on the Fraser River, near the PSC fish fence. River flow direction is indicated by a large arrow, the PSC transducers are indicated by a triangle, and the Doppler sonar location is indicated by a plus sign. The sonar beams are indicated as dotted lines.

bottom reflections (Table A.14). The deployment bracket was located just upstream of the PSC's fish-fence and transducers, as shown in Figure 3.11b.

Uncoded and coded pulses of 96 μs to 416 μs were used in combination with lags of 576 μs to 2304 μs, as detailed in Table A.15. Table A.16 contains the parameters used for target identification and data processing. The location of the sonar beam resulted in multiple surface and bottom reflections; therefore, in each file (about 200 pings) the mean backscatter as a function of range was calculated and subtracted from each ping after converting backscatter counts to dB. A total of 8813 fish were identified over the course of the stationary field experiment.

3.5.3 Independent fish velocity measurements

The 'true' velocity needed for comparisons with measured Doppler velocity was readily available for the towtank experiments. No separate instrument was available for

deployment to simultaneously measure the swimming speed of fish being observed during the field experiments. Instead, for the two field experiments, simultaneous independent measurements of fish velocity were extracted by differentiating the range to the targets as a function of time.

Velocity calculated by differentiation of the fish position as a function of time is independent of the Doppler technique, since it relies only on the ping rate and the fish intensity image, neither of which is used to calculate Doppler velocity. The independent velocity estimate is extracted by fitting a straight line to fish position as a function of time. The slope of the line is equal to the fish velocity, so the velocity calculated with this technique will be referred to as the slope velocity or v_{slope}.

Figure 3.12a is the backscatter intensity image from a target in the mobile field experiment, and Figure 3.12c is the backscatter intensity image from a target in the stationary field experiment. Figures 3.12b and d are images of the samples (in white) corresponding to the identified targets, with the straight-line fits plotted in red. For the mobile field experiment, the fit resulted in $v_{slope} = 24 \pm 2$ cm s^{-1}, while the Doppler estimate was $v = 36.9 \pm 0.4$ cm s^{-1}. For the stationary field experiment, the fit resulted in $v_{slope} = 37.4 \pm 0.2$ cm s^{-1}, while the Doppler estimate was $v = 35.6 \pm 0.7$ cm s^{-1}.

The Doppler and slope velocities are much closer in value for the stationary field experiment than for the mobile field experiment. The slope velocity is consistently lower than the Doppler velocity for all the identified fish in the mobile field experiment: the mean value of $v - v_{slope}$ is 17.4 ± 0.8 cm s^{-1} for the mobile field experiment, compared with 0.18 ± 0.05 cm s^{-1} for the stationary field experiment.

The systematic disagreement between v and v_{slope} is the result of a combination of beam geometry, fish size, and average swimming direction in each experiment. Slope

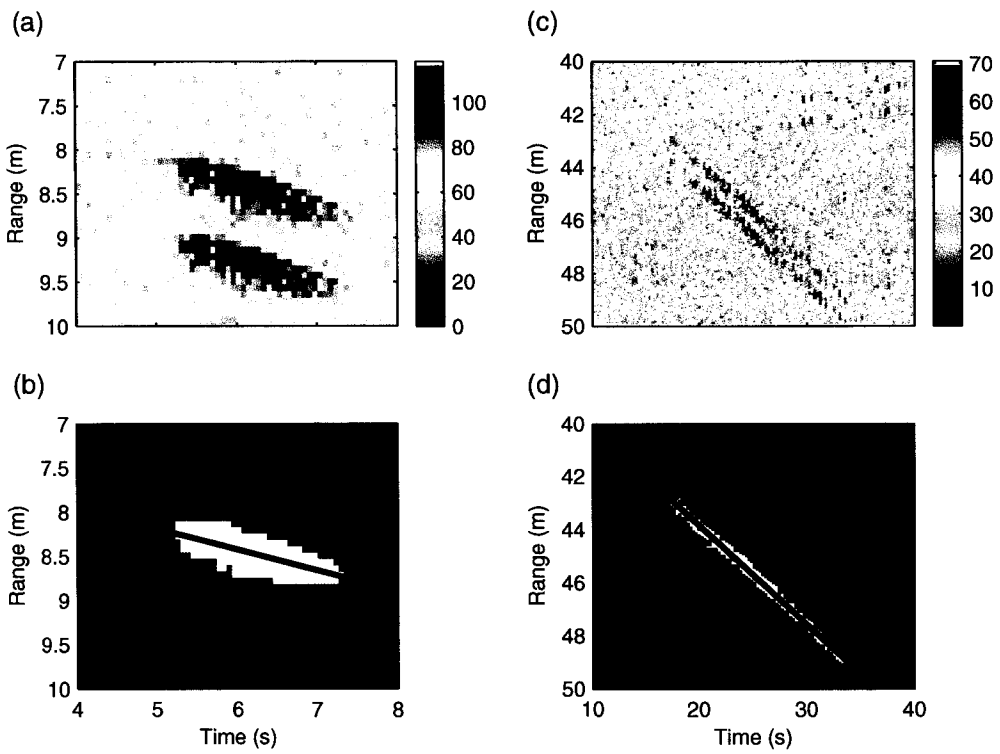

Figure 3.12: Illustration of the calculation of v_{slope}: (a) Backscatter intensity (mobile field experiment), (b) Identified target from (a) shown in white pixels, with the least-squares fit in red, equation $R = (7.0 \pm 0.1) + (0.24 \pm 0.02)t$, (c) Backscatter intensity (stationary field experiment), (d) Identified target from (c) shown in white pixels, with the least-squares fit in red, equation $R = (36.38 \pm 0.05) + (0.374 \pm 0.002)t$.

velocity estimates cannot be corrected for individual fish, since the true swimming direction, swimming speed across the sonar beam, and fish size are unknown; however, by examining the case of a 'typical' fish in each of the field experiments, the average discrepancy can be explained. Consider a fish of length L entering the sonar beam at an angle θ relative to the beam normal and an angle ϕ_1 relative to the beam axis, at a position corresponding to range R_1 as measured along the beam axis, as shown schematically in Figure 3.13. The fish then exits the beam at an angle θ relative to the beam normal and an angle ϕ_2 relative to the beam axis, at a position corresponding to range R_2 as measured along the beam axis. The position of the fish's geometrical centre $\mathbf{r_{fish}}$, its head $\mathbf{r_{head}}$ and tail $\mathbf{r_{tail}}$ are

$$\mathbf{r_{fish}} = R\tan\phi\hat{\mathbf{i}} + R\hat{\mathbf{j}} \tag{3.14}$$

$$\mathbf{r_{head}} = \mathbf{r_{fish}} - \frac{L}{2}\cos\theta\hat{\mathbf{i}} + \frac{L}{2}\sin\theta\hat{\mathbf{j}} \tag{3.15}$$

$$\mathbf{r_{tail}} = \mathbf{r_{fish}} + \frac{L}{2}\cos\theta\hat{\mathbf{i}} - \frac{L}{2}\sin\theta\hat{\mathbf{j}} \tag{3.16}$$

If the fish, as in the diagram, is swimming away from the sonar with velocity

$$\mathbf{v} = v\cos\theta\hat{\mathbf{i}} + v\sin\theta\hat{\mathbf{j}} \tag{3.17}$$

then the nearest point to the sonar axis as the fish enters the beam is its head, and the furthest point from the sonar axis as the fish leaves the beam is the tail. The closer a target is to the axis, the stronger the backscatter and the more likely it is to pass the thresholds and form part of the fish image. A rough approximation of the differentiation method is to use the entrance and exit ranges $\mathbf{r_1}$ and $\mathbf{r_2}$ and the

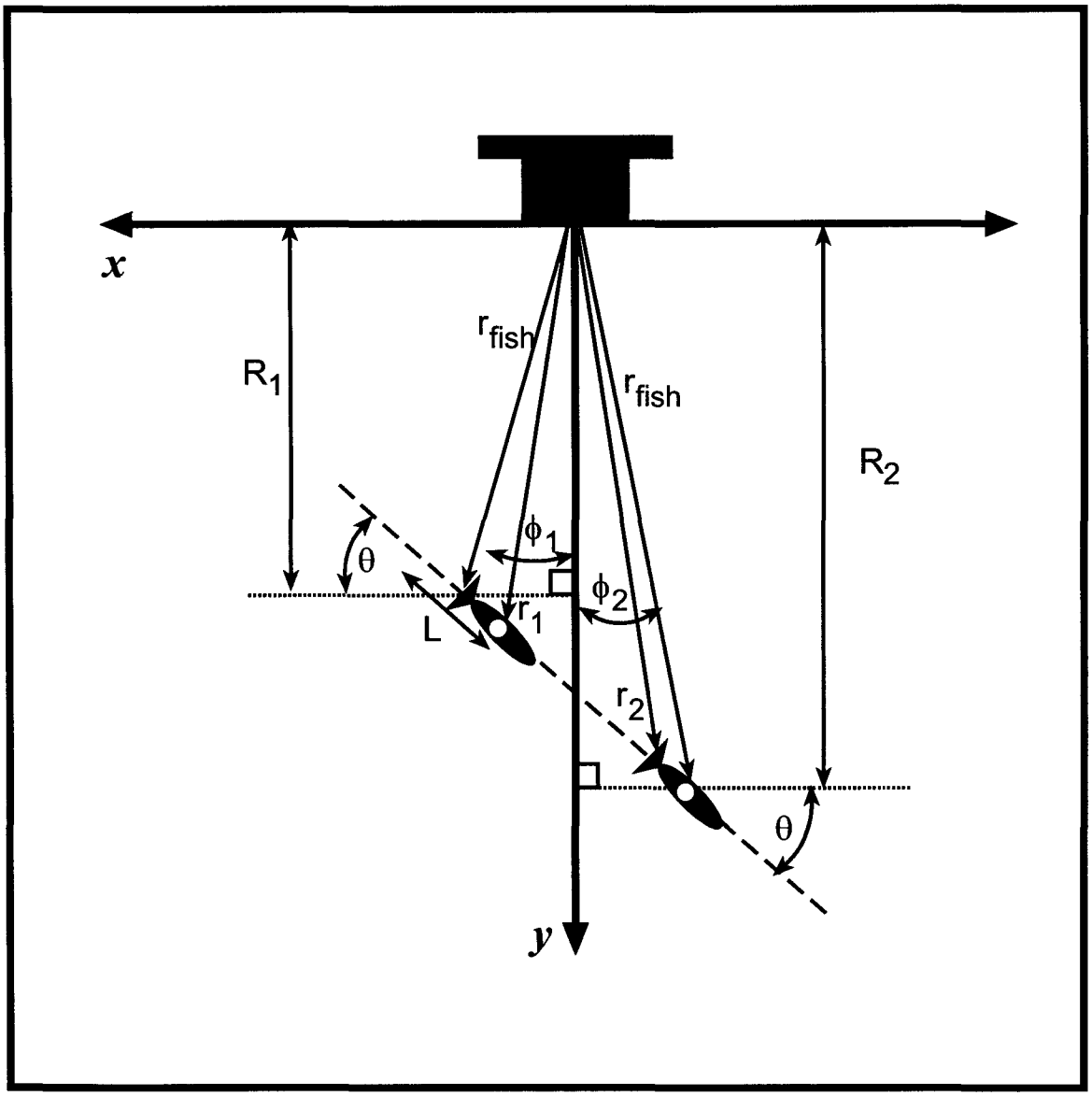

Figure 3.13: Diagram of fish position in beam. The fish of length L enters the beam at angle ϕ_1, with its head at a distance $\mathbf{r_1}$ from the transducer, its centre at range R_1, swimming at an angle θ to the beam normal; exits the beam at angle ϕ_2, with its tail at a distance $\mathbf{r_2}$ from the transducer, its centre at range R_2.

time-in-beam T_{beam} to calculate the velocity:

$$|\mathbf{v}| = \frac{|\mathbf{r_2}| - |\mathbf{r_1}|}{T_{beam}} \tag{3.18}$$

$$\mathbf{r_1} = \mathbf{r_{fish}}(\phi_1, R_1) + \mathbf{r_{head}} \tag{3.19}$$

$$\mathbf{r_2} = \mathbf{r_{fish}}(\phi_2, R_2) + \mathbf{r_{tail}} \tag{3.20}$$

The magnitudes for $\mathbf{r_1}$ and $\mathbf{r_2}$ are

$$|\mathbf{r_1}|^2 = R_1^2 \sec^2\phi_1 + \frac{L^2}{4} + R_1 L(\sin\theta - \tan\phi_1 \cos\theta) \tag{3.21}$$

$$|\mathbf{r_2}|^2 = R_2^2 \sec^2\phi_2 + \frac{L^2}{4} + R_2 L(\tan\phi_2 \cos\theta - \sin\theta) \tag{3.22}$$

Substitution of Equations 3.21 and 3.22 into Equation 3.18 results in a value for the differentiated velocity as a function of angles ϕ_1 and ϕ_2, ranges R_1 and R_2, time-in-beam T_{beam}, angle relative to beam θ, and fish length L, all of which are different for the two field experiments.

Field data were used to calculate average range to fish R and time-in-beam T_{beam} for use in Equation 3.14 in order to determine a typical value for the discrepancy between v_{slope} and v. The fish were assumed to be travelling directly upstream, so that the angle relative to the beam normal was taken to be $\theta = 30°$ for the mobile field experiment, and $\theta = 85°$ for the stationary field experiment. Representative speeds and fish lengths were needed for use in Equation 3.14; therefore, speed was taken as $v = 50$ cm s^{-1}, and fish length L was taken as 50 cm.

Using values for R_1, T_{beam}, θ, and $\phi_1 = \phi_2 = \phi$ typical of the two field experiments, the error in v_{slope} (the difference between true velocity and Equation 3.18) is plotted

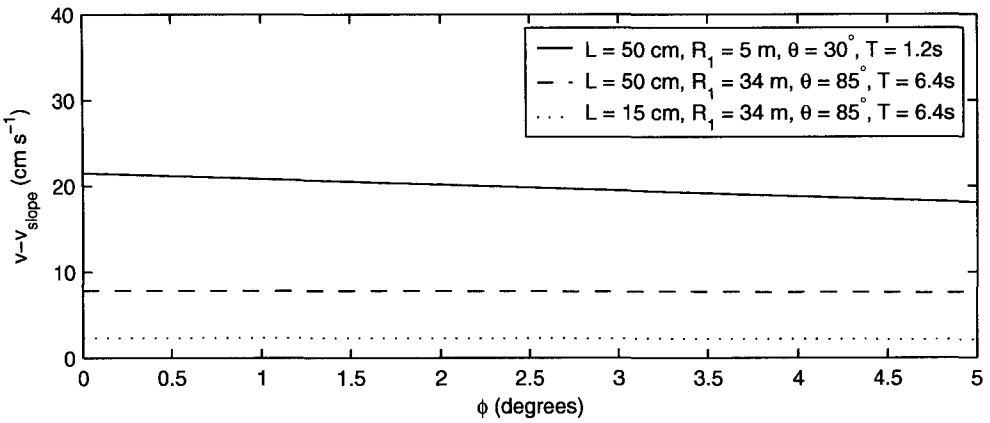

Figure 3.14: Plot of difference between the Doppler velocity estimate v and the slope velocity estimate v_{slope} as a function of beam angle for a 50-cm fish in the mobile field experiment (solid line), a 50-cm fish in the stationary field experiment (dashed line), and a 15-cm fish in the stationary field experiment (dotted line).

as a function of range in Figure 3.14 for three different scenarios: a 50-cm fish in the mobile field experiment, a 50-cm fish in the stationary field experiment, and a 15-cm fish in the stationary field experiment.

Assuming salmon length $L = 50$ cm in Equation 3.18 for the stationary field experiment geometry resulted in larger biases (8 cm s^{-1}) than actually observed (< 1 cm s^{-1}). The longer ranges (up to 70 m) for the stationary experiment resulted in higher noise levels in the vicinity of the fish, and it is likely that the backscatter from the fish body was thresholded out during image processing, leaving only the fish swim bladder identified as a target at longer ranges. Therefore, for the stationary field experiment, the fish length as seen by the sonar was not the entire fish length, but just that of the swim bladder. The swim bladder length in the stationary experiment estimated based on a target strength TS = -27.7 dB is 15 cm (MacLennan and Sim-

monds, 1992). The dotted line in Figure 3.14 is plotted using $L = 15$ cm in Equation 3.18, and gives biases of 2 cm s^{-1}, which are comparable to those observed in the field. Therefore, v_{slope} provides useful values for comparison with Doppler velocity only for the stationary field experiment.

3.6 Silo tank experiment

The silo tank experiment was intended to bridge the gap between a completely controlled environment with artificial targets and the completely uncontrolled environment with real fish targets. It was designed to make independent measurements of fish swimming velocity with a separate instrument, since the estimates of v_{slope} were subject to some error which depended on unknown quantities such as the transverse component of fish swimming velocity (Section 3.5.3).

The experiment took place in September 2003 in a silo tank in the Aquaculture Research and Development Facility at the Ocean Sciences Centre (OSC) in St. John's, Newfoundland. Figures 3.15a and b are schematic top and side views of the silo tank, which is cylindrical in shape with a cone at the bottom. The cylindrical portion is 2.50 m in height and 2.31 m in diameter, and the cone is 2.57 m in height and tapers to a drain at the bottom. The tank is supplied with running sea water from the OSC's sea water circulation system, and initially contained eight cod *(Gadus morhua)* of length between 20 and 30 cm. Two fish jumped out of the tank over the course of the experiment so the final number of fish was reduced to six. Most of the time, the fish stayed near the bottom of the tank, but from time to time they swam upward or downward through the sonar beam.

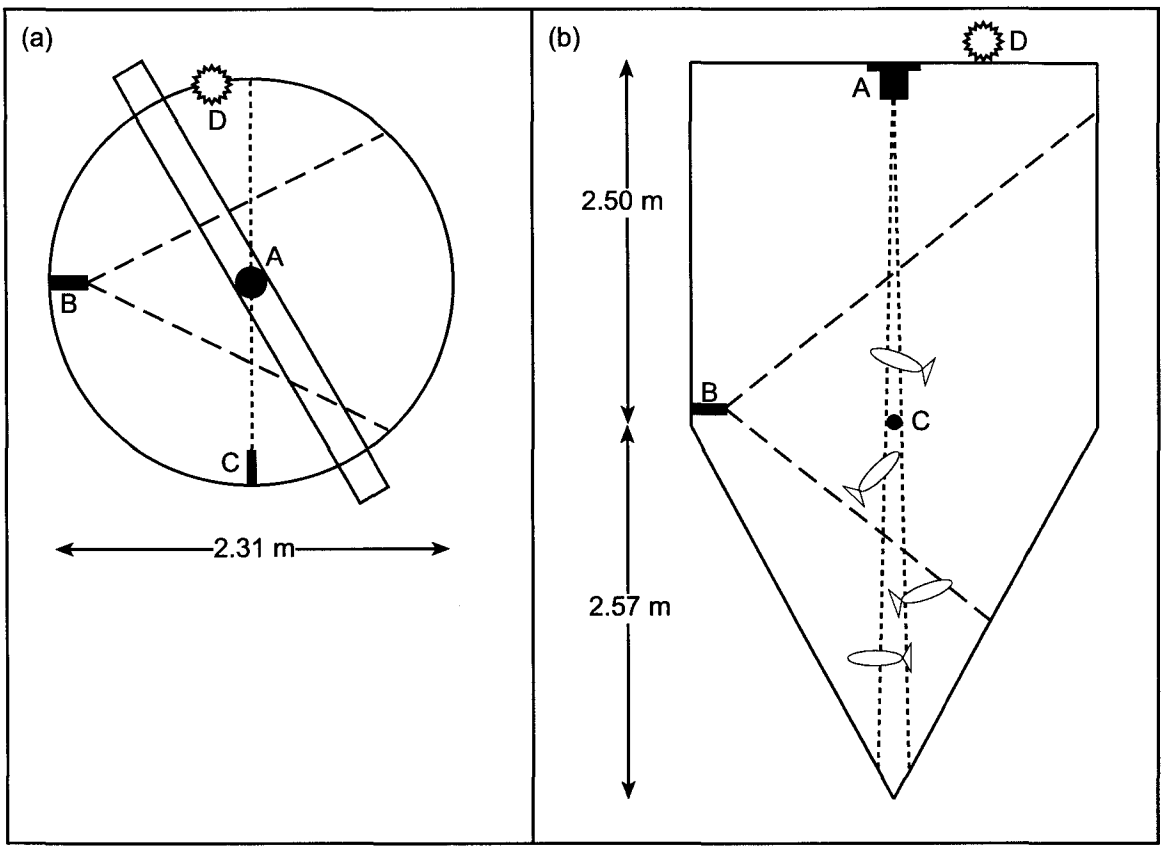

Figure 3.15: Diagram of the silo tank experimental setup (not to scale): (a) top view, showing downward-looking sonar (A), horizontal-looking underwater video camera (B), and fan-beam laser (C). A floodlight (D) was mounted above the tank so that the fish would be visible in the underwater camera. The dotted line indicates the laser beam, and the dashed line indicates the approximate FOV of the camera. (b) side view, in which the dotted line indicates the approximate sonar beam (-3 dB point) and the dashed line indicates the approximate FOV of the camera.

The sonar was mounted at the top of the tank, aimed downward along the centre of the tank as shown in Figure 3.15b. An underwater camera was mounted on the tank wall at a depth of 2.48 m, aimed toward the centre of the tank, and aligned so that the centre of the field of view (FOV) coincided with the centre of the sonar beam. The camera's FOV corresponded to a range along the sonar axis of 1.25 m to 2.84 m from the transducer. A laser which produced a vertical fan beam was mounted on the tank wall at the same depth as the camera but oriented at 90° to the camera axis, and aligned with the sonar axis. The combined orientation of sonar, camera, and laser was such that any fish swimming in the centre of the FOV of the camera while being illuminated by the laser beam would be on the sonar beam axis (see Figure 3.15). The upward or downward component of the fish's motion in the camera's FOV would correspond to the speed as observed by the sonar. A floodlight was mounted on the edge of the tank to provide adequate illumination to see the outlines of the fish in the camera.

To calibrate vertical distance as seen by the camera, a ruler was lowered to within 15 cm of the centre of the FOV of the camera, and aligned with the laser beam (the sonar position prevented the ruler from being lowered into the very centre of the FOV). A few seconds of video were recorded and the same exercise was repeated for the horizontal scale.

The small size of the tank created considerable problems for the sonar with multiple reflections and sidelobes reflected from the surface. After some experimentation with pulse lengths and lags, it was determined that only a 576 μs lag and a 96-μs uncoded pulse would result in usable data.

The camera and sonar combination were set up to record over the course of four

days, and operation was restricted to hours when the facility was accessible (08:00 to 17:00). The video signal from the underwater camera was recorded onto 90-minute digital video tapes using a Sony DCR-TRV25 MiniDV Recorder. The clocks on the computer running the sonar and the video recorder were synchronized to within ± 0.5 s so as to allow identification of fish which appeared simultaneously in both the video and the sonar data.

3.6.1 Data extraction

An immense amount of video data recorded showed no fish along the sonar axis. The video tapes were reviewed and only those portions where fish moved through the centre of the FOV and through the laser beam simultaneously were analyzed. Video data identified for analysis was transferred via FireWire onto a PC at a rate of 15 frames per second (fps), with 720×480 pixels per frame. The horizontal and vertical scale calibration portion of the video was captured in a similar manner at 29.97 fps, to maximize the number of samples for the scale calibration (67 frames for the horizontal calibration, 59 frames for the vertical calibration).

The underwater camera was fitted with a wide-angle lens which meant that the horizontal and vertical scale factors changed with position in the image. The major scale divisions on the ruler in the calibration video frames were identified, and the distance in pixels between scale divisions was calculated, averaged, and inverted to provide a measurement in pixels m^{-1}. Figure 3.16a is a plot of the vertical scale as a function of vertical position, and Figure 3.16b is a plot of the horizontal scale as a function of horizontal position. The calibration data were fitted to a least-squares parabolic model in that portion of the FOV which was used for tracking fish, and

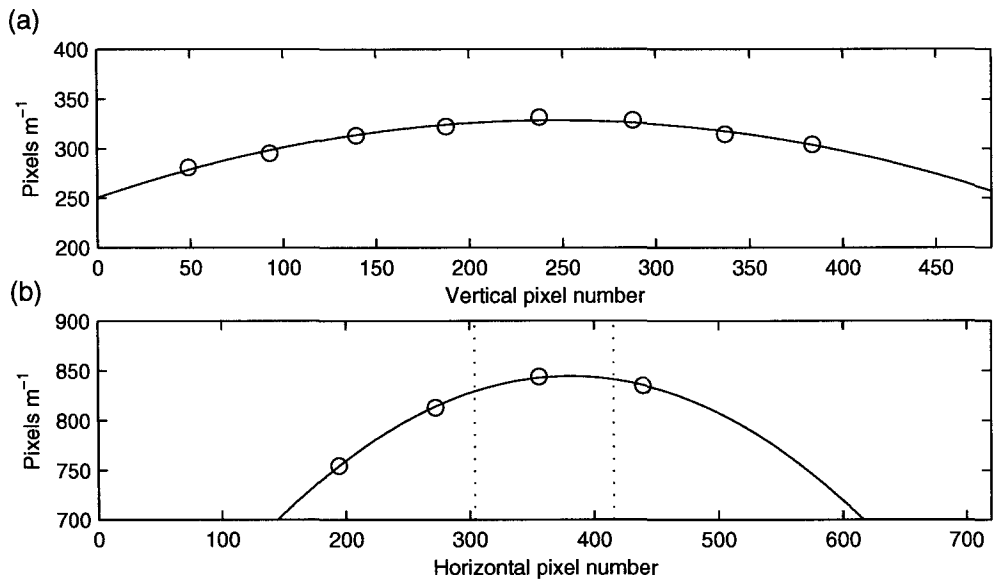

Figure 3.16: (a) Plot of vertical scale as a function of vertical pixel position, with fit line $y = 250 + 0.636x - 0.00130x^2$, $R = 0.977$. (b) Plot of horizontal scale as a function of horizontal pixel position, with fit line $y = 468 + 1.98x - 0.00260x^2$, $R = 1.000$. The dotted lines indicate the pixels corresponding to the width of the sonar beam.

the fit parameters are included in the caption of Figure 3.16. The bottom-left corner of the image was defined as the origin, and the fits were used to calculate x and y positions for each pixel, resulting in a scale which changed according to position within the image.

The video clips of swimming fish were analyzed using Matlab by playing the video frame-by-frame and identifying the nose and tail of the fish in each frame. The nose and tail locations were converted to x and y positions within the frame. The nose of the fish had less velocity variation than its tail, which showed significant transverse motion; therefore, the nose points were the ones used to determine swimming velocity. A linear least-squares fit was performed to the y-position of the fish's nose as a function of time to obtain the slope of the line, which was equal to the velocity in the

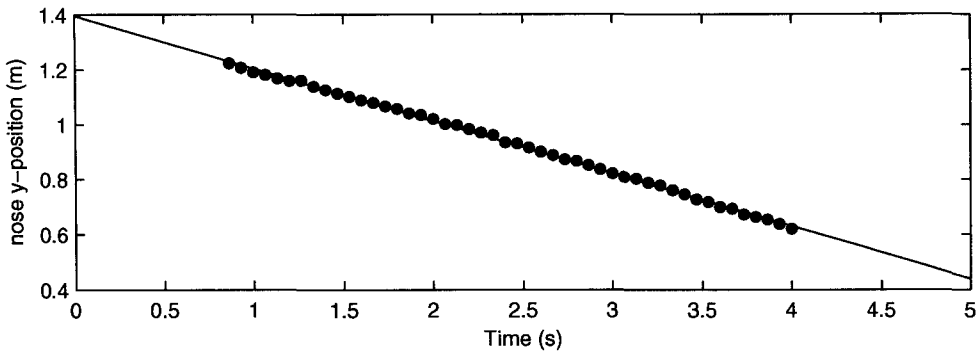

Figure 3.17: Plot of y position for fish #18 as a function of time, with linear fit shown. The equation for the fitted line is $y = (1.396 \pm 0.003) - (0.191 \pm 0.001)t$, giving a speed of -19.1 ± 0.1 cm s^{-1}. The correlation coefficient for the linear fit is $r = -0.999$.

y-direction (a sample fit is shown in Figure 3.17).

Table A.17 contains the parameters used for target identification and processing of the Doppler sonar data. To match up the two types of velocity estimates, the time and range of the fish in the sonar beam were compared with the time and range of the fish in the video, resulting in 54 fish which were simultaneously observed in both the video and the sonar beam.

3.7 Summary of Materials and Methods

A custom-built coherent Doppler sonar was used to explore the utility of Doppler techniques for measurements of fish swimming velocity. Through a variety of field and laboratory trials, acoustic backscatter intensity was used to determine target location by treating the time series of intensity as an image and applying basic image processing algorithms. For identified targets, mean Doppler velocity and standard deviation, SNR, and complex correlation coefficient were calculated.

A total of seven experiments were completed: four towtank experiments in which stationary styrofoam balls were observed while the sonar was moving, two field experiments in which migrating salmon were observed, and one laboratory tank experiment in which video observations of cod were compared with sonar data. The experiments were designed to explore the effects on Doppler velocity estimates of experimental parameters such as pulse length, pulse coding, lag, SNR, and type of targets. No single experiment employed all possible combinations of operating parameters. The error, or difference between Doppler velocity estimates and independent velocity estimates, was used as a measure of accuracy, and the standard deviation in a Doppler velocity estimate for a single target was used as a measure of precision. Error and standard deviation taken together will be a measure of the quality of Doppler sonar fish velocity measurements, and their values will determine whether or not the Doppler technique can be used to measure fish velocity effectively in the field.

Chapter 4

Experimental Results

The experiments described in Chapter 3 formed the initial basis for exploration of the Doppler sonar's capabilities. Each experiment was intended to investigate the effect of changing certain parameters, including target spacing, target speed, pulse length, pulse coding, lag, and target range. The parameters investigated in each experiment are shown in Table 4.1.

The basics of Doppler sonar performance can be reduced to two simple questions with potentially complicated answers: 'How good are the Doppler velocity estimates?'

Experiment	Target spacing	Lag	Pulse Length	Pulse coding	Target range	Comparison available?
Target-array	✓	✓	✓			✓
Short-range		✓	✓	✓		✓
Long-range 1		✓	✓	✓	✓	✓
Long-range 2		✓	✓	✓	✓	✓
Mobile field		✓	✓	✓		
Stationary field		✓	✓	✓	✓	✓
Silo tank						✓

Table 4.1: Overview of the parameters investigated in each experiment

and 'What is the finest achievable spatial resolution?' The quality of a Doppler velocity estimate can be quantified by examining the error (comparing of Doppler estimates with independent velocity estimates) and standard deviation (evaluating the Doppler velocity estimate standard deviation for a single target). Spatial resolution can be quantified by examining the success or failure of individual target identification with various target arrangements. Error, standard deviation, and spatial resolution will be examined in the context of expected fish swimming velocities in Section 6.2 to assess the possibility of making useful Doppler sonar measurements of fish swimming speed.

4.1 A word on statistics

The primary goal of the experiments was to determine the degree to which experimental parameters, such as target velocity or transmit pulse length, had an effect on the two objective measures of the quality of the Doppler velocity estimates: the error δ_v and the standard deviation σ_v.

The error δ_v is the difference between the mean Doppler velocity v and the true velocity v_{true} (measured independently)

$$\delta_v = v - v_{true} \tag{4.1}$$

and is a measurement of how well the true velocity is approximated by the Doppler velocity. Positive or negative values of δ_v indicate that the Doppler measurement overestimated or underestimated the true velocity, respectively. If there is no bias in the Doppler measurements, the value of δ_v averaged over multiple targets should be

zero within its margin of error. The absolute value of δ_v ($|\delta_v|$) can be used to gauge typical error by eliminating the tendency of δ_v with opposite signs to cancel each other out.

The standard deviation σ_v is the standard deviation in a Doppler velocity estimate for a single fish for which v_i are the N individual velocity estimates that are averaged to obtain v:

$$\sigma_v = \sqrt{\frac{1}{N-1}\sum_{i=1}^{N}(v_i - v)} \tag{4.2}$$

The standard deviation is an indication of the repeatability of individual velocity measurements. Averaging the standard deviation σ_v calculated for individual targets will provide measurements of typical standard deviation under given conditions. The uncertainty in the mean Doppler velocity $\sigma_{\overline{v}}$ is related to the standard deviation σ_v and the number N of velocity estimates used to calculate v by

$$\sigma_{\overline{v}} = \frac{\sigma_v}{\sqrt{N}} \tag{4.3}$$

A plot of error or standard deviation as a function of the experimental parameter of interest is the starting point for determining if some dependence is present. One could estimate by looking at the plot whether or not some kind of variation was present, but a more objective method is necessary. If there is no theoretical functional relationship, a first attempt to determine dependence is a linear regression (a fit to the equation $y = a_0 + a_1 x$). The regression results in estimates for the y-intercept a_0 and slope a_1, with corresponding uncertainties. A slope which is equal to zero within error would indicate no significant dependence on the factor being investigated.

A linear regression calculation results in three additional parameters with which

to assess dependence: the linear correlation coefficient r, the F-value, and the p-value (Wadsworth Jr., 1990). The linear correlation coefficient r lies between $+1$ and -1 and its square R is a measure of the degree of variance in the y-variable that is due to variance in the x-variable. Correlation of exactly $+1$ or -1 would indicate perfect linear dependence of y on x, with positive slope in the first case and a negative slope in the latter. The F-value is the ratio of the variance in the linear term to the residual variance, and the p-value is a measure of the probability of observing an F-value equal to or higher than the observed F-value, if the slope of the line is truly equal to zero. Therefore, low p-values indicate a higher probability of a nonzero slope. Generally, a 'level of significance' α is chosen to apply to the p-value: for $p < \alpha$, it may be reasonably concluded that the slope is nonzero, while if $p > \alpha$, the slope is likely to be zero (Mason et al., 2003). Typical values for α are 0.01–0.05; the value used in the following analyses is $\alpha = 0.01$.

4.2 Lag

Lag τ is a critical parameter of coherent Doppler sonar operation. Longer values of lag provide lower standard deviations but restrict maximum resolvable speed, while shorter values of lag provide higher resolvable speed with higher standard deviations, as expressed in Equation 2.32. In this section the dependence of the error δ_v and standard deviation σ_v on lag will be explored. Data from coded and uncoded pulses of all lengths were analyzed together since neither the error nor the standard deviation are affected by pulse length or coding to a significant degree (Section 4.5). For clarity and for comparison with experimental results, the standard deviation predicted by

Equation 2.32 will be written as σ_{vP}, while measured standard deviation will be written as σ_v.

The error is plotted as a function of lag in Figure 4.1a for all experiments. Parameters of linear fits to the datasets with more than two points, summarized in Table A.18, all have p-values greater than the level of significance $\alpha = 0.01$; therefore, the error does not depend on lag. In addition, the mean values of δ_v at each lag are small: all are less than $\pm 1\,\mathrm{cm\,s^{-1}}$, and 25% of the values of δ_v are equal to zero within their uncertainty.

Experimental standard deviation σ_v and theoretical standard deviation σ_{vP} are plotted as a function of lag in Figure 4.1b for all experiments. The standard deviation decreases with increasing lag in roughly the expected shape and magnitude predicted by Zrnic's Equation 2.32 (dotted line in Figure 4.1b). In general, fish targets resulted in $\sigma_v > \sigma_{vP}$ and styrofoam ball targets had $\sigma_v < \sigma_{vP}$, with the exception of the second long-range towtank experiment, for which $\sigma_v > \sigma_{vP}$. The theoretical line in Figure 4.1b was derived using the values for SNR and ρ calculated from averaging over all the experiments. Since σ_v also depends on SNR and ρ, the averaging has obscured some details of the relationship among σ_v and all three of τ, SNR, and ρ.

In order to avoid the pitfalls of too much averaging, the predicted standard deviation σ_{vP} was calculated for each individual target, using the lag, SNR, and ρ applicable to each target and Zrnic's Equation 2.32. The ratio R_{mp} of the measured to predicted standard deviation

$$R_{mp} = \frac{\sigma_v}{\sigma_{vP}} \tag{4.4}$$

was then calculated for each individual target. The mean value of the ratio for all targets was $R_{mp} = 1.001 \pm 0.004$, which is equal to 1 within uncertainty. Therefore,

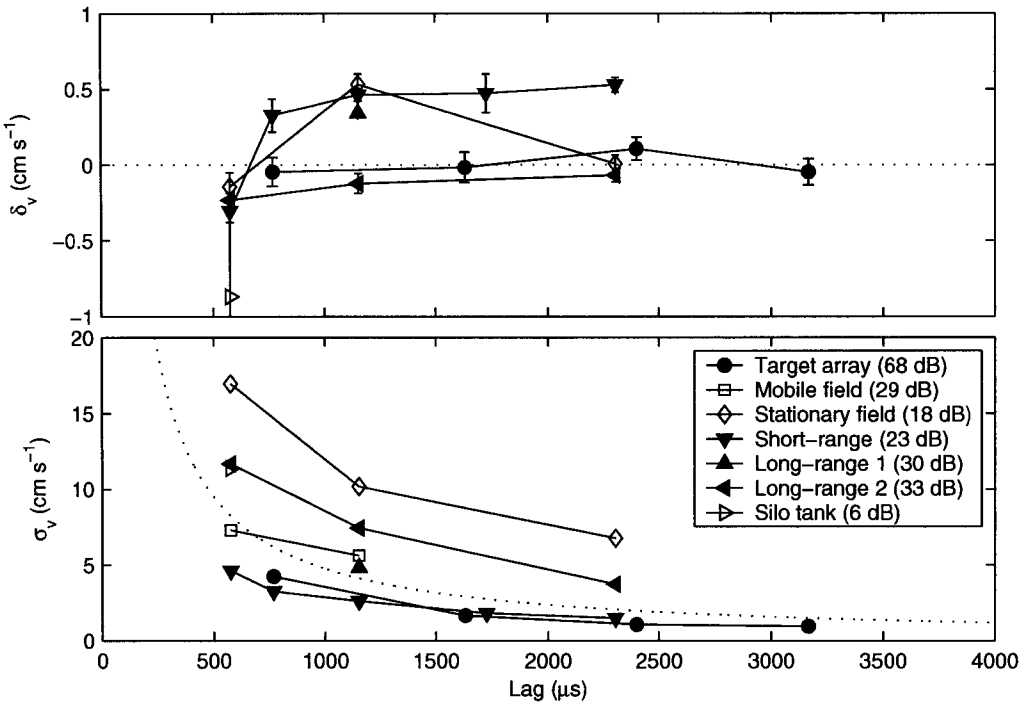

Figure 4.1: Plot of (a) δ_v (cm s^{-1}), (b) σ_v (cm s^{-1}) as a function of lag (μs) for each experiment: target-array experiment (•), mobile field experiment (□), stationary field experiment (◊), short-range experiment (▼), long-range experiment 1 (▲), long-range experiment 2 (◀), silo tank experiment (▷). The average SNR for each experiment is indicated in parentheses in the legend. Plot symbols indicate the target type: styrofoam balls (filled symbols) vs. fish (hollow symbols). The (dotted) theoretical line in (b) is calculated using Equation 2.32 and the average SNR and ρ. Error bars are smaller than the plot points at the scale in (b).

Zrnic's Equation 2.32 does a good job of predicting σ_v for a given lag, SNR, and ρ.

The effects of SNR and ρ, which have been averaged out in Figure 4.1, will be discussed in Section 4.7. For further examinations of σ_v dependence, datasets with different lags will be treated separately.

4.3 Target spacing

The limitations on spatial resolution were investigated by examining data from the target-array experiment (Section 3.4.1). The styrofoam targets within each group were separated by centre-to-centre spacings ranging from 5 cm to 60 cm (Table A.1). Taking into account the sizes of the targets and the relative angles between the sonar beam and the target arrays, the empty space *between* targets ranged between 2.3 and 55.4 cm, spanning the minimum spatial sampling interval of the sonar (7.2 cm).

4.3.1 Spatial resolution

Each trial was analyzed as described in Section 3.2 and once targets were identified by the data processing algorithm, the data were examined to determine whether individual targets were resolved in each target group. The smallest resolvable between-target spacing ΔR_{min} was noted for each pulse length, and ΔR_{min} is plotted as a function of pulse length expressed in both time (T) and equivalent range ($R_T = \frac{cT}{2}$) in Figure 4.2. Within the range of pulse lengths examined, the minimum resolvable target spacing as a function of pulse length R_T can be fit to a linear model, resulting in $\Delta R_{min} \approx 1.4\, R_T$. For the shortest pulse used in the target-array experiment (equal in length to the sampling interval of 7.2 cm), targets separated by 6.6 cm were re-

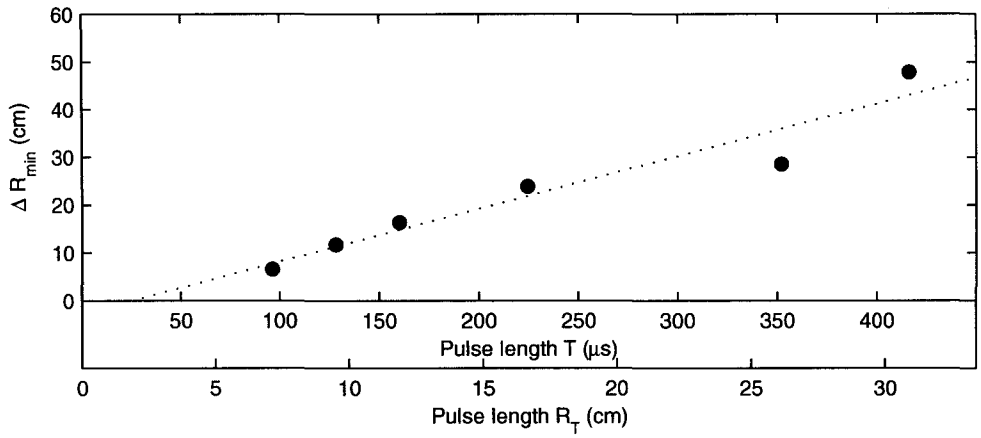

Figure 4.2: Minimum resolvable target spacing ΔR_{min} (cm) as a function of pulse length T (μs) and R_T (cm) for the target-array experiment. The equation of the fit line is $\Delta R_{min} = (1.4 \pm 0.2)R_T - (2.7 \pm 4.2)$ where $R_T = \frac{cT}{2}$ is the pulse length converted to an equivalent range.

solved on a single trial. The 6.6-cm spacing was the smallest target spacing for which individual targets were resolved in any experiment.

4.3.2 Velocity error and standard deviation

Velocity error δ_v and standard deviation σ_v were examined as a function of target spacing for target groups using datasets acquired with the same lag (768 μs) and different pulse lengths (96–416 μs).

The error and its absolute value $|\delta_v|$ as a function of target spacing are plotted as bar plots in Figures 4.3a and b, respectively, with different shading indicating different pulse lengths. The error is less than 2.5 cm s^{-1} except for the 60-cm target groups, where it is as high as 10.7 cm s^{-1}. The value of $|\delta_v|$ is less than 5 cm s^{-1} for target spacing of 40 cm or less, but is as large as 15 cm s^{-1} for the 60-cm target

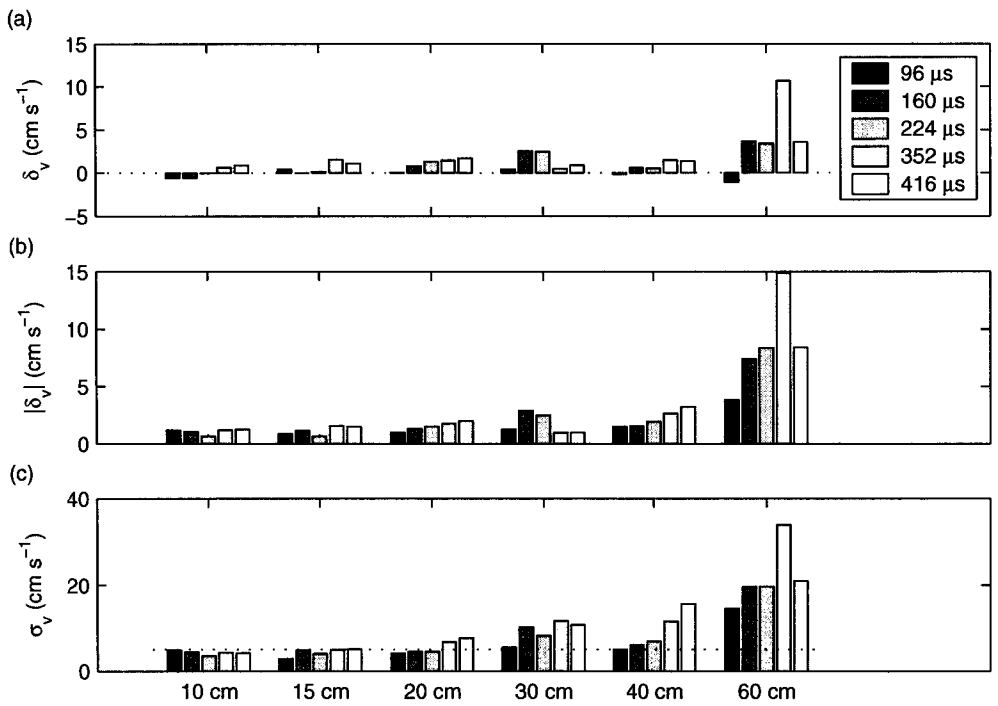

Figure 4.3: Bar plot of (a) δ_v (cm s^{-1}), (b) $|\delta_v|$ (cm s^{-1}), and (c) σ_v (cm s^{-1}) for different pulse lengths (see legend) and target groups of different spacings. All data were acquired with a lag $\tau = 768$ μs. The dotted line in (a) corresponds to $\delta_v = 0$.

spacing. The largest values of both δ_v and $|\delta_v|$ occur when the target spacing (60 cm) is nearly equal to the lag ($\tau = 768$ μs or 57 cm), as the backscatter from different targets adds and arrives at the sonar at the same time, and the phase information needed to extract the Doppler velocity is confounded.

Standard deviation is plotted as a bar plot in Figure 4.3c as a function of target spacing, with different shading indicating different pulse lengths. The combined effect of increasing pulse length and a lag of 57 cm (approximately equal to the 60-cm target spacing) resulted in a standard deviation which increased with pulse length when the

target spacing was 20 cm or greater. No increase is evident for the 10-cm and 15-cm target groups in Figure 4.3c. The increases in σ_v are larger for longer pulse lengths and greater target spacings, as these factors combine to result in overlap in the detected backscatter, and corruption of the phase information required to extract the Doppler velocity estimates.

Since both σ_v and δ_v in the target-array experiment are subject to interference caused by the spatial arrangements of the targets themselves, data from target groups subject to overlapping pulses (obliquely arranged with spacing of 20 cm or greater) were not used in inter-experiment comparisons.

4.4 Target velocity

Error δ_v and standard deviation σ_v were examined for dependence on true target velocity by analyzing data from several of the experiments. Since styrofoam balls and fish targets have significant differences (the styrofoam targets are not capable of independent motion), the two cases of towtank and live-fish experiments will be examined separately in Sections 4.4.1 and 4.4.2, respectively.

4.4.1 Tow velocity

Effects of tow velocity on error and standard deviation were investigated using the target-array experiment, the short-range experiment, and the two long-range experiments. Agreement between mean Doppler velocity and tow velocity for all the towtank experiments, regardless of velocity, is good. Taking into consideration each individual target, the error is less than ± 5 cm s^{-1} for 94% of targets, less than ± 3 cm s^{-1} for

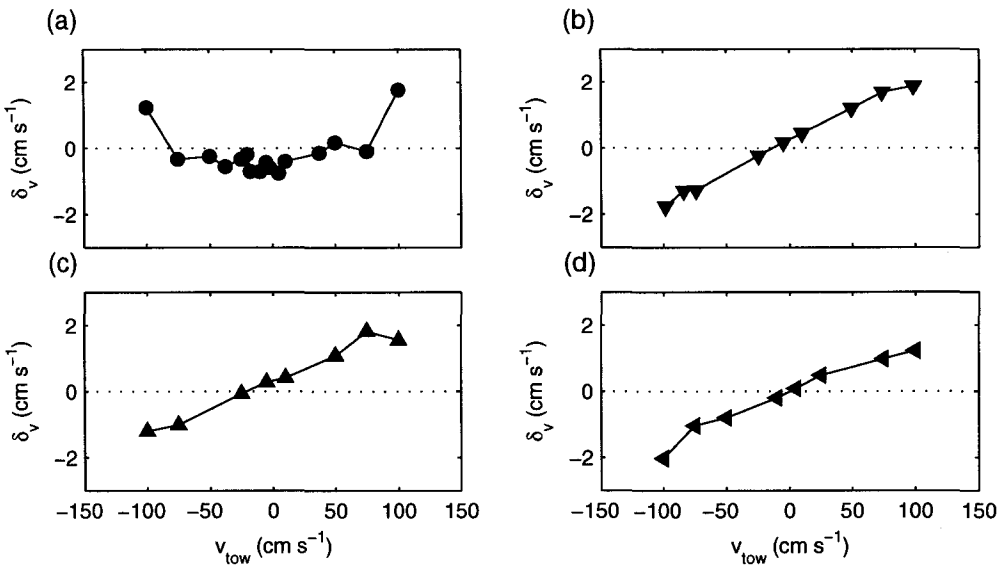

Figure 4.4: Plot of δ_v (cm s^{-1}) as a function of tow velocity v_{tow} (cm s^{-1}) for towtank experiments: (a) target-array experiment, (b) short-range experiment, (c) long-range experiment 1, (d) long-range experiment 2. Results for targets identified at a given tow velocity were averaged for each data point; error bars are smaller than plot markers at this scale.

84% of targets, and less than ± 1 cm s^{-1} for 47% of targets. The mean value of δ_v averaged over all targets is -0.1 ± 0.03 cm s^{-1}, which is small, but not equal to zero within uncertainty. The absolute values $|\delta_v|$ were averaged over all targets to get a typical value for the error of 1.84 ± 0.03 cm s^{-1}.

The error is plotted as a function of tow velocity in Figure 4.4 for the towtank experiments, and parameters from linear fits of δ_v as a function of v_{tow} are in Table A.19. For the short-range and long-range experiments, the linear dependence is significant ($p < \alpha$), and the magnitudes of the fitted slopes imply that the Doppler technique overestimates the velocity by approximately 2%. However, for the target-array experiment, there is no concrete relationship between δ_v and v_{tow} ($p > \alpha$).

There are three possible reasons for the bias in Doppler velocity estimates: uncer-

tainty in sound speed, asymmetry in the demodulation circuits in the sonar, or tank and geometry effects. The temperature, salinity, and pressure in each experiment were accurately known, and the water was well-mixed; therefore, errors in sound speed are not the cause of the bias. Asymmetry in the circuits used to extract the in-phase and quadrature values could cause such a bias; however, no bias was observed in the target-array experiment with the same instrument. The experimental geometry in the short-range and two long-range experiments is similar (horizontal beam), and differs significantly from that in the target-array experiment (oblique beam). Surface or bottom sidelobes and multiple reflections may have contaminated the backscatter in the short-range and long-range experiments, resulting in the bias observed in Figure 4.4.

The standard deviation is plotted as a function of tow velocity v_{tow} for lags of 576 μs in Figure 4.5a, 1152 μs in Figure 4.5b, and 2304 μs in Figure 4.5c. Parameters of linear fits to σ_v as a function of v_{tow} in Table A.19 revealed no significant dependence of σ_v on tow velocity ($p > \alpha$).

4.4.2 Fish velocity

Of the three live-fish experiments, no independent velocity estimate was available for the mobile field experiment, and the silo tank experiment did not cover a wide range of fish velocities (–18 cm s^{-1} to 12 cm s^{-1}). Therefore, error δ_v and standard deviation σ_v were examined as a function of fish swimming velocity using only the stationary field experiment dataset, with the assumption that the true velocity was equal to the independent swimming velocity estimate v_{slope}, described in Section 3.5.3. Values of the error and standard deviation for the 8813 identified fish were averaged into 5-cm

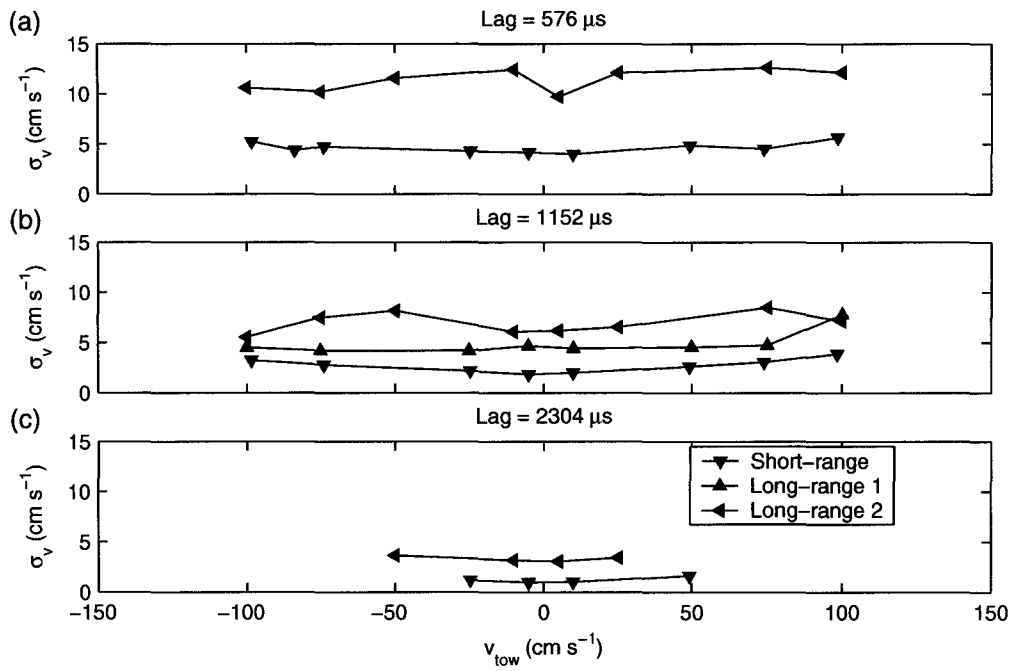

Figure 4.5: Plot of σ_v (cm s^{-1}) as a function of tow velocity v_{tow} (cm s^{-1}) for the towtank experiments: short-range experiment (▼), long-range experiment 1 (▲), long-range experiment 2 (◀). Results for σ_v were grouped by lag: (a) $\tau = 576\,\mu$s, (b) $\tau = 1152\,\mu$s, (c) $\tau = 2304\,\mu$s. Results for targets identified at a given tow speed were averaged for each data point; error bars are smaller than plot markers at this scale.

bins based on the corresponding value of v_{slope}, which was assumed to be the true swimming velocity v_{fish} relative to earth. Measurements of fish swimming velocity relative to the water velocity were not possible because of the poor quality of water velocity estimates in that particular location. Positive velocity values indicate fish swimming away from the sonar (upriver).

Figure 4.6 is a plot of the error as a function of fish swimming velocity. The data do not conform to a linear model (the fit parameters are given in Table A.20). There is, however, a rise in δ_v from ± 1 cm s^{-1} to $+5$ cm s^{-1} for v_{fish} between $40 - 80$ cm s^{-1}. The data points involved originate in three well-separated four-hour time periods over four days, suggesting that different fish behaviour at those times may have caused the discrepancy between v and v_{slope} not seen during other time periods. Anecdotal reports suggests that fish swimming behaviour changes as the river velocity varies with the tidal cycle. Attempts were made to extract current velocities from the Doppler sonar data after the fact; however, boundary effects, short pulse lengths, and interference from the surface and bottom combined to result in poor-quality current estimates from the Doppler sonar. There were no additional instruments deployed to measure current velocity, therefore no reliable current velocity measurements exist for that time period to determine whether the tidal current fluctuations are the source of the change in behaviour.

The standard deviation is plotted as a function of fish swimming velocity in Figures 4.7a, c, and e. The value of σ_v increased as the magnitude of the swimming velocity increased, so σ_v was averaged a second time using the swimming speed $|v_{fish}|$ instead of the velocity, and these data are plotted in Figures 4.7b, d, and f. Parameters of straight-line fits in Table A.20 indicate a dependence of σ_v on $|v_{fish}|$, as $p \ll \alpha$ for

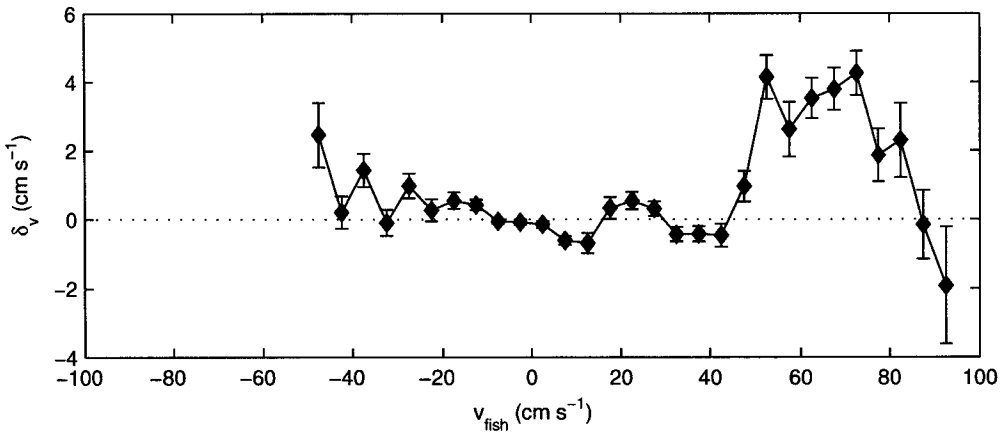

Figure 4.6: Plot of δ_v (cm s^{-1}) as a function of fish velocity v_{fish} (cm s^{-1}) for the stationary field experiment.

all three datasets. The value of the standard deviation increased as swimming speed increased, between 8 cm s^{-1} and 23 cm s^{-1} per m s^{-1} of fish swimming speed, with the largest increase occurring at the shortest lags. The minimum value of the standard deviation occurs when $|v_{fish}| = 0$ and is equal to the value of the standard deviation given by Zrnic's Equation 2.32 (dotted lines in Figure 4.7).

An important and obvious distinction between styrofoam balls and fish is that fish swim and have associated movements (tail-beats) which are proportional to swimming speed (Bainbridge, 1958). It is therefore likely that that the increase in σ_v with target speed not seen in towtank data is caused by the tail-beat motion of the swimming fish. The swimming motion would also account for the dependence of the standard deviation σ_v on speed (rather than velocity): whether the fish is swimming toward or away from the transducer, the swimming motion would be similar and should affect velocity estimates in a similar manner. The tail-beat effect is considered in more detail in Section 6.1.7.

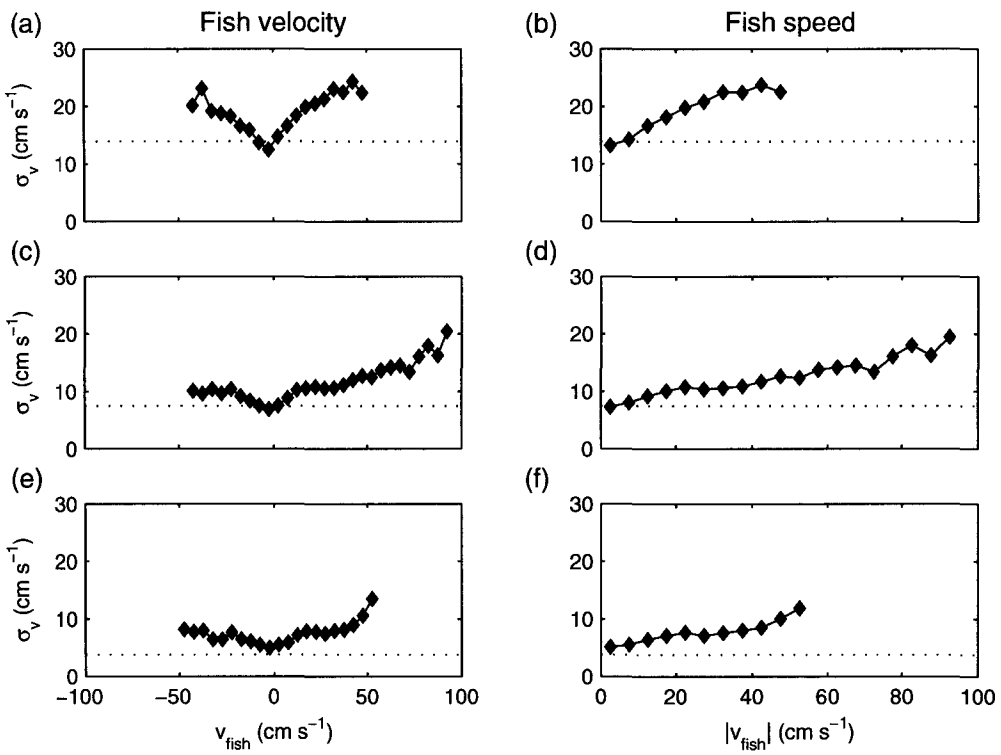

Figure 4.7: Plot of σ_v ($\mathrm{cm\,s^{-1}}$) as a function of fish velocity ($\mathrm{cm\,s^{-1}}$, first column) and fish speed ($\mathrm{cm\,s^{-1}}$, second column) for the stationary field experiment: (a) and (b) 576-μs lag, (c) and (d) 1152-μs lag, (e) and (f) 2304-μs lag. Dotted line indicates the predicted standard deviation based on Equation 2.32, calculated using mean values for SNR and ρ. Error bars are smaller than the plot markers at this scale.

4.5 Pulse length and pulse codes

The dependence of error δ_v and standard deviation σ_v on pulse length and pulse coding was investigated by examining data from those experiments in which more than one pulse length was used. Furthermore, it was necessary to have independent measurements of velocity available to calculate δ_v. These requirements excluded the mobile field experiment and silo tank experiment from the analysis of δ_v as a function of pulse length and coding, the former because no reference velocity was available, and the latter because only one pulse length was used. The target-array experimental results were excluded when investigating the effects of pulse coding, because only coded pulses were used.

Error is plotted as a function of pulse length in Figure 4.8 for the target-array experiment (a), the stationary field experiment (b), the short-range experiment (c), and the two long-range experiments (d, e). The linear fit parameters in Table A.21 reveal no dependence of δ_v on pulse length ($p > \alpha$).

In order to compare uncoded and coded pulses, the mean and standard error for δ_v were calculated in each experiment using all values of δ_v regardless of pulse length. Mean values of uncoded and coded δ_v agree within uncertainty for three of the four experiments (Table A.22); for the experiment in which they do not agree, the difference between the uncoded and coded values of δ_v is small (0.34 $\mathrm{cm\,s^{-1}}$). Therefore, it cannot be concluded that coded pulses provide different results for error δ_v than uncoded pulses.

The standard deviation at each pulse length for both coded and uncoded pulses was calculated and plotted as a function of pulse length for each lag τ in Figure 4.9. The linear fit parameters in Table A.23 reveal no dependence of σ_v on pulse length

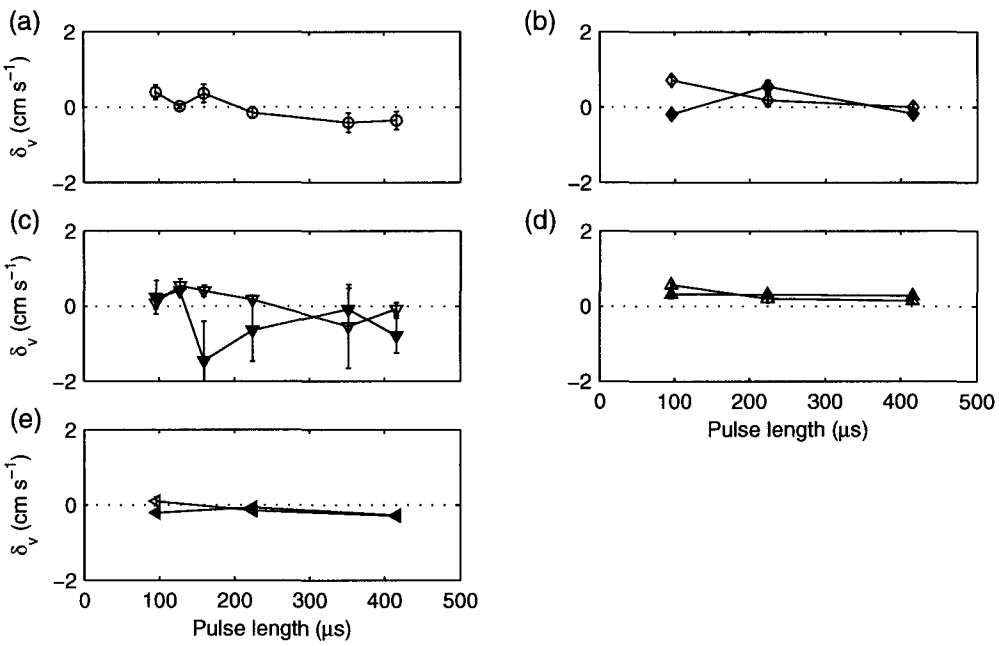

Figure 4.8: Plot of δ_v ($\mathrm{cm\,s^{-1}}$) as a function of pulse length (μs) for (a) target-array experiment, (b) stationary field experiment, (c) short-range towtank experiment, (d) long-range towtank experiment 1, (e) long-range towtank experiment 2. Filled symbols represent uncoded pulses while hollow symbols represent phase-coded pulses.

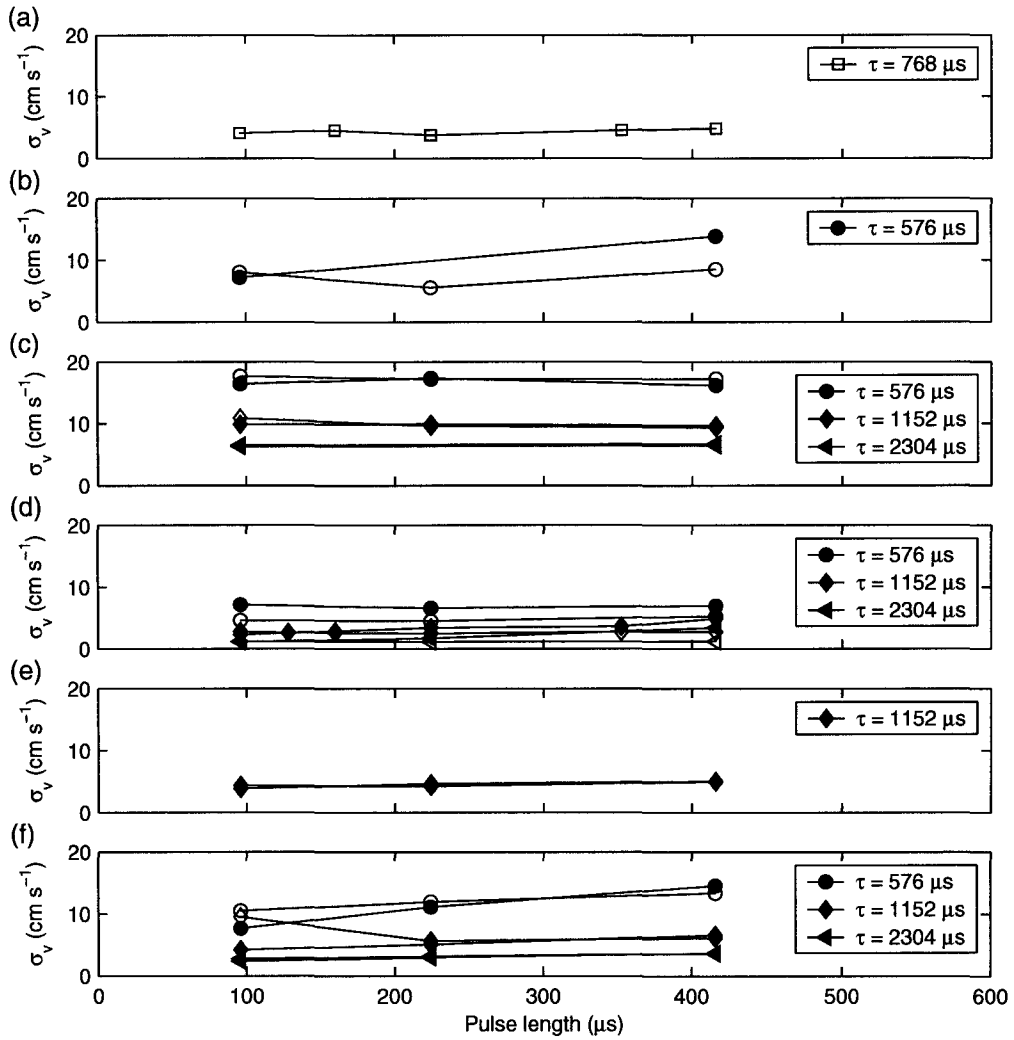

Figure 4.9: Plot of σ_v (cm s^{-1}) as a function of pulse length (μs) for uncoded pulses (filled symbols) and coded pulses (hollow symbols) for (a) target array experiment, (b) mobile field experiment, (c) stationary field experiment, (d) short-range towtank experiment, (e) long-range towtank experiment 1, (f) long-range towtank experiment 2. Error bars are smaller than the plot symbols at this scale, and lags are indicated in the legend on each plot.

($p > \alpha$).

In order to determine the effect of pulse coding on σ_v, all values of σ_v for a given lag and experiment were used to calculate mean and standard error for σ_v for both uncoded and coded pulses (Table A.24). Six of fourteen comparisons resulted in agreement between the observed values of σ_v for uncoded and coded pulses. For the remaining eight comparisons, the differences ranged between -1.6 and $+2.1$ cm s^{-1}, and the uncoded σ_v was not consistently larger or smaller than the coded σ_v. Therefore, pulse coding does not have any quantifiable or consistent effect on measured values of σ_v.

4.6 Target Range

Three experiments, the stationary field experiment and the two long-range towtank experiments, were designed to investigate the behaviour of Doppler velocity estimates as a function of range to the target.

Error is plotted as a function of target range in Figure 4.10 for the stationary field experiment (a) and the long-range towtank experiments (b, c). Over all three experiments, 93% of the mean values for δ_v at a given range were less than ± 1 cm s^{-1} and 38% were equal to zero within uncertainty. In the stationary field experiment, surface and bottom reflections caused the values of δ_v to increase to ± 1 cm s^{-1} for ranges less than 20 m; δ_v also increased at ranges greater than 60 m (Figure 4.10a). In the first long-range experiment, δ_v is less than ± 0.5 cm s^{-1} with the exception of the 35-m data point (Figure 4.10b). In the second long-range experiment, δ_v is less than ± 0.5 cm s^{-1} for ranges less than 60 m, and δ_v increases to ± 1 cm s^{-1} for ranges

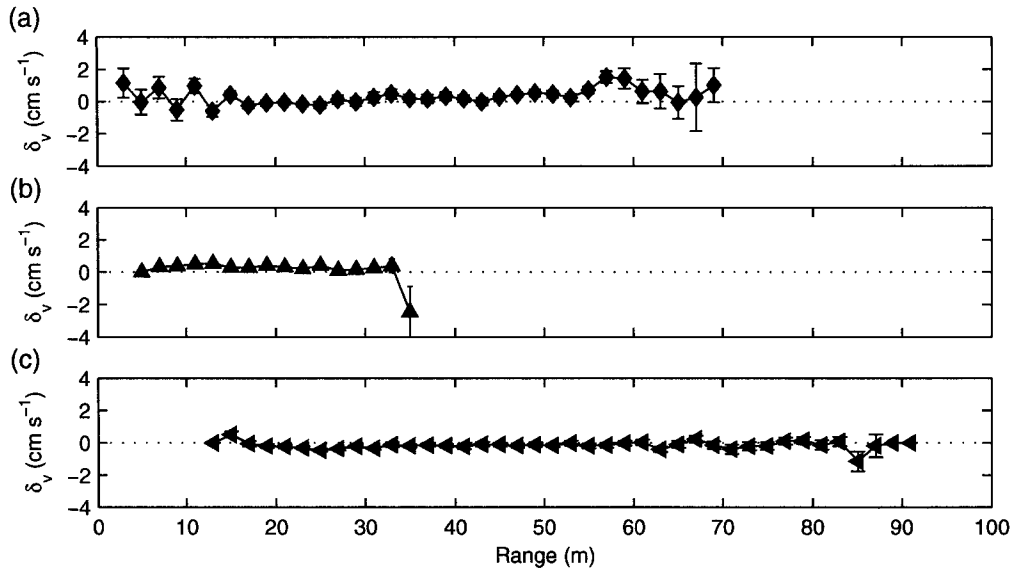

Figure 4.10: Plot of δ_v (cm s^{-1}) as a function of target range (m) for the three long-range experiments: (a) Stationary field experiment, (b) Long-range towtank experiment 1, (c) Long-range towtank experiment 2.

greater than 60 m (Figure 4.10c). Parameters of linear fits of δ_v as a function of range in Table A.25 reveal that δ_v does not depend on range in a systematic way ($p > \alpha$).

Standard deviation is plotted as a function of range in Figure 4.11 for the stationary field experiment (a) and the two long-range experiments (b, c), with different plot symbols for each lag. The SNR is plotted as a function of range in Figure 4.11d, with hollow plot symbols used to highlight the ranges at which SNR < 30 dB. In the stationary field experiment, σ_v remained essentially constant with range, while in the long-range 1 and 2 towtank experiments, σ_v began to increase at 19 m and 47 m range, respectively, as indicated by arrows in Figures 4.11b and c. The range at which σ_v began to increase corresponded roughly to the range at which SNR fell below 30 dB (Figure 4.11d), and is different for the two tanks because of the differing

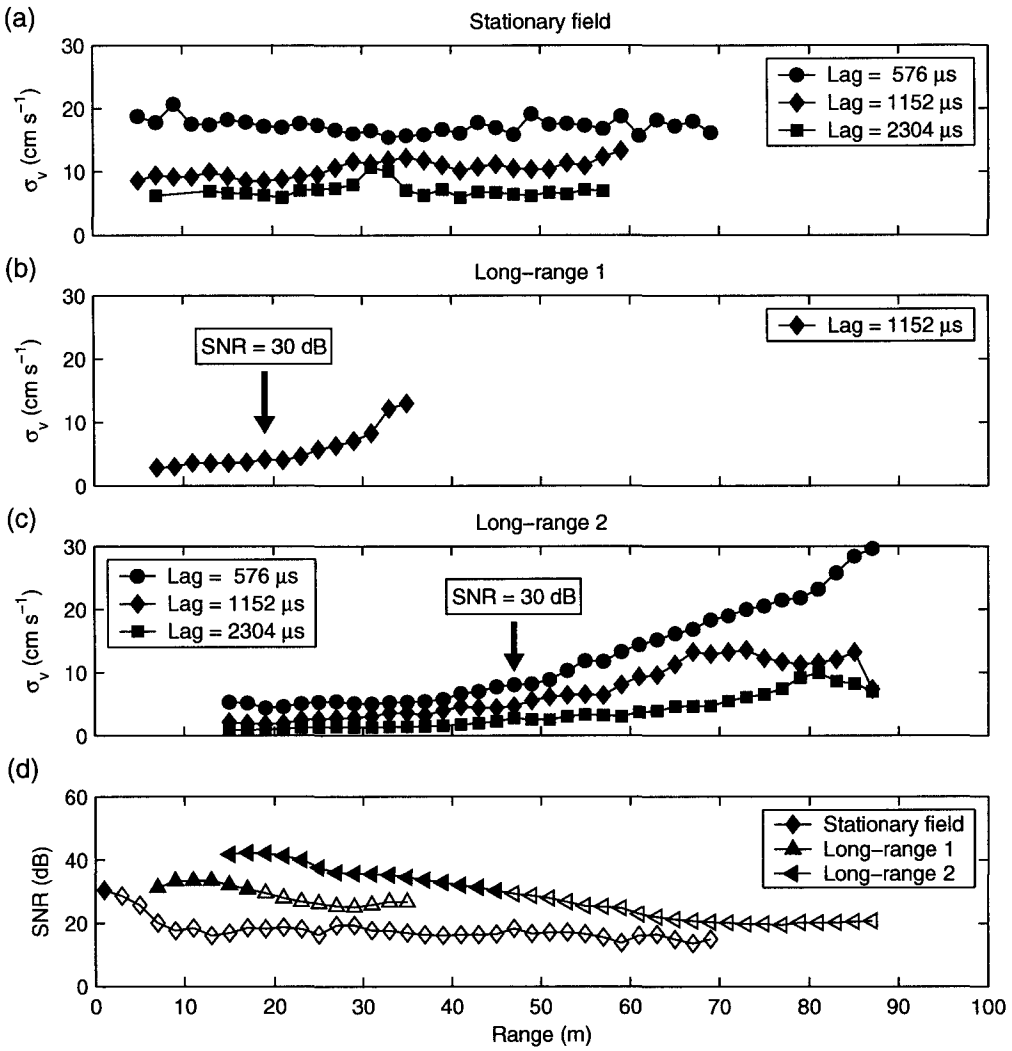

Figure 4.11: Plot of σ_v (a)–(c) (cm s^{-1}) and SNR (d) as a function of target range. (a) σ_v for stationary field experiment, (b) σ_v for long-range towtank experiment 1, (c) σ_v for long-range towtank experiment 2, (d) SNR for all three experiments, with hollow plot markers for SNR < 30 dB. Plot symbols represent different lags in (a)–(c), and different experiments in (d), as given by the legends. Uncertainties were smaller than the plot markers at this scale.

geometries. The SNR for the stationary field experiment is below 30 dB at most ranges, and the values of σ_v are essentially constant with range. Furthermore, values of σ_v from the stationary field experiment at the same lags as the two long-range experiments are comparable in magnitude to those observed in the sub-30-dB ranges in the towtank experiments (Figure 4.11d).

4.7 SNR and ρ

Results in Sections 4.2 and 4.6 have demonstrated that standard deviation depends on lag, SNR, and ρ in a complicated way. Experimental results for σ_v were in reasonable agreement with theoretical results calculated using Equation 2.32 on a target-by-target basis (Section 4.2). The fact that SNR decreases with increasing range, and σ_v increases with increasing range (Section 4.6) allows for a further examination of error and standard deviation as a function of both SNR and ρ.

Data from all experiments were combined, and values of δ_v and σ_v for each target were grouped by SNR and averaged into bins of size $\Delta\text{SNR} = 2$ dB. The error does not depend on lag (Section 4.2), so all error data were grouped together regardless of lag, and δ_v is plotted as a function of SNR in Figure 4.12a. Results for standard deviation were subdivided by lag, using the three lags with the largest datasets, and σ_v is plotted as a function of SNR in Figures 4.12b, c, and d, for lags of 576 μs, 1152 μs, and 2304 μs, respectively.

For SNR > 7 dB, the absolute value of the error $|\delta_v|$ is smaller than 0.5 cm s^{-1} (Figure 4.12a). Parameters of a linear fit in Table A.26 reveal a small dependence of δ_v on SNR of -0.008 ± 0.004 cm s^{-1}/dB ($p < \alpha$), amounting to a decrease of

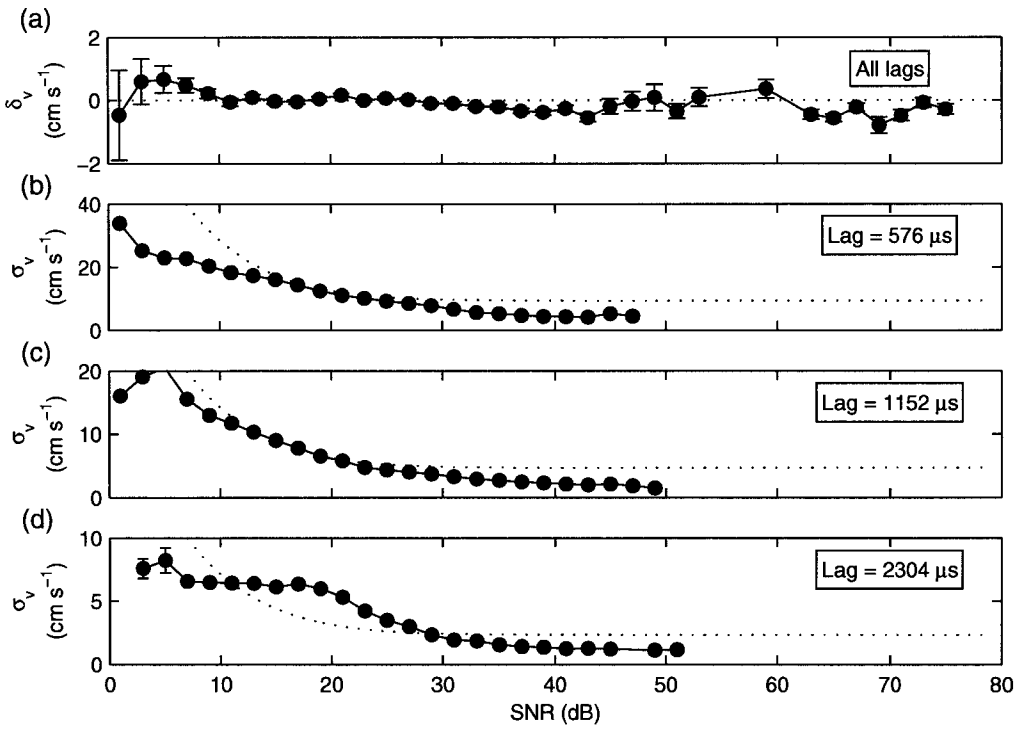

Figure 4.12: Plot of (a) δ_v (cm s^{-1}) for all lags, (b) σ_v (cm s^{-1}) for $\tau = 576$ μs, (c) σ_v (cm s^{-1}) for $\tau = 1152$ μs, (d) σ_v (cm s^{-1}) for $\tau = 2304$ μs, all as a function of SNR. Dotted lines in (b)–(d) are the predicted standard deviations σ_{vP} calculated with mean ρ. Uncertainties were smaller than the plot markers at this scale.

0.64 cm s^{-1} over the 80-dB range of SNR which was studied.

The measured standard deviation follows the general shape of the theoretical standard deviation σ_{vP} as a function of SNR (dotted lines in Figure 4.12b–d). For the 576 and 1152-μs lags and values of SNR between 10–30 dB, σ_v is equal to σ_{vP}, while for SNR less than 10 dB and SNR greater than 30 dB, measured σ_v is smaller than σ_{vP}. For the 2304-μs lag, σ_v exceeds the predicted value for $10 < \text{SNR} < 30$ dB; the higher-σ_v data in this region originates primarily from fish targets, suggesting that swimming motion was responsible for the increased σ_v relative to σ_{vP}.

The dependence of δ_v and σ_v on the complex correlation coefficient ρ was investigated by again combining data from all experiments. Values of δ_v and σ_v for each target were averaged in bins of size $\Delta\rho = 0.005$ and plotted as a function of ρ. Figure 4.13a is a plot of δ_v as a function of ρ, and Figures 4.13b, c, and d, are plots of σ_v as a function of ρ for lags of 576 μs, 1152 μs, and 2304 μs, respectively. Linear fit parameters in Table A.26 reveal that there is no significant dependence of δ_v on ρ ($p > \alpha$). The standard deviation σ_v depends strongly on ρ, which is expected based on Equation 2.32; however, when the effects of SNR are averaged out, the standard deviation σ_v is greater than the predicted standard deviation σ_{vP} by a factor of approximately 1–4. The lower-ρ data points, where the difference between σ_v and σ_{vP} is greater, originate primarily from swimming fish rather than styrofoam targets, which again suggests that fish motion causes an increase in σ_v relative to the predicted value σ_{vP}. Effects of fish swimming motion will be addressed in greater detail in Section 6.1.7.

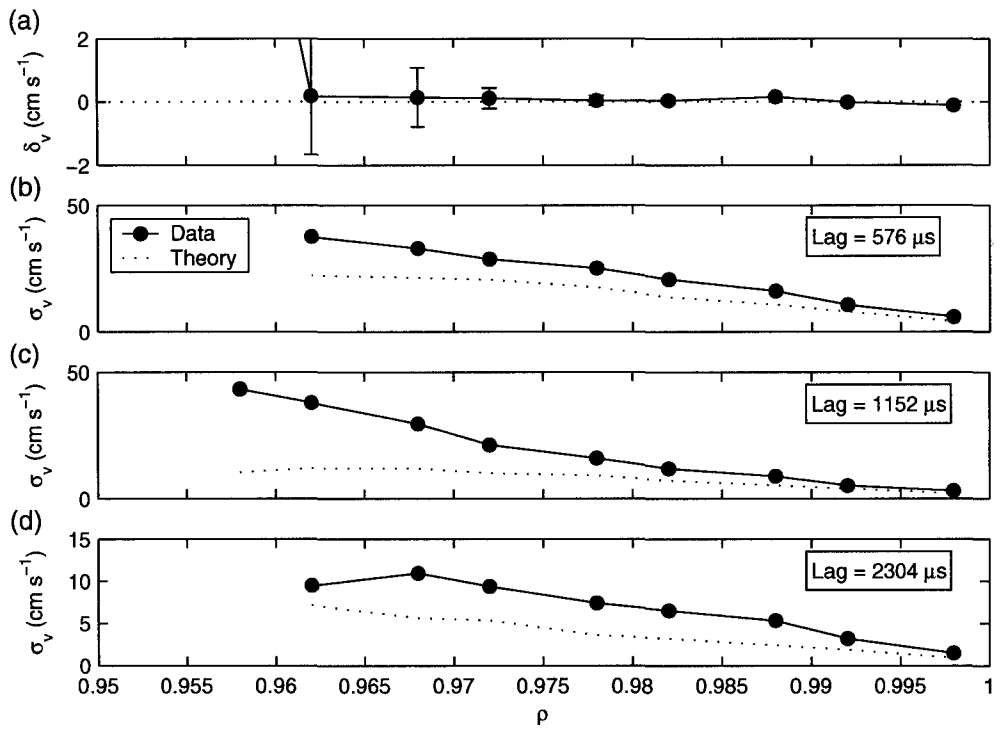

Figure 4.13: Plot of (a) δ_v ($\mathrm{cm\,s^{-1}}$) for all lags, (b) σ_v ($\mathrm{cm\,s^{-1}}$) for $\tau = 576$ μs, (c) σ_v ($\mathrm{cm\,s^{-1}}$) for $\tau = 1152$ μs, (d) σ_v ($\mathrm{cm\,s^{-1}}$) for $\tau = 2304$ μs, all as a function of ρ. Dotted lines in (b)–(d) are the predicted standard deviations σ_{vP} calculated with mean SNR. Uncertainties were smaller than the plot markers at the scale in (b)–(d).

4.8 Summary of Experimental Results

The experimental results have determined which sonar and target parameters have a significant effect on the quality of Doppler velocity estimates, as measured by both the error and standard deviation. In addition, the sonar spatial resolution was explored through the target-array experiment.

Spatial resolution is affected by the pulse length. With the transmit pulse length equal to the maximum spatial sampling rate for the test instrument of 7.2 cm, targets with 6.6 cm of space between them were differentiated in the backscatter data. The minimum resolvable target spacing ΔR_{min} rose linearly with pulse length T, $\Delta R_{min} \approx 1.4 R_T$ ($R_T = \frac{cT}{2}$). Target spacing also affected the quality of Doppler velocity measurements. Both error and standard deviation increased when the target spacing, pulse length, and lag combined to result in targets overlapping in the backscatter.

Pulse length and coding do not have a measurable effect on either error or standard deviation. The error is not affected by the choice of lag (discounting possible aliasing), and the standard deviation depends on lag approximately as predicted by Zrnic (1977). Target velocity has a small effect on error in some of the towtank experiments, with the Doppler velocity slightly overestimating the true velocity; however, there is no dependence of Doppler velocity on target velocity in the field data. Target velocity does not affect standard deviation in the towtank experiments, but the standard deviation increases with increasing target speed in the field experiments, which may be caused by the fish's body motion. Target range affects the SNR and therefore the standard deviation, with the dependence approximately following that predicted by Zrnic (1977); however, target range has no effect on the error.

The ranges of parameters explored through the experiments has raised further questions regarding Doppler sonar performance in a number of situations not accessible with the current instrument. One way to extend investigation of Doppler sonar performance is to design a computer model of sonar operation. A model was constructed for this purpose and verified by comparing model results with experimental results where possible. The model was then extended to investigate some effects not studied in detail in the experiments, including changes in bandwidth and multiple strong targets simultaneously in the beam. The following chapter describes the programming and results of the computer model in detail.

Chapter 5

Model Results

The computer model was designed to extend the understanding of the sonar operation, with four specific goals to fulfill. First, the model was used to confirm experimental results for standard deviation and error. Second, the model was used to explore the effects of changing some experimental parameters which were difficult to control in the field and laboratory, such as SNR, multiple target and water velocities, a wider range of lags, pulse lengths, and coding. Third, the model was meant to assist in explaining the discrepancy observed between Zrnic's theoretical treatment and experimental observations at low SNR. Fourth, the model allowed for investigation of some situations not accessible with the current Doppler system, in particular, the effects of changes in bandwidth, and the occurrence of multiple strong targets simultaneously in the beam.

5.1 Model design

The coherent Doppler sonar model was implemented using the Matlab programming environment, and consisted of three main parts: pulse construction, hardware simulation, and post-processing. In the pulse construction phase, the pressure wave resulting from interaction of the transmitted pulse with one strong target (the fish) and several weaker targets (the water) was constructed. In the hardware simulation phase, the modelled pressure wave was treated as it would be in the signal processing electronics in the sonar. In the post-processing phase, the target velocity estimates were generated for comparison with the known target velocity by applying the same data processing schemes used with actual data. Model parameters, which will be fully explained in the following sections, are summarized in Table 5.1, for both a

Parameter	**Narrowband value**	**Broadband value**
Transmit frequency (f_0)	250 kHz	
Ping rate	3.125 Hz	
Transmit bandwidth (BW_{Xmt})	30 kHz	125 kHz
Receive bandwidth (BW_{rec})	21.7 kHz	125 kHz
Final sampling frequency (f_s)	10.4 kHz	250 kHz
Final sampling interval (Δt_s)	96 μs	4 μs
Model sampling frequency (f_m)	16 MHz	
Model time increment (Δt_m)	62.5 ns	
Number density of weak targets (n_p)	20 m^{-1}	
Filter order (O_{filt})	4	
Sound speed (c)	1480 m s^{-1}	
Starting target range	20 m $\pm 10\lambda$	
Time in beam for strong target	10 s	
Number of repetitions (n_{rep})	50	

Table 5.1: Parameters and sonar settings used in the computer model of narrowband and broadband sonar response

Parameter	Default value	Values used
Lag	1152 μs	384 to 3264 μs
Pulse length	224 μs	32 to 640 μs
Pulse codes	No code	Uncoded pulses or Barker codes of length 2, 3, 5, 7, 11, 13 elements
Strong target velocity	+50 cm s^{-1}	−100 to +100 cm s^{-1}
Strong target Δ_v	0 cm s^{-1}	0 to +20 cm s^{-1}
Weak target velocity	0 cm s^{-1}	−100 to +100 cm s^{-1}
Weak target Δ_v	0 cm s^{-1}	0 to +20 cm s^{-1}
Weak target strength (A_{rel})	−30 dB	−80 to 0 dB

Table 5.2: Default parameters and the variations used in the computer model of sonar response

narrowband and broadband version of the computer model. Default values for the parameters are given in Table 5.2, and the choice of default values is discussed in greater detail in Section 5.1.4.

5.1.1 Pulse construction

The pulse construction phase consisted of coherently adding the backscatter which would result when a pair of transmit pulses were scattered from various point targets. The targets consisted of a single strong target, representing the fish, and a number of weak targets, representing water. No beam-width or target-size effects were taken into account, resulting in a 1-dimensional model.

A transmit pulse template was created by sampling a sine wave of frequency f_0 at the model sampling frequency f_m (corresponding to time step Δt_m) for a duration equal to the pulse length T. The sampled pulse was zero-padded up to $2 \times T$ on either

side to reduce filter end-effects:

$$s(t_i) = \begin{cases} 0, & -2T < t_i \leq 0 \\ \sin(2\pi f_0 t_i), & 0 < t_i \leq T \\ 0, & T < t_i < 3T \end{cases} \tag{5.1}$$

If the pulse was to be coded, the pulse elements corresponding to the code elements with a 180° phase shift were multiplied by -1. The sonar transmit bandwidth was simulated by filtering $s(t_i)$ with a Butterworth filter of bandwidth BW_{Xmt} and order O_{filt}.

The start position for the fish on the first ping was randomly selected to lie in an interval of $\pm 10\lambda$ about the desired starting range. This dithering of start position was needed to eliminate possible errors from beginning each model execution with the same nonzero phase. The position of the fish for each ping was calculated based on the input fish velocity, resulting in a minimum, mean, and maximum fish range. The backscattered pulse $S(t)$ was simulated for a range extending to $\pm 2\tau$ on either side of the maximum and minimum fish range, with the number of weak targets M needed for the simulation calculated based on the desired number of weak targets per metre n_p (Section 5.1.4). Therefore, a total of $M + 1$ targets were added to $S(t)$.

With the pulse-pair transmit scheme, two pulses separated by a lag τ are transmitted. Therefore the j^{th} target with velocity v_j will be insonfied twice by the transmit pulses, once when at its initial position $R_{1,j}$, and a second time at position $R_{2,j}$, the location of the target after a time τ:

$$R_{2,j} = R_{1,j} + \tau v_j \tag{5.2}$$

The backscattered pulses, which were transmitted a time τ apart, will arrive at the sonar at times $t_{1,j}$ and $t_{2,j}$:

$$t_{1,j} = \frac{2R_{1,j}}{c} \tag{5.3}$$

$$t_{2,j} = \frac{2R_{2,j}}{c} + \tau \tag{5.4}$$

For each target, Equations 5.2, 5.3, and 5.4 were used to calculate where to place the transmit pulse s in the backscattered pulse S. Paradoxically, no Doppler shift was applied when assembling the backscattered pulse, since the pulse-pair technique depends on the phase shift between the two pulses to determine velocity. Computation time would have increased in proportion to the number of velocities present if a frequency shift had been included. Fish targets were given an amplitude A of unity, while water targets had an amplitude A_{rel} ranging from –80 dB to 0 dB relative to the fish:

$$A_j = \begin{cases} 1 & \text{(fish)} \\ 10^{A_{rel}/20} & \text{(water)} \end{cases} \tag{5.5}$$

The backscattered pulse $S(t)$ was built by recursively adding $s(t)$ to $S(t)$ with appropriate amplitude A_j at times $t_{1,j}$ and $t_{2,j}$:

$$S(t_{1,j}) = S(t_{1,j}) + A_j\, s(t) \tag{5.6}$$

$$S(t_{2,j}) = S(t_{2,j}) + A_j\, s(t) \tag{5.7}$$

An example of $S(t)$ constructed by applying Equations 5.6 and 5.7 is plotted in Figure 5.1.

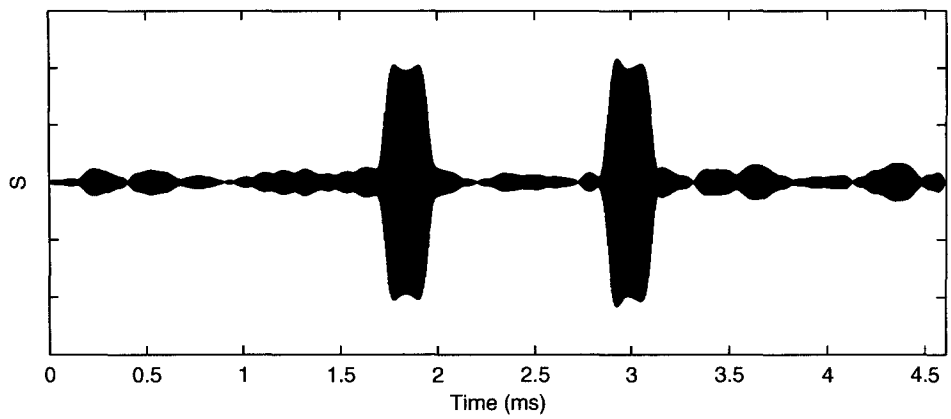

Figure 5.1: Sample of backscattered pulse S (arbitrary units) as a function of time (ms) produced by the narrowband model with the default settings (Tables 5.1 and 5.2). The fish targets correspond to the higher-amplitude regions near 1.8 ms and 3.0 ms. The smaller-amplitude regions contain 20 randomly spaced weak targets m^{-1}.

With minor alterations, the model could also be configured to reproduce volume backscatter. The model domain in the volume backscatter configuration was a fixed length of 4τ; targets which moved out of the domain between pings were re-introduced at the opposite side of the domain. The strong target was omitted from pulse construction, and only the equal-amplitude weaker targets were placed in the backscattered pulse. Velocity estimates were taken from the centre of the model domain to avoid the reduction in inter-particle interference at the edges of the domain.

In both the fish and water-only cases, the backscattered pulse created using Equations 5.6 and 5.7 was receive-filtered, using a Butterworth filter of order O_{filt} and bandwidth BW_{rec}. In a real sonar system, the observed backscatter suffers from transmission loss due to both range-spreading and attenuation, and corrections are applied in either the signal processing electronics or post-processing stage to account

for these effects. In the model, accounting for and then correcting for transmission loss would result in no net change to the modelled signal; thus, neither the transmission loss nor the subsequent corrections were included in the model. Therefore, at this stage in the model, $S(t)$ represents the received backscatter with no beam-spreading or attenuation effects, and the pulse is ready to have the Doppler signal extracted by the hardware simulation portion of the program.

5.1.2 Hardware simulation

5.1.2.1 Intensity

The backscatter intensity was calculated in order to differentiate target samples from water, as in the experiments. The envelope S_{rect} of the received pressure wave was extracted first by rectifying it:

$$S_{rect}(t) = |S(t)| \tag{5.8}$$

Following the rectification, a low-pass filter was applied. The signal was then sampled at the final sonar sampling rate f_{sonar} and converted to decibels relative to an arbitrary reference level, with an added constant to shift the backscatter to positive values, for consistency with real sonar data and ease of interpretation:

$$S_{dB} = 20 \log_{10} |S| + 255 \tag{5.9}$$

5.1.2.2 Complex Demodulation

The complex demodulation which takes place in the test instrument is an analog process: no digital sampling takes place until the cosine and sine (in-phase and quadrature) signal components have been generated in an analog circuit. Implementing the analog quadrature demodulation in the model resulted in slow model execution because multiple filters were required for the calculation. Instead, a digital quadrature demodulation process was implemented in the model, which gives equivalent results with less computation time (Ziomek, 2002).

Analog quadrature demodulation is a standard signal processing technique used to extract the in-phase I (cosine) and quadrature Q (sine) components of a received signal (Rickey, 2000). Recall that the multiplication of two sinusoidal signals of frequency f_1 and f_2 can be written as the sum of two signals, one containing the difference frequency $f_1 - f_2$ and one containing the sum frequency $f_1 + f_2$:

$$\sin(2\pi f_1 t) \times \cos(2\pi f_2 t) = \frac{1}{2}[\cos(2\pi(f_1 - f_2)t) + \cos(2\pi(f_1 + f_2)t)] \quad (5.10)$$

$$\sin(2\pi f_1 t) \times \sin(2\pi f_2 t) = \frac{1}{2}[\cos(2\pi(f_1 - f_2)t) - \cos(2\pi(f_1 + f_2)t)] \quad (5.11)$$

Quadrature demodulation exploits the relationships in Equations 5.11 and 5.10, beginning with the multiplication of the received signal $S(t) = \sin(2\pi f t + \phi)$ with frequency $f = f_0 + f_d$ and phase shift ϕ by reference sine and cosine signals:

$$I(t) = S(t)\cos(2\pi f_0 t) \quad (5.12)$$

$$Q(t) = S(t)\sin(2\pi f_0 t) \quad (5.13)$$

The reference signals are generated at the transmit frequency f_0 and have the same phase as the transmit signal. The I and Q signals resulting from Equations 5.12 and 5.13 have sum ($f_0 + f = 2f_0 + f_d$) and difference ($f_0 - f = -f_d$) components given by application of Equations 5.11 and 5.10

$$I(t) = \frac{1}{2}\left[\cos\left(2\pi f_d t + \phi\right) + \cos\left(2\pi\left(2f_0 + f_d\right)t + \phi\right)\right] \quad (5.14)$$

$$Q(t) = \frac{1}{2}\left[\cos\left(2\pi f_d t + \phi\right) - \cos\left(2\pi\left(2f_0 + f_d\right)t + \phi\right)\right] \quad (5.15)$$

The multiplication in Equations 5.14 and 5.15 is followed by application of a low-pass filter with cutoff F_{demod} and order O_{filt}, which eliminates the sum component (frequency $2f_0 + f_d$) and retains only the difference component (frequency f_d) which contains the Doppler shift.

The filter operations are computationally time-consuming. An alternative approach is digital quadrature demodulation, also known as digital downconversion, which omits the multiplication and filtering steps altogether by sampling the digital signal at exactly four times the transmit frequency (Ziomek, 2002). Consider a signal of the form $S(t) = \sin(2\pi ft + \phi)$, evaluated at times $t = 0, \frac{1}{4f}, \frac{1}{2f}, \frac{3}{4f}$:

$$\begin{aligned}
S(0) &= \sin\left(2\pi f\left(0\right) + \phi\right) &&= \sin(0 + \phi) &&= \sin(\phi) \\
S\left(\tfrac{1}{4f}\right) &= \sin\left(2\pi f\left(\tfrac{1}{4f}\right) + \phi\right) &&= \sin(\tfrac{\pi}{2} + \phi) &&= \cos(\phi) \\
S\left(\tfrac{1}{2f}\right) &= \sin\left(2\pi f\left(\tfrac{1}{2f}\right) + \phi\right) &&= \sin(\pi + \phi) &&= -\sin(\phi) \\
S\left(\tfrac{3}{4f}\right) &= \sin\left(2\pi f\left(\tfrac{3}{f}\right) + \phi\right) &&= \sin(\tfrac{3\pi}{2} + \phi) &&= -\cos(\phi)
\end{aligned}$$

The result of sampling at four times the transmit frequency is the sequence $\sin(\phi)$, $\cos(\phi)$, $-\sin(\phi)$, $-\cos(\phi)$, corresponding to I, Q, $-I$, and $-Q$, from which the I and Q samples can then be extracted at the desired sampling frequency. Two minor

restrictions arise from the application of digital demodulation: the model timestep must be an integral fraction of the transmit period, and the maximum possible final sampling frequency will be equal to the transmit frequency f_0.

Figure 5.2a is a false-colour image of the difference between analog-demodulated Doppler velocity v_A and digitally-demodulated Doppler velocity v_D for a typical modelled fish. The difference $v_A - v_D$ is -0.45 ± 0.53 cm s^{-1} for all the modelled data in Figure 5.2a, and -0.1 ± 0.4 cm s^{-1} for the samples between the black lines, which are the samples that originate from the fish. In both cases, the difference $v_A - v_D$ is equal to zero within uncertainty. Greater detail can be seen in Figures 5.2b and c, which is a plot comparing v_A and v_D for the two modelled pings indicated in red in Figure 5.2a.

Digital demodulation provides Doppler velocity estimates which are equal within uncertainty to those obtained with analog demodulation. Therefore, to reduce computation time, digital demodulation was used in the Doppler sonar model.

5.1.3 Post-processing

Sine, cosine, and intensity signals were sampled for each ping and saved into output matrices. Mean Doppler velocity, standard deviation, correlation coefficient, and SNR were calculated by combining the velocity samples into a single dataset for the entire time the fish is in the beam, as in the experiments. The fish position on a given ping was identified using the known fish location and taking into account the pulse length. Samples originating from the fish were thresholded using intensity and correlation thresholds, and the Doppler velocity statistics for the series of pings were calculated in exactly the same way as in the experiments.

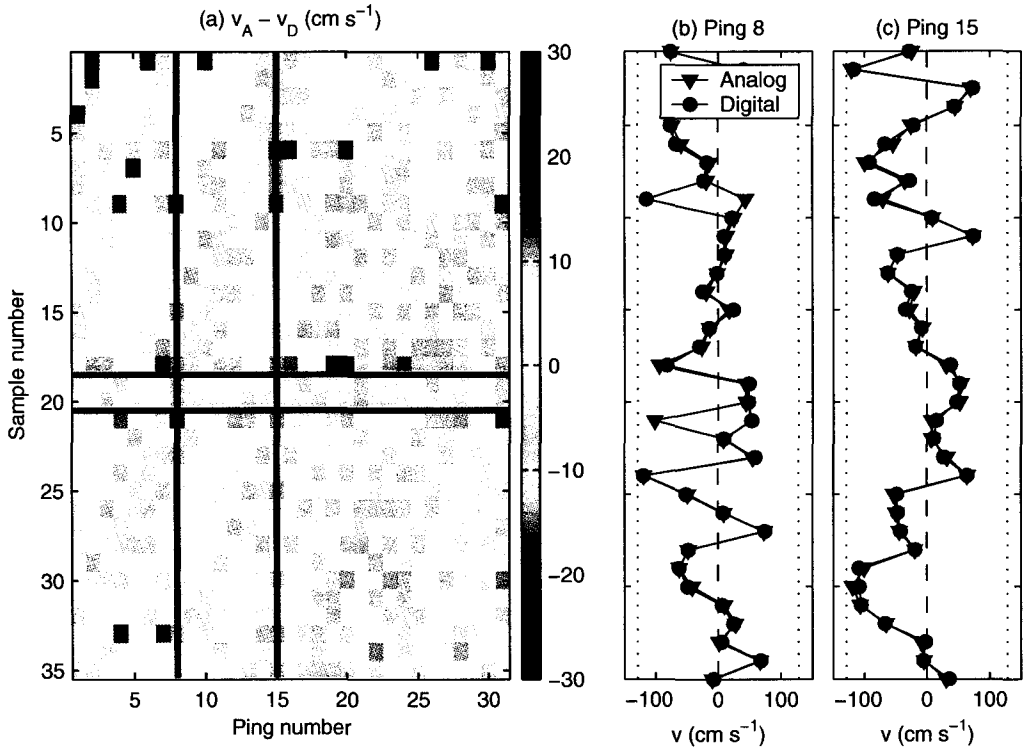

Figure 5.2: Comparison of Doppler velocities calculating using analog v_A and digital v_D demodulation techniques for the narrowband model. (a) False-colour image of the difference $v_A - v_D$ (cm s^{-1}) between analog and digital demodulator results for 31 pings. The black horizontal lines indicate the position of the fish target, and the red vertical lines indicate the locations of pings plotted in (b) and (c). The average difference for all points was $v_A - v_D = -0.45 \pm 0.53$ cm s^{-1}. (b) Profile of v_A (▼) and v_D (•) (cm s^{-1}) as a function of sample number for ping #8. (c) Profile of v_A and v_D (cm s^{-1}) as a function of sample number for ping #15. In (b) and (c), the ambiguity velocity is represented with a dotted line, and the samples corresponding to the fish are coloured in red.

5.1.4 Model parameters

A model run consisted of a number of repetitions n_{rep} of the entire modelling procedure: a single fish and a suitable number of randomly-spaced weak targets were followed through the model domain for the desired time-in-beam (Table 5.1), and the velocity of the fish target was calculated. In any series of model runs, all parameters were set to a default value and a single parameter was varied within the ranges shown in Table 5.2, with n_{rep} repetitions performed for each parameter value.

Before a thorough investigation of sonar parameters was possible it was necessary to determine the acceptable range for two fundamental model parameters: the timestep, and the number of weak targets per metre.

Short model timesteps are required to accurately reproduce acoustic pulses; however, the shorter the timestep, the longer the computation time. The model was executed using timesteps ranging from 15.625 ns to 250 ns. Error and standard deviation are plotted as a function of model timestep Δt_m in Figures 5.3a and b, respectively. The 62.5-ns timestep was chosen because both the error and the standard deviation do not change significantly as the time step decreases further, but computation time continues to increase as the timestep decreases.

The appropriate number of weak targets per unit range n_p was determined by executing the model with n_p varying from 0 to 200 m^{-1}. Error, standard deviation, and SNR are plotted as functions of n_p in Figures 5.4a, b, and c, respectively. The value of $n_p = 20$ weak targets m^{-1} was chosen as a compromise: the value of $\delta_v = -0.16$ cm s^{-1} was relatively small, the value of σ_v was within 1.3 cm s^{-1} of the theoretical value, and the model execution time was 'reasonable' to perform all the experiments of interest. Greater numbers of weak targets cause the model to slow

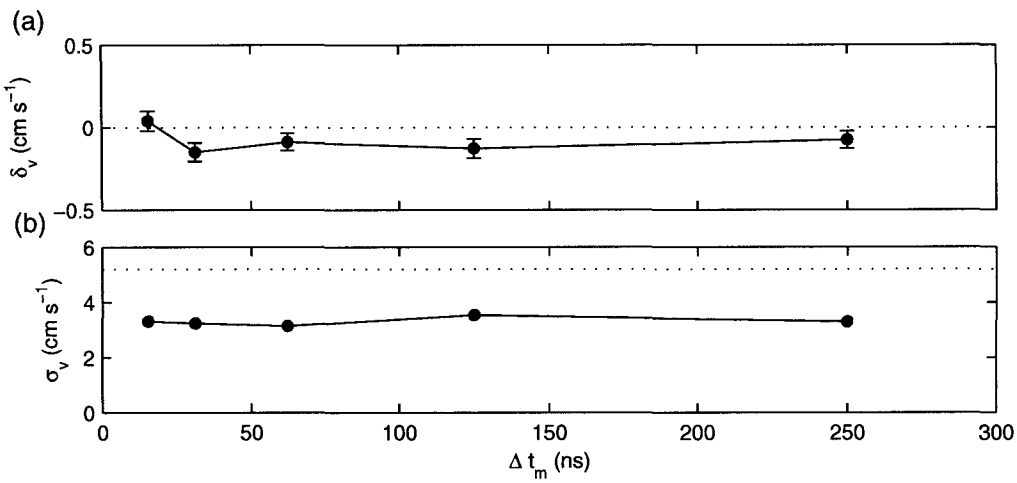

Figure 5.3: Plot of (a) δ_v (cm s^{-1}) and (b) σ_v (cm s^{-1}) as a function of model timestep Δt_m (ns). The dotted line in (b) indicates the expected value of σ_v, based on Zrnic's Equation 2.32, calculated using mean measured model values of SNR and ρ. Error bars are the standard error in (a), and smaller than the plot points in (b).

down significantly as the particles were placed in the backscattered pulse. The measured SNR of 22.0 ± 0.1 dB for $n_p \geq 20$ and $A_{rel} = -30$ dB was typical of the SNR observed in a number of the experiments and therefore a useful domain in which to explore the model. Furthermore, the backscatter $S(t)$ generated by the model with $n_p = 20$ resulted in fish targets completely surrounded by water targets, leaving no part of the modelled backscatter 'empty' of targets, as in the sample pulse in Figure 5.1. The corresponding volume particle density for $n_p = 20$ weak targets m^{-1} is 23 weak targets m^{-3} (assuming a 1-m bin centred at range $R = 20$ m).

The remaining model parameters were chosen to be representative of experimental conditions. The ping rate (3–4 Hz) was typical of the longest ping rate used in the experiments. The transmit and receive filter were forward-and-reverse Butterworth filters of order 2 (true order 4). The sound speed (1480 m s^{-1}) is typical of the

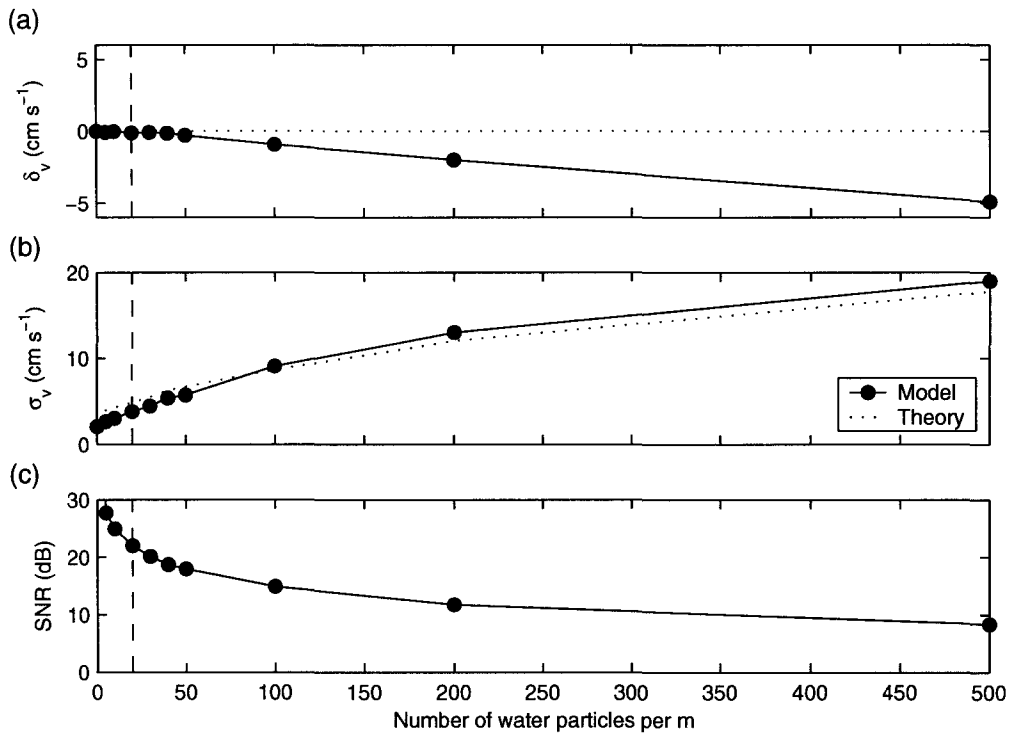

Figure 5.4: Plot of (a) δ_v (cm s^{-1}) (b) modelled (•) and theoretical (dotted line) σ_v (cm s^{-1}) and (c) SNR (dB) as a function of the number of weak targets per metre. Dashed vertical lines indicate the value implemented in the model ($n_p = 20$). Error bars are smaller than the plot points at this scale.

experimental sound speed, and the time-in-beam (10 s) and target range (20 m) are both typical of the fish in the stationary field experiment, from which the greatest proportion of live-fish data originates.

5.2 Comparison with theoretical results

Model performance was compared to theoretical results based on Zrnic's (1977) derivation of the standard deviation as a function of lag, based on a Gaussian-shaped power spectrum. The model was configured for volume backscatter in both narrowband and broadband mode, as described in Section 5.1.1, with a fixed pulse length T (228 μs) and lag τ varying from 384 to 3264 μs. The independent pulse-pair processing method was used for both the narrowband and the broadband model. Neither model is expected to reproduce results comparable to commercially available Doppler current profilers, since the processing methods are different: commercial narrowband instruments are usually incoherent and do not use the pulse-pair method, and commercial broadband instruments use long pseudo-random phase codes when implementing the pulse-pair method.

The particle density for volume backscatter was $n_p = 20$ equal-amplitude randomly-spaced scatterers per metre. The target velocities followed a Gaussian distribution with mean $\overline{v}$ and standard deviation σ_v related to the ambiguity velocity Δv by

$$\begin{aligned} \overline{v} &= 0.5\Delta v \\ \sigma_v &= 0.1\Delta v \end{aligned}$$

Increasing bandwidth while maintaining the same pulse length allowed for inves-

tigation of the effects of averaging on Doppler velocity estimates. In Doppler current profilers, backscatter and phase information are averaged along the beam direction in bins ranging from tens of centimetres to several metres in size. The limitations on the sample rate of the test instrument did not allow for averaging in the experimental data; however, the model was easily configured to allow for spatial averaging or 'binning' of the data. The binning takes place after the correlation r has been calculated from the phase data, as outlined in Section 3.2.1. Recall that the i^{th} sample of the signal s_i is given by

$$s_i = C_i'' + iS_i'' \tag{5.16}$$

where C_i'' and S_i'' are the corrected sine and cosine phase samples. The correlation r is calculated as

$$r_i = s_i \times (s_{i+L})^* \tag{5.17}$$

where L is the number of samples corresponding to the lag τ and * represents the complex conjugate. At this point, the velocity v_i for the i^{th} sample may be calculated by applying

$$v_i = \frac{\Delta v}{\pi} \arg r_i. \tag{5.18}$$

However, an alternative is to average the correlation r along M samples

$$r_j = \frac{1}{M} \sum_{i=1}^{M} r_i \tag{5.19}$$

before calculating the velocity v_j and the complex correlation coefficient ρ_j for the

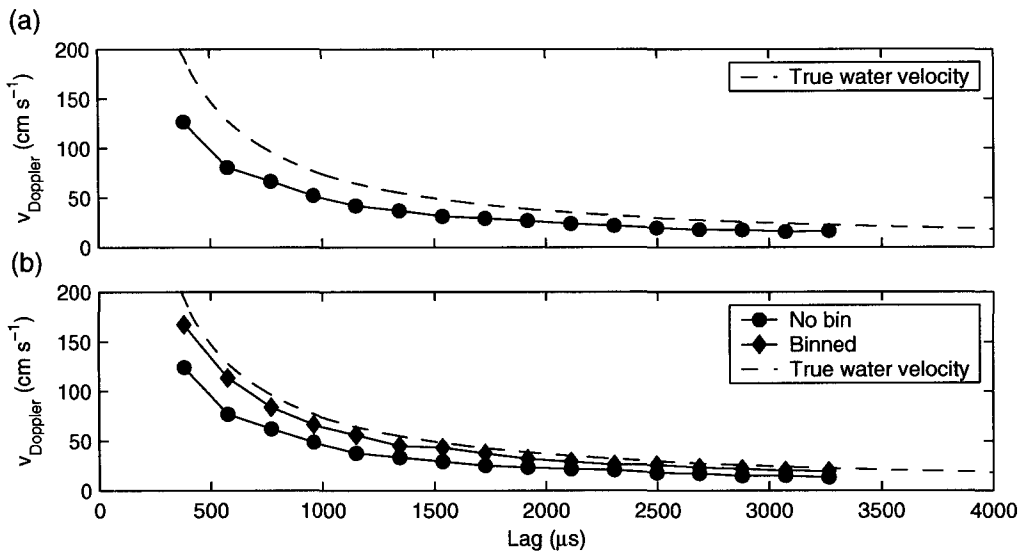

Figure 5.5: Plot of model results as a function of lag τ (μs): (a) narrowband $v_{Doppler}$ (cm s^{-1}), with true water velocity plotted as a dashed line, (b) broadband $v_{Doppler}$ (cm s^{-1}) for no-bin (•) and bin (♦) calculations, with true water velocity plotted as a dashed line. Error bars are smaller than the plot points at this scale.

j^{th} bin

$$v_j = \frac{\Delta v}{\pi} \arg r_j \tag{5.20}$$

$$\rho_j = |r_j| \tag{5.21}$$

The data are typically binned along the number of samples M corresponding to the pulse length. The number of correlation samples in each bin increased with increasing bandwidth and sample rate because the model was configured with a fixed pulse length.

Figures 5.5a and b are plots of the Doppler velocity $v_{Doppler}$ as a function of lag for the narrowband and broadband models, respectively, with the true velocity

plotted as a dashed line. The narrowband model data ($M = 2$ samples per pulse length) was not binned, while the broadband model data ($M = 56$ samples per pulse length), was treated using both no-bin and bin methods. The narrowband Doppler velocity is consistently biased toward zero by a factor of 33% across the range of lags studied. The broadband Doppler velocity computed using the binning method is on average 14% lower than the true velocity, compared to 39% for the no-bin method. The narrowband model results (no-bin) were comparable in magnitude to the no-bin broadband results (33% too low). Therefore, increasing the bandwidth alone does not reduce error unless spatial averaging is also implemented.

Examination of modelled and experimental velocity histograms confirms that the zero-bias of the Doppler velocity estimates is a direct result of the velocity aliasing inherent to the pulse-pair processing technique. Figure 5.6a and b are no-bin and bin velocity histograms for the narrowband model, Figure 5.6c and d are no-bin and bin velocity histograms for the narrowband model, and Figure 5.6e and f are no-bin and bin velocity histograms for the narrowband test instrument field data, with mean and true velocities indicated, where possible. Both narrowband and broadband modelled data suffer from a zero-bias of the mean Doppler velocity (Figures 5.6a–d). Similarly, the mean Doppler velocity calculated from the field data in Figures 5.6e and f appears to be biased relative to the location of the spectral peak (the true velocity for that dataset is unknown). The error is larger for the no-bin velocities (Figures 5.6a, c, e), than the bin velocities (Figures 5.6b, d, f). Reducing the width of the spectrum of measured velocities by increasing the pulse bandwidth and performing some averaging would reduce the error in Doppler measurements of water velocity.

Figures 5.7a and b are plots of the standard deviation as a function of lag for the

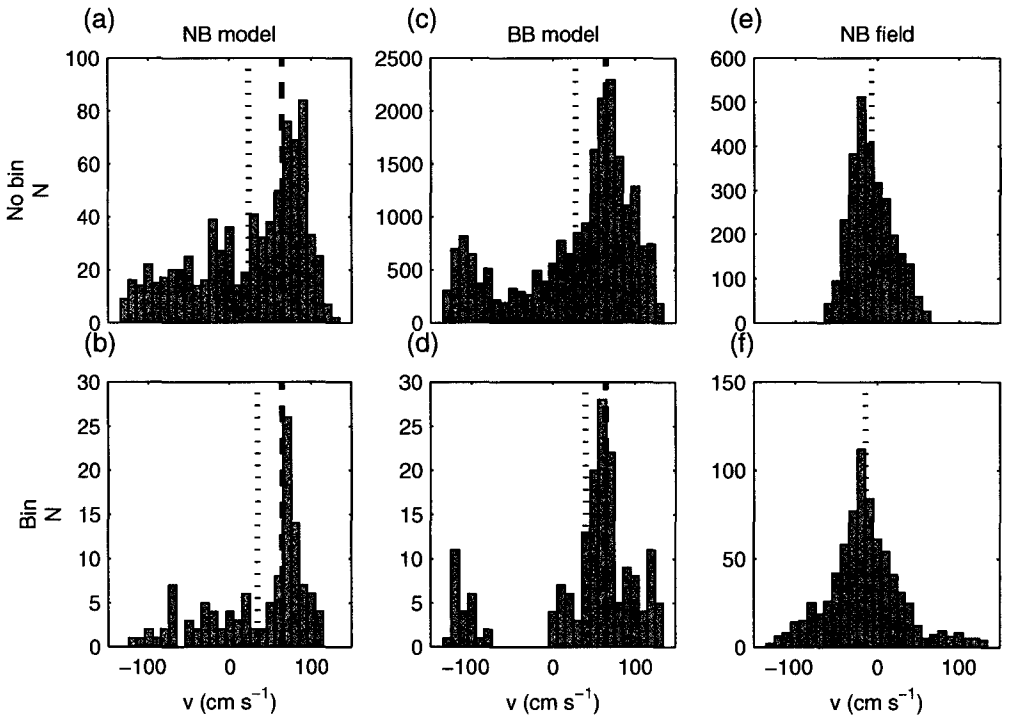

Figure 5.6: Histogram of measured Doppler velocity v (cm s^{-1}) for (a) narrowband model, no-bin, (b) narrowband model, bin, (c) broadband model, no-bin, (d) broadband model, bin, (e) field data, no-bin, and (f) field data, bin. Dotted lines indicate average Doppler velocities, and dashed lines indicate true velocities.

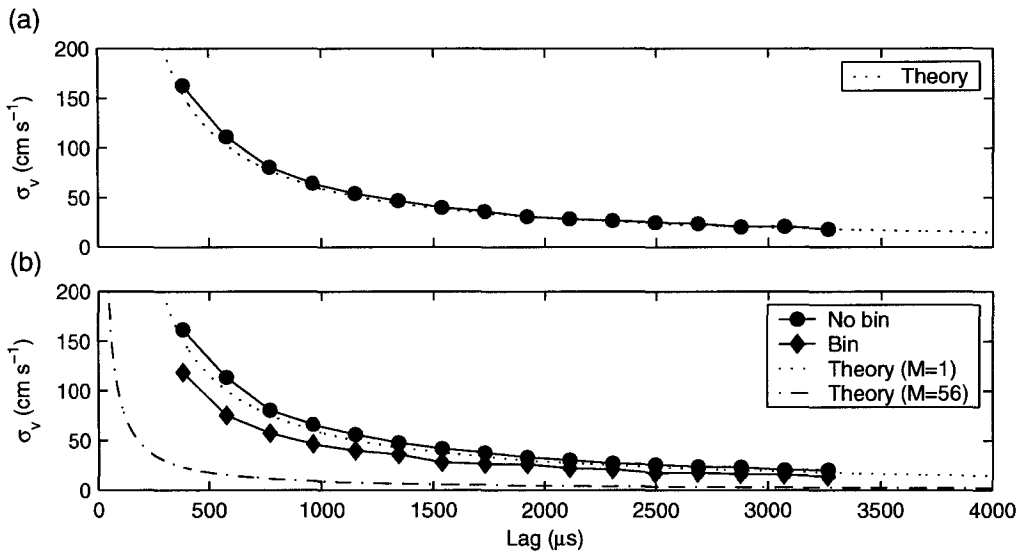

Figure 5.7: Plot of model results as a function of lag τ (μs): (a) narrowband σ_v (cm s^{-1}), with theoretical σ_v plotted as a dashed line, (b) broadband σ_v (cm s^{-1}) for no-bin (•) and bin (♦) calculations, with theoretical σ_v plotted as a dashed line for $M = 1$ and a dash-dot line for $M = 56$. Error bars are smaller than the plot points at this scale.

narrowband and broadband models, respectively. The general form of the narrowband results for σ_v as a function of τ agree relatively well with the theoretical predictions based on Equation 2.32; however, the modelled σ_v is between 0–8% greater than the predicted value. In the broadband model, the standard deviation σ_v is 11% higher than the predicted value without binning, and 26% lower than predicted with binning. Strictly speaking, however, Equation 2.32 contains a factor $1/\sqrt{M}$, where M is the number of *independent* samples averaged to obtain one velocity sample. If M is assumed to be equal to the number of samples per pulse length, the observed σ_v are a factor of 4.5 larger than predicted, implying that not all the samples are independent.

The number M of independent samples is limited by the bandwidth, and the plots in Figure 5.5d imply that $1 < M < 56$. An estimate of the effective number of

independent samples M_{eff} can by made by observing that the binned σ_v appears to be a fixed fraction of the predicted σ_v for $M = 1$. A linear fit of $\sigma_v = a_0 + a_1\sigma_{vP}$ for the binned data results in the following parameters: $a_0 = 0.8 \pm 1.3$, $a_1 = 0.67 \pm 0.02$ and $p = 0$. The intercept is equal to zero within uncertainty, so $\sigma_v \approx 0.67\sigma_{vP}$. Therefore, the effective number of independent samples M_{eff} can be calculated using the fact $\sigma_v = 1/\sqrt{M}\sigma_{vP} \approx 0.67\sigma_{vP}$, resulting in $M_{eff} = 2.23$. In other words, over the pulse length of 228 μs in the broadband water model, 2.23 independent samples were obtained, which corresponds to an effective bandwidth BW_{eff} of approximately $BW_{eff} = M_{eff}/T = 10$ kHz. Therefore, increasing the bandwidth while keeping all other transmit parameters the same does not result in larger numbers of independent samples.

5.3 Comparison with experimental results

In this section, the dependence of modelled error and standard deviation on target velocity and standard deviation, water velocity and standard deviation, lag, pulse length, pulse coding, SNR, and ρ will be explored. Model results will be compared with experimental results, where possible.

5.3.1 Target velocity

In order to determine whether error δ_v or standard deviation σ_v depend on the fish velocity, the modelled fish velocity was varied from -100 cm s^{-1} to $+100$cm s^{-1}. The water velocity was set to its default value of 0 cm s^{-1}, and all other parameters were set to their default values (Table 5.2).

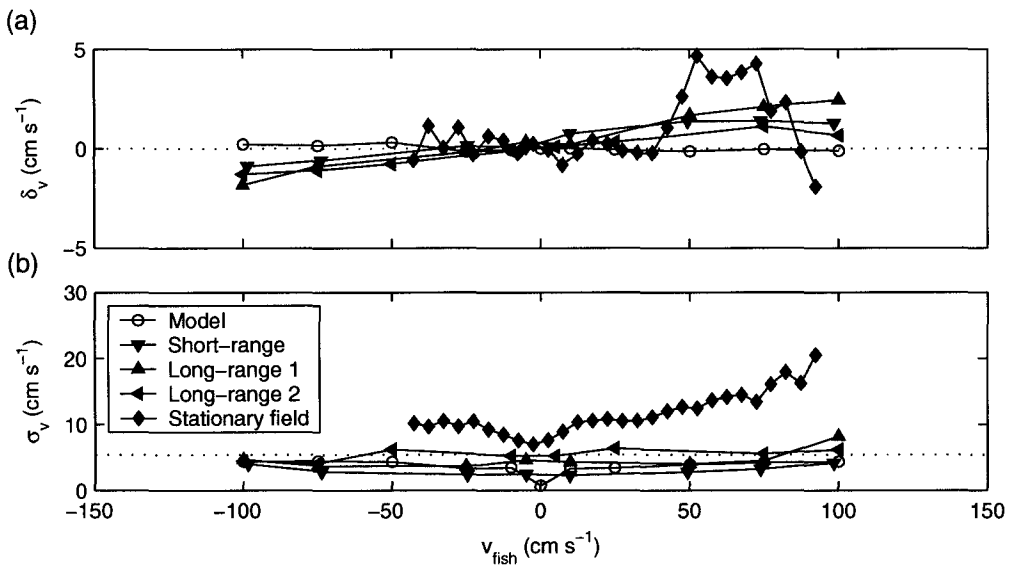

Figure 5.8: Plot of (a) δ_v (cm s^{-1}) and (b) σ_v (cm s^{-1}) as a function of fish velocity (cm s^{-1}) for the narrowband model (○), the short-range towtank experiment (▼), the long-range towtank experiments 1 (▲) and 2 (◀), and the stationary field experiment (♦). The model was executed with default parameters (Table 5.2), and the experimental results were acquired with the same lag (1152 μs) and pulse length (228 μs, uncoded) as the model. Theoretical σ_v in (b) is indicated by a dotted line. Error bars are smaller than the plot points at this scale.

The error and standard deviation are plotted as a function of target velocity in Figures 5.8a and b, respectively, for both modelled and experimental data acquired with the same lag (1152 μs) and pulse length (228 μs, uncoded). Parameters from linear fits of model results in Table A.27 revealed no dependence of either δ_v or σ_v on target velocity ($p > \alpha$). Average values of modelled δ_v for all target velocities were less than 0.5 cm s^{-1}, and average values of modelled σ_v were less than 5 cm s^{-1}. The modelled standard deviation σ_v is somewhat lower than the theoretical standard deviation of 5.4 cm s^{-1} as predicted by Zrnic (Equation 2.32), but in good agreement with towtank observations.

Field observations of σ_v were higher than the towtank or model results, which is not surprising given that the towtank and model both involve targets with a single velocity component, whereas the live fish in the field might be expected to show some variation in velocity from ping to ping. In order to reproduce the effect of a time-varying fish velocity, the modelled fish velocity for each ping was randomly chosen to lie within a range $\pm\Delta_v$ centred about 50 cm s^{-1}, where $0 \leq \Delta_v \leq 20$ cm s^{-1}. For each modelled fish, the mean true fish velocity v_T and its standard deviation σ_{vT} were computed. The error and standard deviation are plotted as functions of the target standard deviation σ_{vT} in Figures 5.9a and b, respectively.

Parameters of a linear fit to the error as a function of target velocity standard deviation σ_{vT} in Table A.28 reveal a dependence of δ_v on σ_{vT} ($p < \alpha$). The small negative slope of -0.03 ± 0.02 cm s^{-1}/cm s^{-1} implies that the Doppler velocity becomes slightly biased toward zero as the variance in the target velocity increases. The mean value and standard error of δ_v are $\overline{\delta_v} \pm \sigma_{\overline{\delta_v}} = -0.16 \pm 0.03$ cm s^{-1}, which is not equal to zero within uncertainty, again implying that the Doppler speed is slightly lower

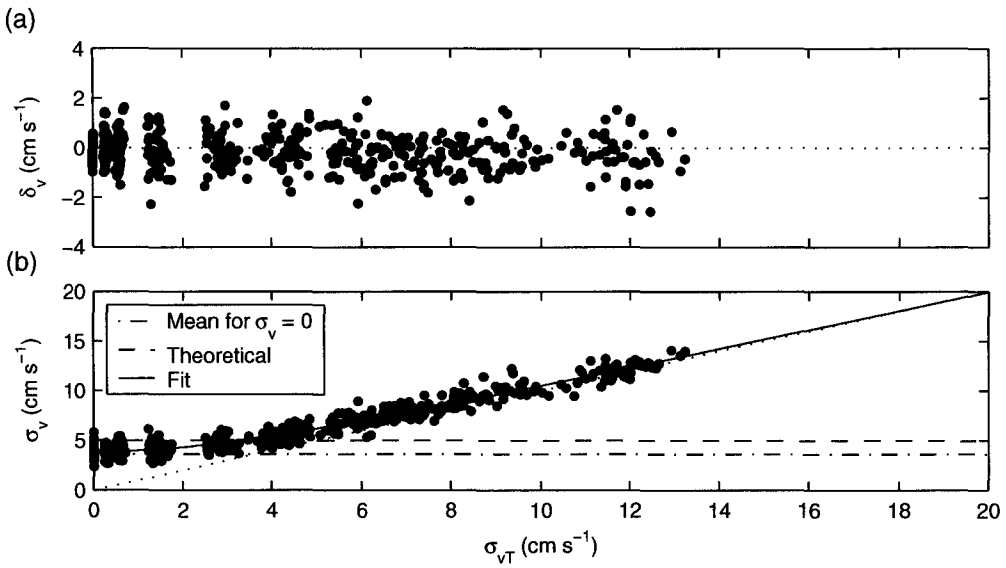

Figure 5.9: Plot of (a) δ_v ($\mathrm{cm\,s^{-1}}$) and (b) σ_v ($\mathrm{cm\,s^{-1}}$) as a function of target velocity standard deviation ($\mathrm{cm\,s^{-1}}$) for the narrowband model. Each point represents a single modelled target.

than the true speed.

The standard deviation increases as σ_{vT} increases (Figure 5.9b). The mean value for σ_v in the single-velocity model was 3.6 $\mathrm{cm\,s^{-1}}$, and at this value the plot of σ_v as a function of σ_{vT} is divided into two regions. For $\sigma_{vT} < 3.6$ $\mathrm{cm\,s^{-1}}$, the standard deviation σ_v remains constant at 4.04 ± 0.04 $\mathrm{cm\,s^{-1}}$, while for $\sigma_{vT} > 3.6$ $\mathrm{cm\,s^{-1}}$, the standard deviation σ_v follows the shape of the 1:1 line, but is 1.9 $\mathrm{cm\,s^{-1}}$ greater than σ_{vT} on average. In other words, the plots appear to be the sum of a constant term c and a linear term $mx + b$, added in quadrature to produce the observed values of σ_v:

$$\sigma_v^2 = (mx + b)^2 + c^2 \tag{5.22}$$

Equation 5.22 can be re-written as a parabola

$$y = a_0 + a_1 x + a_2 x^2, \tag{5.23}$$

with $y = \sigma_v^2$ and a_0, a_1, and a_2 related to m, b, and c by

$$m = \sqrt{a_2}\,, \quad b = \frac{a_1}{2\sqrt{a_2}}\,, \quad c = \sqrt{a_0 - \frac{a_1^2}{4a_2}}\,. \tag{5.24}$$

The square of the Doppler standard deviations were fit to a parabolic model (Equation 5.23), resulting in the parameters a_0, a_1, and a_2 given in Table A.28. Application of the formulae in Equation 5.24 to the fit parameters results in values for m, b, and c:

$$\begin{aligned} m &= 0.980 \pm 0.002 \text{ cm s}^{-1}/\text{cms}^{-1} \\ b &= -0.02 \pm 0.02 \text{ cm s}^{-1} \\ c &= 3.84 \pm 0.08 \text{ cm s}^{-1} \end{aligned} \tag{5.25}$$

Two details are revealed by the parameters in Equation 5.25. First, the constant value of $c = 3.84 \pm 0.08$ cm s^{-1} is close to both the 'rough' value calculated from the data of 4.04 ± 0.04 cm s^{-1}, and the value of 3.6 cm s^{-1} observed with zero target standard deviation. Second, the standard deviation σ_v increases linearly with target standard deviation beyond a threshold value, with a ratio $m = 0.980 \pm 0.002$, which is nearly a ratio of 1:1. In other words, a greater spread of actual target velocities will result in a greater spread of Doppler velocities over and above the standard deviation of Doppler velocities already present because of the pulse-pair method of velocity estimation. A swimming fish presents a range of target velocities rather than

a single velocity, resulting in higher values of standard deviation for a swimming fish compared to styrofoam balls.

5.3.2 Water velocity

The effects of water velocity on Doppler estimates of fish velocity were difficult to quantify in the experiments. In the towtank experiments, the water velocity was equal to the target velocity, and there was no way of changing the relative velocity between the two. In the field experiments, the water velocity changed with time because the location of the experiments was subject to tidal fluctuations. However, attempts to measure the water velocity resulted in very noisy velocity estimates, probably caused by the proximity of the sonar to the boundary layer at the river's edge, and the water velocity estimates were abandoned. Therefore, the best way to systematically explore the effects of water velocity on error and standard deviation was to use the computer model, which was configured with a fixed fish velocity of 50 cm s^{-1} and water velocity which varied between −100 cm s^{-1} and +100 cm s^{-1}.

Figures 5.10a and b are plots of the error and standard deviation as functions of water velocity v_{water}. The absolute value of the error $|\delta_v|$ was less than 0.4 cm s^{-1} in all cases, and the linear fit parameters in Table A.29 confirmed that δ_v did not depend on water velocity ($p > \alpha$). The standard deviation is a minimum (2.46 ± 0.05 cm s^{-1}) when the water velocity and fish velocity are equal at 50 cm s^{-1}, and rises symmetrically as the difference between water and fish velocity increases. The model data from Figure 5.10b were regrouped and σ_v is plotted as a function of the absolute difference between the water and fish velocity $|v_{fish} - v_{water}|$ in Figure 5.10c. The value of σ_v rises to 4.8 cm s^{-1} when the difference between velocities is greater than 100 cm s^{-1}.

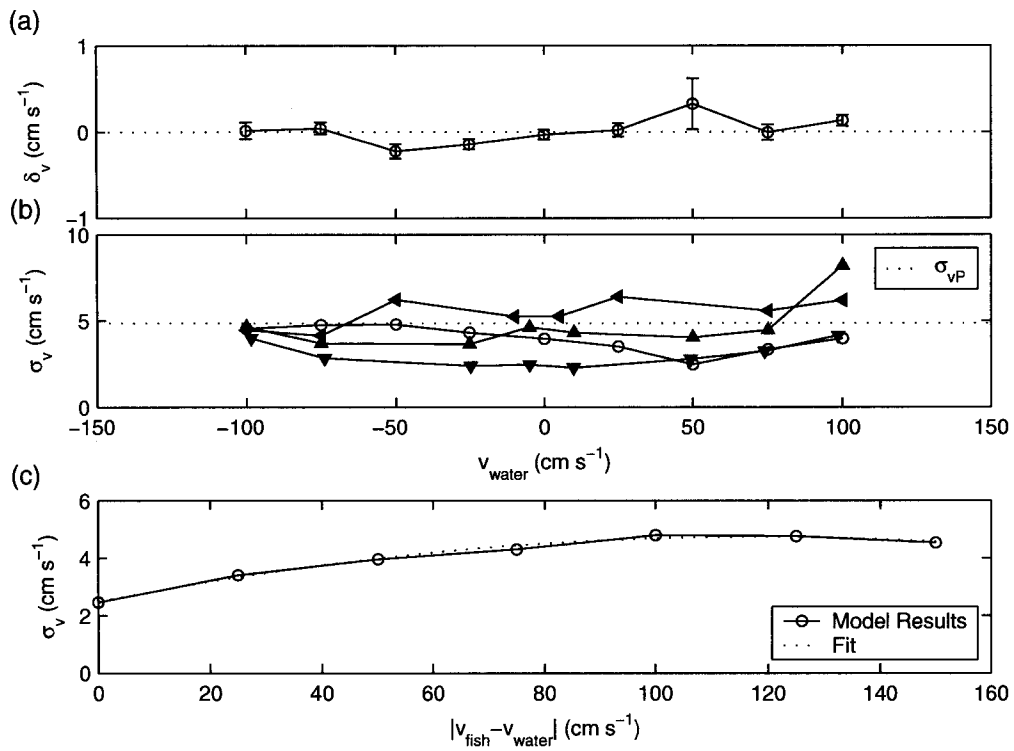

Figure 5.10: Plot of (a) δ_v (cm s^{-1}) and (b) σ_v (cm s^{-1}) as a function of water velocity (cm s^{-1}) for the narrowband model (○), short-range experiment (▼), long-range experiment (OERC B)(▲), long-range experiment (IOT)(◀), and theoretical prediction (dotted line). (c) Plot of σ_v (cm s^{-1}) as a function of $|v_{fish} - v_{water}|$ (cm s^{-1}) for the narrowband model with the quadratic fit based on parameters in Table A.29 plotted as a dotted line. For all three plots, the fish velocity was 50 cm s^{-1} for the modelled data. Error bars are smaller than the plot points at the scales of (b) and (c).

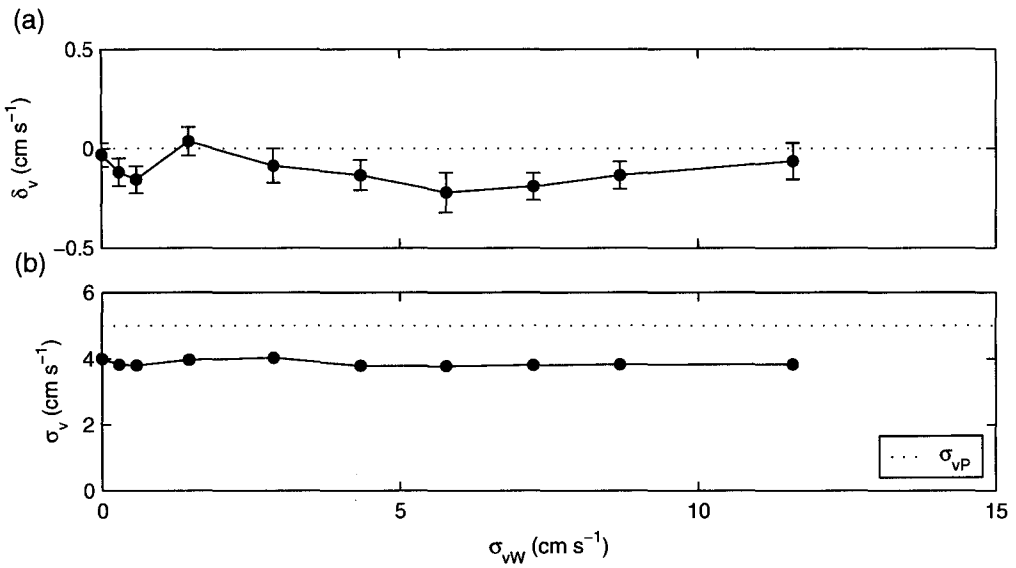

Figure 5.11: Plot of (a) δ_v (cm s^{-1}) and (b) σ_v (cm s^{-1}) as a function of water velocity standard deviation σ_{vW} (cm s^{-1}) for the narrowband model. Centre water velocity is 0 cm s^{-1}. Error bars are smaller than the plot points at the scale of (b).

A second-order polynomial fit describes the data well within the ranges studied, and the fit parameters in Table A.29 confirm the dependence of σ_v on $|v_{fish} - v_{water}|$ ($p < \alpha$).

Turbulence was simulated by allowing the water velocity to vary within a range $\pm\Delta_v$ of the mean water velocity value of 0 cm s^{-1}, with values of Δ_v from 0–20 cm s^{-1}. Figures 5.11a and b are plots of the error and standard deviation as functions of the standard deviation in water velocity σ_{vW}. Linear fit parameters for δ_v and σ_v as functions of σ_{vW} in Table A.29 revealed that neither error nor standard deviation depend on the standard deviation in water velocity σ_{vW} ($p > \alpha$). It is therefore expected that, within the range limitations introduced by turbulence, Doppler measurements of fish velocity in more turbulent waters should not be any different than those in

still waters.

5.3.3 Lag

Standard deviation is inversely proportional to lag (Equation 2.32), and experimental data have demonstrated that the general shape of the standard deviation as a function of lag is correct. In order to further explore the effects of lag on both error and standard deviation, the model was configured with lags ranging from 384–3264 μs.

Two separate model configurations were employed. In the first configuration, the target velocity was equal to 50 cm s^{-1}, and velocity aliasing was observed for lags greater than 2688 μs. In the second configuration, the target velocity was set to equal one-half the ambiguity velocity to avoid the velocity aliasing effects. The error and standard deviation are plotted as functions of lag in Figures 5.12a and b, respectively, for $v_{target} = 50$ cm s^{-1}, and in Figures 5.12c and d, respectively, for $v_{target} = \frac{1}{2}\Delta v$.

The error is equal to zero within uncertainty (-0.05 ± 0.10 cm s^{-1}) when the target velocity does not exceed the ambiguity velocity Δv (Figure 5.12a). For $v_{fish} < \Delta v$, parameters of linear fits in Table A.30 reveal no dependence of δ_v on lag ($p > \alpha$). Once the fish velocity exceeds the ambiguity velocity, δ_v grows rapidly. The fact that there is no velocity aliasing for $\tau = 2688$ μs ($\Delta v = 55$ cm s^{-1}) while there is aliasing for $\tau = 2880$ μs ($\Delta v = 51$ cm s^{-1}) implies that the modelled velocity spectrum is quite narrow, with a width between 1–4 cm s^{-1}.

When the fish velocity is chosen to prevent velocity aliasing ($v_{target} = \frac{1}{2}\Delta v$), the absolute value of the error $|\delta_v|$ is less than 1 cm s^{-1} at all lags, and the average value for the error is $\overline{\delta_v} = -0.08 \pm 0.05$ cm s^{-1}, which is not equal to zero within uncertainty but negative, indicating that the Doppler technique slightly underestimates the fish

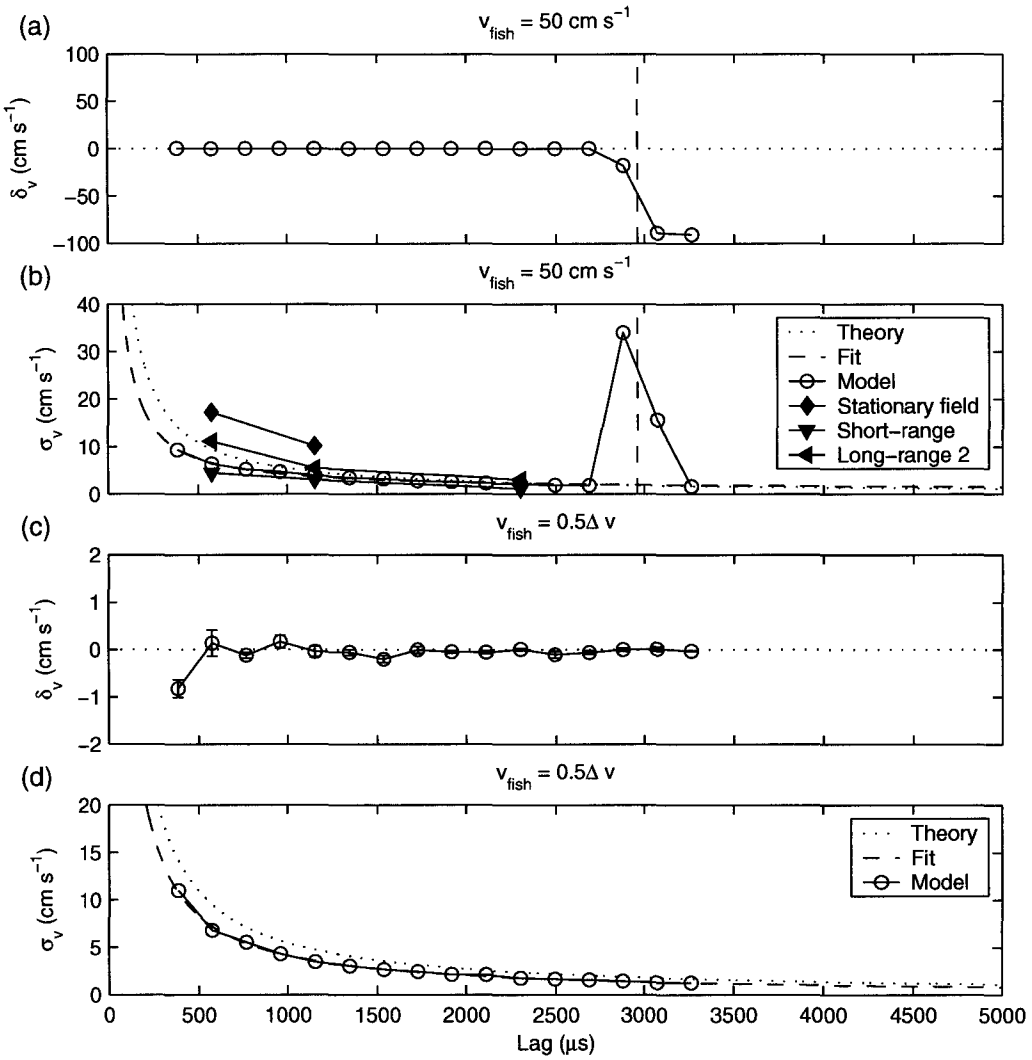

Figure 5.12: (a) δ_v (cm s^{-1}) and (b) σ_v (cm s^{-1}) as a function of lag τ (μs) for the narrowband model with $v_{fish} = 50$ cm s^{-1} and experiments (see legend in (b)). The vertical line indicates the lag for which $\Delta v = v_{fish} = 50$ cm s^{-1}, the dotted line in (b) is the predicted standard deviation σ_{vP} calculated using Equation 2.32, and the dashed line is the fit of $\sigma_v = a_0 + a_1\sigma_{vP}$. (c) δ_v (cm s^{-1}) and (d) σ_v (cm s^{-1}) as a function of lag τ (μs) for the narrowband model with $v_{fish} = 0.5\Delta v$. The dotted line in (d) is the predicted standard deviation σ_{vP} calculated using Equation 2.32, and the dashed line is the fit of $\sigma_v = a_0 + a_1\sigma_{vP}$. Error bars are smaller than the plot points at the scale of (a), (b), and (d).

velocity (Figure 5.12c). The results of a linear fit in Table A.30 suggest that δ_v does not depend on lag ($p > \alpha$).

In Figure 5.12b, the shape of the dependence of the modelled standard deviation on lag follows that described by Zrnic (Equation 2.32), but the values for σ_v are lower than predicted. Once velocity aliasing occurs, the standard deviation increases drastically to 35 cm s^{-1}. When the fish velocity is chosen to prevent velocity aliasing ($v_{target} = \frac{1}{2}\Delta v$), the modelled standard deviation again appears to be a constant fraction of the theoretical standard deviation σ_{vP} (Figure 5.12d). A linear fit of σ_v as a function of the theoretical standard deviation σ_{vP} with parameters in Table A.30 shows that for $v_{target} = 50$ cm s^{-1}, $\sigma_v \approx 0.61\sigma_{vP}$ ($\sigma_{vP} \approx 1.6\sigma_v$) and for $v_{target} = \frac{1}{2}\Delta v$, $\sigma_v \approx 0.76\sigma_{vP}$ ($\sigma_{vP} \approx 1.3\sigma_v$).

The towtank experiments featuring varying lags, which allow for comparison with the model, are in good agreement with the model results (Figure 5.12b). The stationary field experiment resulted in higher values for σ_v than the model, consistent with the hypotheses that the fish swimming movement and the difference between fish and water velocity are contributing to the higher observed value of σ_v for the live-fish experiments.

5.3.4 Pulse length and coding

In order to investigate the effects of pulse length and pulse coding, the model was configured with pulse lengths varying from 32 μs to 640 μs, and both coded and uncoded pulses were used where a Barker code exists for a given pulse length (Table 2.2). Figures 5.13a and b are plots of error and standard deviation as functions of pulse length for both coded and uncoded pulses, respectively.

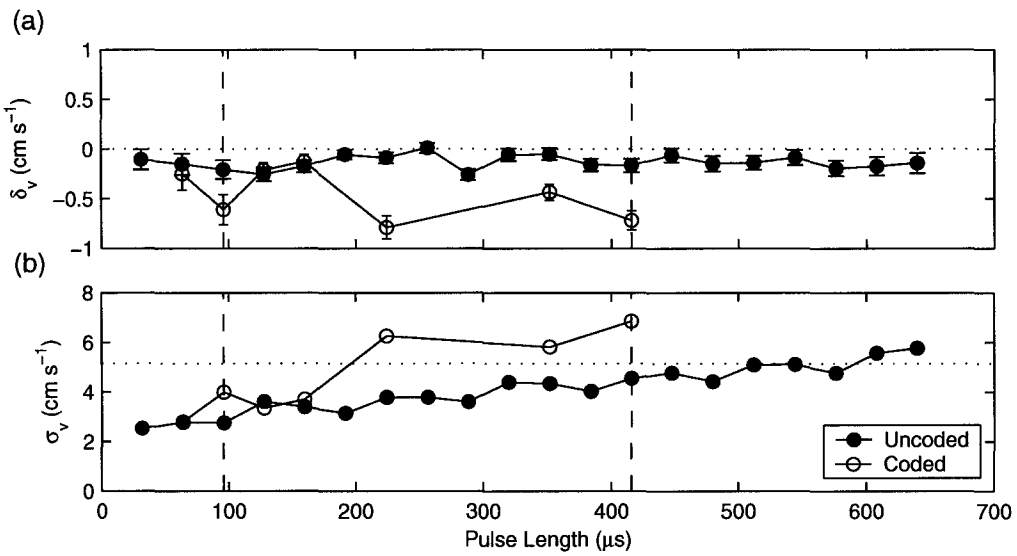

Figure 5.13: Plot of (a) δ_v (cm s^{-1}) and (b) σ_v (cm s^{-1}) as a function of pulse length (μs) for the narrowband model, for uncoded (•) and Barker-coded (○) pulses. Error bars are smaller than the plot points at the scale in (b). Dashed lines indicate the limits of pulse lengths used in the experiments, and the dotted line in (b) indicates the value for σ_v calculated using Equation 2.32.

The the error δ_v was small and on average, negative: $|\delta_v|$ was less than 0.3 cm s^{-1} for the uncoded pulses, and less than 0.8 cm s^{-1} for the coded pulses (Figure 5.13a). The average error is $\overline{\delta_v} = -0.13 \pm 0.02$ cm s^{-1} for uncoded pulses and $\overline{\delta_v} = -0.45 \pm 0.04$ cm s^{-1} for coded pulses, which is relatively small (less than 1% of the fish swimming velocity) but not equal to zero within uncertainty. The parameters for linear fits of δ_v reveal no dependence of δ_v on pulse length ($p > \alpha$).

The standard deviation increases from 2.5 cm s^{-1} to 5.5 cm s^{-1} over the range of uncoded pulse lengths studied, and to 6.7 cm s^{-1} for the coded pulses, with coded pulses giving a 1–2 cm s^{-1} larger σ_v for some pulse lengths (Figure 5.13b). In both the uncoded and coded cases, the parameters of linear fits to σ_v as a function of pulse length in Table A.31 confirm the dependence ($p < \alpha$). In contrast, the experimental results in Tables A.23 and A.24 showed no significant difference between uncoded and coded pulses, and no change in σ_v with pulse length. It is possible that the effect of pulse coding was overwhelmed by other effects, such as fish motion and tank reverberation, in the experimental datasets.

5.3.5 SNR and ρ

Effects of changing SNR were modelled by varying the water particle strength A_{rel} relative to the fish target, and examining the error and standard deviation as a function of the measured SNR. The SNR measured from the model output is plotted as a function of the relative strength of the weak targets A_{rel} in Figure 5.14. Varying A_{rel} over the range –80 to 0 dB corresponded to measured SNR ranging from 2–72 dB.

The error δ_v, standard deviation σ_v, and correlation coefficient ρ are plotted as functions of measured SNR in Figures 5.15a, b, and c, respectively, for the model,

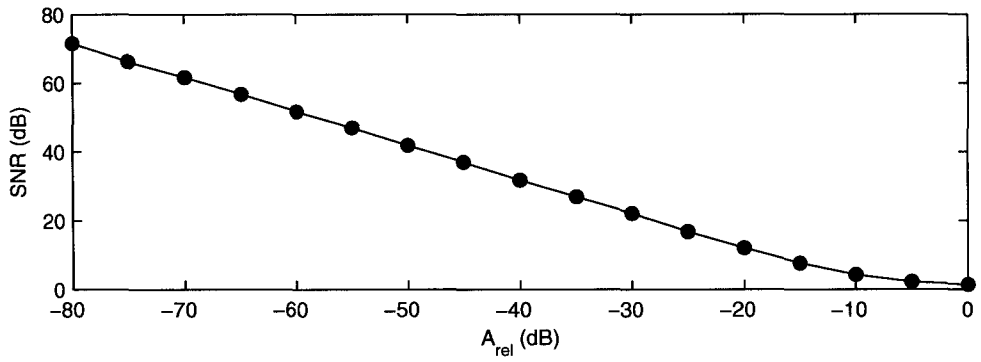

Figure 5.14: Plot of measured SNR (dB) as a function of relative target strength A_{rel} (dB) for the narrowband model. Error bars are smaller than the plot points at this scale.

experiments, and theory. Model output can also be examined as a function of ρ instead of SNR, as in Figures 5.15d and e, which are plots of error and standard deviation as functions of ρ, respectively.

The error is large and negative (-40 cm s^{-1}) when SNR = 1.5 dB and approaches zero rapidly as SNR increases (Figure 5.15a). For SNR $>$ 15 dB, the absolute value of the error $|\delta_v|$ is less than 1 cm s^{-1}. The fact that the Doppler velocity measurement is strongly biased toward the water velocity (0 cm s^{-1}) at low SNR ($v_{Doppler} - v_{fish} \approx -50\,\text{cm s}^{-1} = v_{water} - v_{fish}$) suggests that in the low-SNR region, the backscattered signal from the solid target is overwhelmed by backscatter from the water, and it is the water velocity that is measured instead.

The modelled standard deviation as a function of SNR is in agreement with the predicted standard deviation σ_{vP} (Figure 5.15b). Experimental results for σ_v as a function of SNR follow the model results very closely for SNR $>$ 15 dB. For SNR $<$ 15 dB, the experiments resulted in smaller σ_v than the model. It is possible that the model does not accurately reproduce the noise effects experienced by the

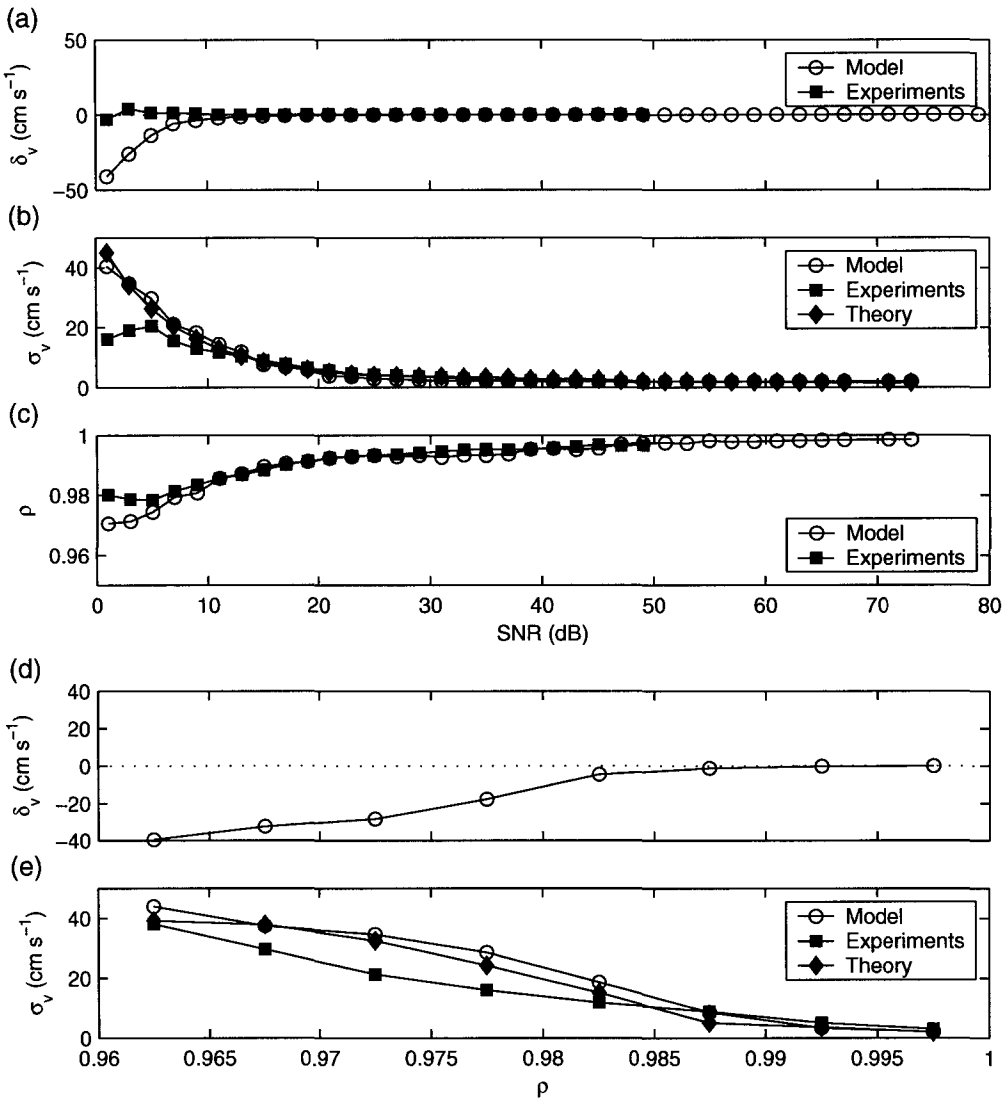

Figure 5.15: Plot of (a) δ_v (cm s^{-1}), (b) σ_v (cm s^{-1}), and (c) ρ as a function of SNR (dB) for the narrowband model; plots of (d) δ_v (cm s^{-1}), (e) σ_v (cm s^{-1}) as a function of ρ for the narrowband model. In (b) and (e), theoretical results were calculated using Equation 2.32 with measured SNR and ρ (dotted line). Error bars are smaller than the plot points at this scale.

sonar when SNR $<$ 15 dB; in particular, the model did not account for electronic noise, which could be significant relative to the signal levels at low SNR.

The model and experimental mean correlation coefficients calculated as a function of SNR also agree for SNR $>$ 15 dB while diverging for SNR $<$ 15 dB (Figure 5.15c). In the region SNR $<$ 15 dB, the model ρ is slightly (0.003–0.006) smaller than the experimental ρ. Since σ_v is very sensitive to small changes in ρ when $\rho \approx 1$, the difference in ρ could be another source of the discrepancy in σ_v at low SNR.

The data can also be examined as a function of ρ instead of SNR. The error is very large and negative when $\rho < 0.9875$ (Figure 5.15d), but its absolute value is less than 2 cm s^{-1} when $\rho \geq 0.9875$, which is necessarily consistent with the plots in Figure 5.15a and c: $\rho = 0.9875$ at about 15 dB, which is where δ_v as a function of SNR drops below ± 1 cm s^{-1}.

The modelled standard deviation as a function of ρ is in good agreement with the theoretical standard deviation σ_{vP} (Figure 5.15e). However, the experimental results have $\sigma_v < \sigma_{vP}$ when $\rho < 0.9875$, consistent with the results as a function of SNR.

Many of the results so far have demonstrated that the test instrument consistently performs better than expected in low-SNR (low-ρ) measurement environments. Therefore, the model does not accurately represent the low-SNR measurement environment, although agreement with experimental results is good for SNR $>$ 15 dB.

5.4 Model extension

Two primary areas were of interest for the extension of experimental results using the model. The first area of interest was the exploration of the effect of multiple

strong targets in the beam, since anomalously large error and standard deviation had been observed when backscatter from multiple targets overlapped during the target-array experiment. The second area of interest was the investigation of the effects of bandwidth and averaging schemes on fish velocity estimates.

5.4.1 Multiple strong targets

The effect of two strong scatterers simultaneously occupying the beam was examined by introducing a second target with the same amplitude and velocity as the first target, at a location Δ_R relative to the first target (Δ_R ranging from –1.5 m to +1.5 m). The lag, pulse length, and coding used were chosen to correspond with those for which the largest deviations had been observed in the target-array experiment: lag $\tau = 768$ μs and an 11-element coded pulse of length $T = 352$ μs.

The error and standard deviation as a function of the distance between strong targets are plotted in Figures 5.16a and b, respectively, with shaded regions indicating where one or both pulses from each target overlap in the backscatter. The absolute value of the error $|\delta_v|$ is less than 0.5 cm s^{-1} when the targets are not overlapping or if both pulses from both targets are overlapping, but the measured Doppler velocity exhibits large error (up to -25 cm s^{-1}) when one pulse from each target is overlapping (Figure 5.16a). The large error is caused by corruption of the phase information used to calculate velocity with the pulse-pair technique, and it is also the reason δ_v remains low when *both* pulses from both targets overlap: although the second target corrupts the phase of backscatter from the first target, it corrupts each pulse of the pair in the same way, so the relative phase difference upon which the Doppler velocity calculation is based is not affected. When both pulses overlap, the sonar essentially sees a single

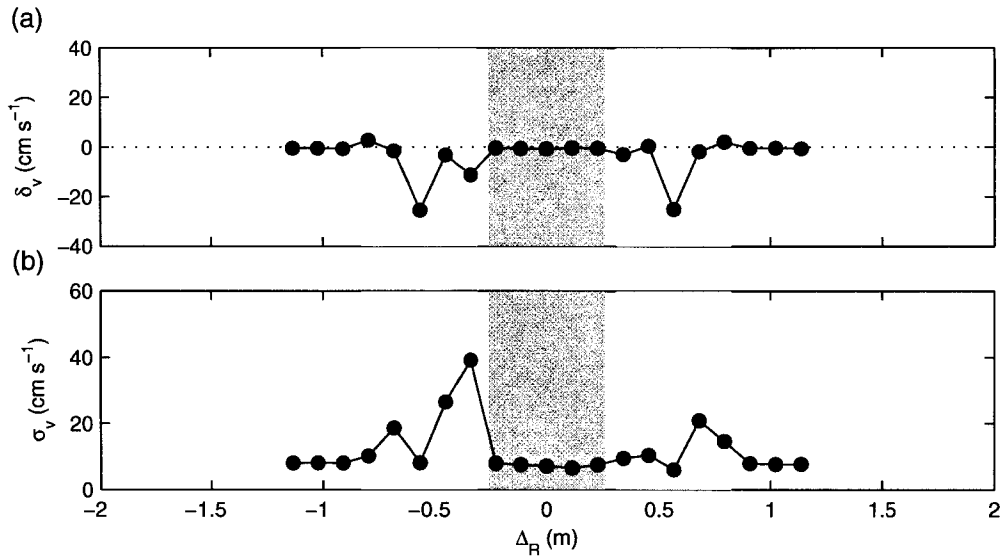

Figure 5.16: Plot of (a) δ_v (cm s^{-1}) and (b) σ_v (cm s^{-1}) as a function of distance between strong targets Δ_R for the narrowband model. The lighter shaded regions indicates the area of overlap of one pulse from each target, and the darker shaded region indicates the area in which both pulses from each target overlap. Error bars are smaller than the plot points at this scale.

target, with perhaps some internal structure. The deviations observed in the model are consistent with experimental results in pattern, but larger in magnitude. In the target-array experiment with the same pulse length and lag, δ_v was as high as 11 cm s^{-1} when targets were overlapping, compared to less than 2 cm s^{-1} with no overlap (Figure 4.3a).

The standard deviation determined from the model is similarly well-behaved when targets are not overlapping ($\sigma_v < 9$ cm s^{-1}), and then increases to values as high as 40 cm s^{-1} when the backscatter from the one pulse of each target overlaps (Figure 5.16b). The model results are comparable with experimental results, in which overlapping targets resulted in σ_v as high as 10–34 cm s^{-1}, while non-overlapping targets

had $\sigma_v < 7$ cm s^{-1} (Figure 4.3c).

5.4.2 Bandwidth

The effect of bandwidth was investigated by configuring the model with sample rates varying from 8–96 μs, and transmit and receive bandwidths equal to the inverse of the sample interval (recall that 96 μs is the sample rate of the test instrument being modelled). The default pulse length ($T = 228$ μs) and lag ($\tau = 1152$ μs) were used with both uncoded and coded pulses (the code element length is 32 μs). It would have been necessary to decrease the pulse length as the bandwidth increased in order to take full advantage of the increasing bandwidth; however, it would have been impossible to identify any observed effect as being solely caused by either the changing pulse length or changing bandwidth. Furthermore, when observing swimming fish such as pink salmon, sockeye salmon, or Atlantic cod, as in the experiments, pulse lengths substantially shorter than 228 μs (17 cm) are unnecessary, as the fish size is comparable to or longer than the pulse length. Therefore, the pulse length was maintained at a constant value while the bandwidth was changed.

The effect of binning the correlation r calculated using Equation 3.9 was investigated for the fish target as it was with the water (Section 5.2). Doppler velocities were calculated for the fish with both 'no-bin' and 'bin' methods. Figures 5.17a and b are plots of the number of samples and the SNR as a function of bandwidth, respectively. The number of samples available for binning in a 228-μs pulse varies from 12 to 144 over the range of modelled bandwidths. The SNR observed using coded pulses is 1.5 dB higher than that measured using coded pulses at a bandwidth of 10 kHz, and the difference decreases with increasing bandwidth (Figure 5.17b).

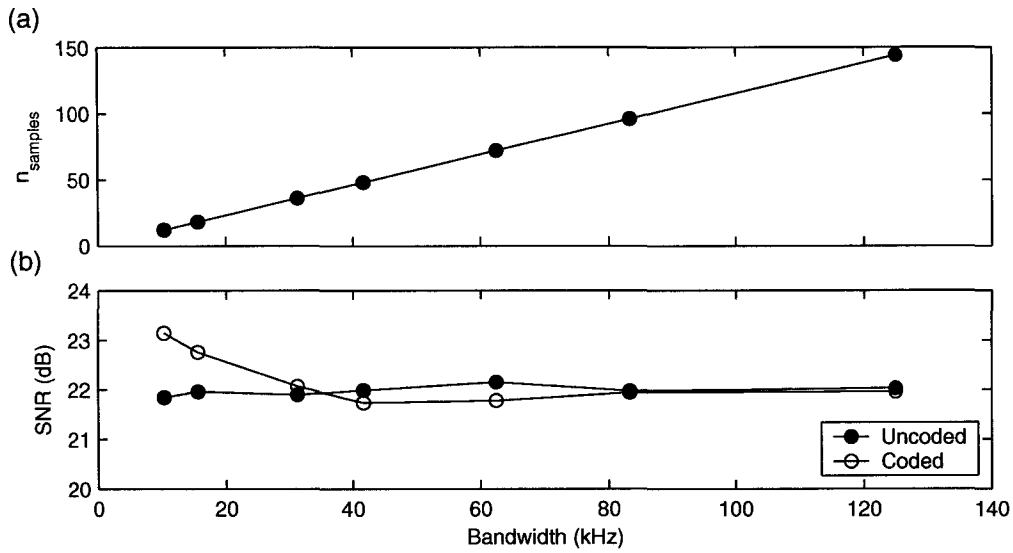

Figure 5.17: Plot of (a) $n_{samples}$ for the bin method, (b) SNR (dB), as a function of bandwidth for the computer model, for uncoded (•) and coded (o) 228-μs pulses. Error bars are smaller than the plot points at this scale.

Figures 5.18a and b are plots of the error as a function of bandwidth for uncoded and coded pulses, respectively. Figures 5.18c and d are plots of the standard deviation as a function of bandwidth for uncoded and coded pulses. Figures 5.18e and f are plots of the correlation coefficient of the fish as a function of bandwidth for uncoded and coded pulses. Figures 5.18g and h are plots of the correlation coefficient of the water as a function of bandwidth for uncoded and coded pulses. Figures 5.18i and j are plots of the difference $\rho_{fish} - \rho_{water}$ as a function of bandwidth for uncoded and coded pulses.

There was no dependence of error on bandwidth ($p = 0.15 - 0.71$) for any combination of uncoded/coded and bin/no-bin data in Figures 5.18a and b. For uncoded pulses, the no-bin and bin methods produced errors which were in agreement within

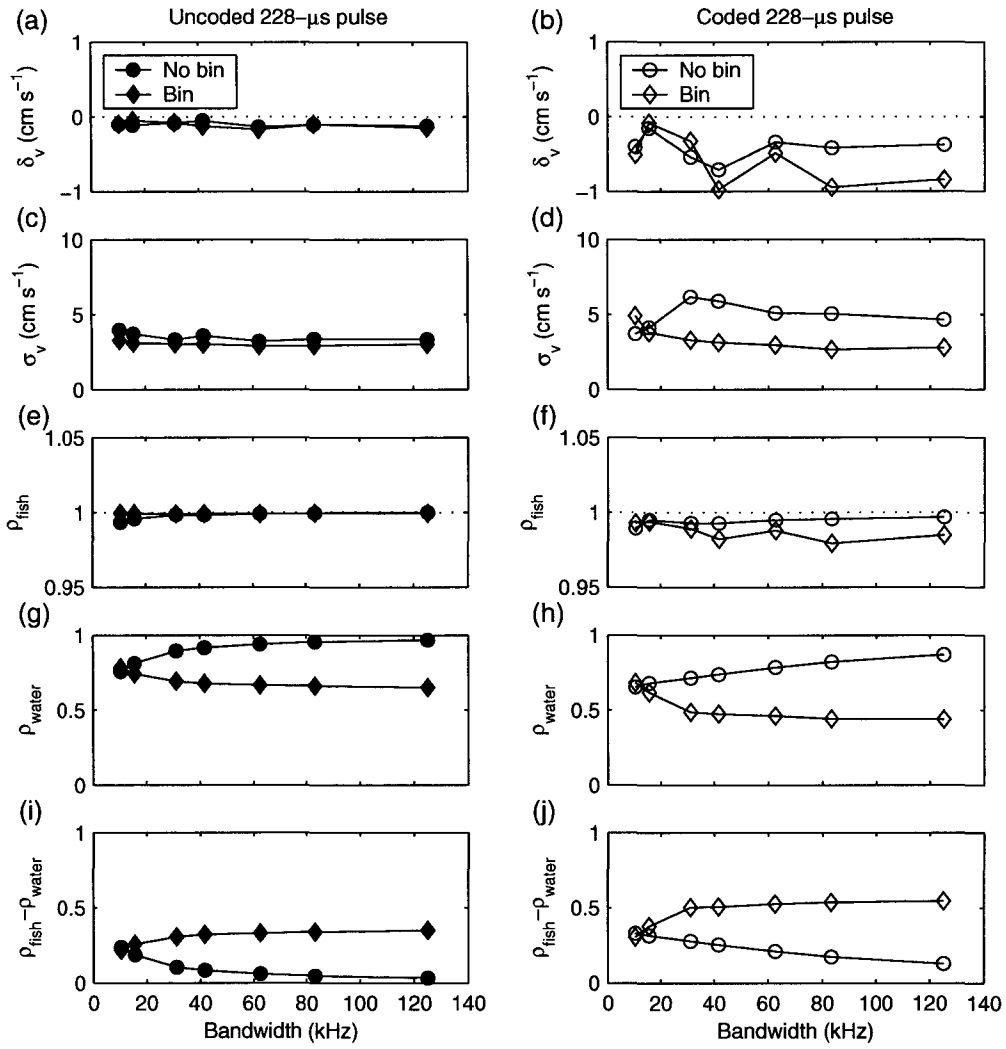

Figure 5.18: Plot of (a–b) δ_v (cm s^{-1}), (c–d) σ_v (cm s^{-1}), (e–f) ρ_{fish}, (g–h) ρ_{water}, and (i–j) $\rho_{fish} - \rho_{water}$ as a function of bandwidth for the computer model using uncoded pulses (solid plot symbols, first column) and coded pulses (hollow plot symbols, second column). Circles (•, ○) indicate results obtained by averaging 'instantaneous' velocities, and diamonds (♦,◇) indicate results obtained by averaging phase samples along the pulse length before calculating Doppler velocity. Error bars are smaller than the plot points at this scale.

their respective uncertainties. For the coded pulses, the errors observed with the bin method were slightly smaller than the corresponding no-bin errors, with a mean difference of $\delta_{v,NoBin} - \delta_{v,Bin} = -0.2 \pm 0.1$ cm s^{-1}.

The uncoded standard deviation decreases slightly with increasing bandwidth up to 31.25 kHz, then remains constant at 3.37 ± 0.06 cm s^{-1} and 2.99 ± 0.03 cm s^{-1} for the no-bin and bin methods respectively (Figure 5.18c). The coded standard deviation also experiences a drastic change around 31.25 kHz, at which point the no-bin σ_v rises to 6.3 cm s^{-1} while the bin σ_v decreases to 3.2 cm s^{-1} (Figure 5.18d). For bandwidths greater than 31.25 kHz, both no-bin and bin σ_v continue to decrease to values of 4.6 cm s^{-1} (no-bin) and 2.7 cm s^{-1} (bin). The value of σ_v for the binned, coded pulses is comparable to that of binned, uncoded pulses, and much lower than σ_v for no-bin, coded pulses.

At bandwidths less than 31.25 kHz, the correlation coefficient ρ is greater than 0.8 for both fish ($\rho_{fish} \approx 0.99$) and water ($\rho_{water} \approx 0.8$), and both pulse coding and the choice of bin/no-bin method makes little difference to the values of ρ_{fish}, ρ_{water} and their difference $\rho_{fish} - \rho_{water}$ (Figure 5.18e–j). By comparison, at bandwidths greater than 31.25 kHz, the difference $\rho_{fish} - \rho_{water}$ increases when using the bin method (Figure 5.18i, j) compared to the no-bin method. In particular, the difference using the bin method is greater for the coded pulses ($\rho_{fish} - \rho_{water} \approx 0.5$) than for the uncoded pulses ($\rho_{fish} - \rho_{water} \approx 0.3$), and much greater than the no-bin method for either uncoded pulses ($\rho_{fish} - \rho_{water} \approx 0.05$) or coded pulses ($\rho_{fish} - \rho_{water} \approx 0.15$).

The calculation of the correlation coefficient ρ is clearly affected by the combination of bandwidth, binning method, and pulse coding. Increasing the bandwidth improves estimates of ρ by increasing the number of phase samples used in its calcu-

lation. In an instrument with bandwidth greater than 30 kHz, the greater difference between ρ_{fish} and ρ_{water} calculated using the bin method could be exploited to discriminate fish targets from the water. In the test instrument, ρ was not used for target discrimination: the sample bandwidth was only 10 kHz and experimental results confirmed that the difference between fish and water ρ was not large enough to exploit for target discrimination. A truly broadband instrument does not appear to be necessary, since increasing the bandwidth beyond 40 kHz does not further increase the difference between ρ_{fish} and ρ_{water}.

5.5 Summary of model results

A model of coherent Doppler sonar operation was constructed, which allowed for confirmation of experimental results and exploration of some configurations not accessible with the test instrument. The model was configured to reproduce backscatter from a collection of weak scatterers moving at the same velocity (water mode), or a single strong scatterer with one velocity surrounded by a collection of weak scatterers with a different velocity (fish-plus-water mode).

Results for modelled water velocities were explored by configuring the model in both narrowband (30-kHz bandwidth) and broadband (125-kHz bandwidth) water modes. The broadband mode allowed for exploration of the spatial averaging ('binning') similar to that used in Doppler current profilers. The narrowband Doppler velocities were 33% too low because the velocity aliasing resulting from the limited bandwidth in the narrowband model shifted higher velocities to the opposite side of the velocity spectrum, biasing the mean velocity toward zero. The error was smaller

(14%) for the broadband model. The standard deviation in Doppler velocity followed the general form of Zrnic's (1977) Equation 2.32 for standard deviation as a function of lag, but was up to 8% greater than that predicted for the narrowband model, 11% greater than predicted for the broadband (125-kHz bandwidth) model (no binning), and 26% lower than predicted for the broadband model (with binning).

The model was configured in fish-plus-water mode in order to investigate the effects of varying target velocity and standard deviation, water velocity and standard deviation, lag, pulse length, pulse coding, SNR, and ρ. Error and standard deviation did not depend on target velocity when target velocity was varied between ± 100 cm s^{-1}. When a range of target velocities of up to ± 20 cm s^{-1} was introduced for a single fish, the error was not affected, but the standard deviation increased as the standard deviation of the target velocity increased. The measured standard deviation was approximately equal to the quadrature sum of the standard deviation for a point target and the standard deviation in the target velocity itself. When a range of water velocities up to ± 20 cm s^{-1} was introduced neither the error nor the standard deviation were affected. The error did not depend on the water velocity, but the standard deviation increased as the absolute difference between the fish velocity and the water velocity increased.

The error in the modelled fish velocity did not depend on lag, but the standard deviation was inversely proportional to lag, as in Zrnic's Equation 2.32. However, the modelled standard deviation was smaller than the predicted standard deviation by a factor of 0.61–0.76, suggesting that more independent samples were being used in the calculation of the Doppler velocity than was assumed for the theoretical calculation. The pulse length did not affect the error for either coded or uncoded pulses; however,

the standard deviation increased as the pulse length increased, which is inconsistent with experimental results. Furthermore, for some pulse lengths, the standard deviation for coded pulses was larger than for uncoded pulses, again in contrast to experimental results. It is possible that if pulse length and coding effects were present in the experiments, the additional uncertainty associated with experimental measurement obscured their measurement.

The effects of SNR and complex correlation coefficient ρ on error and standard deviation were investigated. For SNR $>$ 15 dB, model, experimental, and theoretical results for error and standard deviation were all in good agreement. However, for SNR $<$ 15 dB, experimentally measured error and standard deviation were both smaller than in the model. Therefore, it appears that the model fails to capture some essential feature of the low-SNR measurement environment. Results for error and standard deviation as a function of ρ are consistent with the same results plotted as a function of SNR, which is understandable as SNR and ρ are strongly related.

The effect of multiple targets in the modelled beam on Doppler velocity estimates are comparable to the observations from the target-array experiments: error and standard deviation increase somewhat erratically as targets overlap in the backscatter, reaching values as large as -25 cm s^{-1} for the error and 40 cm s^{-1} for the standard deviation.

Increasing the instrument bandwidth while maintaining the same pulse length and lag result in better ability to discriminate water from fish targets using the correlation coefficient ρ. For bandwidths greater than 40 kHz, the difference $\rho_{fish} - \rho_{water}$ is 0.3 for uncoded pulses and 0.5 for coded pulses, suggesting that ρ could be useful for target discrimination if the bandwidth were greater than 40 kHz and all other sonar

parameters kept the same. Furthermore, a larger bandwidth would allow for some phase averaging or binning along the pulse length, which will also reduce standard deviation in Doppler velocity estimates.

Model, experimental, and theoretical results have resulted in detailed knowledge of the effects of various experimental parameters on Doppler velocity estimates. The following chapter will present an overview of all the results, followed by a discussion how the results are relevant to achieving the goal of designing a realistic, stand-alone system capable of acquiring useful real-life data.

Chapter 6

Discussion

The results of Chapters 4 and 5 indicate that Doppler measurements of fish velocity are possible with the independent pulse-pair processing technique. Furthermore, measurements made with a purpose-built sonar and customized signal processing are superior to those obtained with either an off-the-shelf ADCP or incoherent processing methods. However, some interesting behaviour of Doppler velocity estimates has been uncovered, and needs to be explained before considering the larger-scale implications of this work.

6.1 What affects velocity estimates?

Lag, pulse length, pulse coding, target velocity, water velocity, bandwidth, SNR, and multiple targets were investigated in detail through experiments and computer models. Each investigation tried to answer two questions. First, does a particular parameter have an effect on the Doppler velocity estimates? Second, if there is an effect, is it predictable and consistent? In this section, experimental and model

results will be reviewed, assembled, and synthesized to understand what is important for good performance when measuring fish velocities with a Doppler sonar.

6.1.1 Target velocity

Section 4.4 explored the effects of target velocity on Doppler velocity measurements through examination of experimental results, while Section 5.3.1 explored the effects of changes in target velocity and target velocity standard deviation on Doppler velocity measurements through examination of computer model results.

The error in Doppler velocity measurements depended on target velocity for three of the towtank experiments (the short-range experiment and the two long range experiments), in which the Doppler velocity was biased by a factor of about 2% away from zero ($|v_{Doppler}| > |v_{tow}|$). In contrast, there was no signficant dependence of the error on target velocity for the target-array towtank experiment, the field experiments, or the model. Uncertainty in sound speed c is unlikely to be the culprit since the temperature in all three experiments was accurately known. Sonar alignment errors on the order of 10° would have been necessary to result in a 2% error in tow velocity; however, none of the experiments were set up with the targets far enough off-axis for a 10° misalignment to go undetected. It may be that in the three experiments which showed bias, which were set up with similar geometries, sidelobes scattering off tank walls or the surface contributed to the error, while the differing geometry in the other experiments minimized the effects of sidelobes. The source of the error thus remains unknown, but since it only appears in three of the seven experiments, and is small, it will be considered insignificant.

Target velocity did not have a significant effect on either measured or modelled

standard deviations, except in the case of the stationary field experiment, in which σ_v increased with fish swimming *speed*. Model results obtained with a range of target velocities suggest that the larger values for σ_v observed from live fish in the field experiments were caused by the fact that moving fish do not scatter a single frequency back to the Doppler sonar, but rather a range of frequencies. The fact that σ_v depends on fish swimming speed rather than velocity supports the idea that the increase is caused by swimming motion: faster-swimming fish have a greater displacement of their bodies about their centre of mass (Bainbridge, 1958). The greater displacement will increase the target velocity standard deviation, resulting in higher standard deviations in the Doppler estimates. The effects of fish motion will be considered in more detail in Section 6.1.7.

6.1.2 Water velocity

Systematic investigations of the effects of water velocity on Doppler velocity estimates for solid targets were limited to model results from Section 5.3.2, as it was impossible to control the mean and standard deviation in water velocity in the experiments.

The velocity error does not depend on the mean or standard deviation of water velocity. The velocity standard deviation does not depend on the standard deviation in water velocity but does depend on the absolute difference between target velocity and mean water velocity. An increase in standard deviation from 2.5 $\mathrm{cm\,s^{-1}}$ to 4.8 $\mathrm{cm\,s^{-1}}$ was observed over the range $0 \leq |v_{fish} - v_{water}| \leq 150$ $\mathrm{cm\,s^{-1}}$ (with lag $\tau = 1152$ μs). In practice, this means that the standard deviation is expected to increase as the difference between fish and water velocity increases, but is not expected to increase as turbulence increases. The caveat is that maximum range is limited by

turbulence, as the increased scatter through turbulent water results in lower SNR. The dependence of σ_v on the difference between water and fish velocity could explain some of the increased standard deviation observed in the field experiments relative to the towtank experiments. In the field experiments, the water and fish were generally moving in opposite directions and the fish velocity estimates would therefore suffer from an increase in σ_v of approximately 2 cm s^{-1} above the minimum value (for the 1152-μs lag, as in the model).

6.1.3 Pulse length

The effects of pulse length on error and standard deviation were determined by examining experimental results in Section 4.5 and model results in Section 5.3.4.

Pulse length did not affect the error in either experimental or modelled Doppler velocity estimates. Linear fits to standard deviation as a function of pulse length for the experiments did not suggest a dependence of σ_v on pulse length, although some linear fit parameters almost surpassed the threshold for significance. The modelled standard deviation increased with pulse length for both uncoded and coded pulses, with a slope of 0.0047 ± 0.0007 cm s$^{-1}/\mu$s for uncoded pulses and 0.011 ± 0.006 cm s$^{-1}/\mu$s for coded pulses. It is possible that the model simply removed some confounding factors and allowed the dependence of σ_v on pulse length to be more clearly observed than in the experiments.

The increase in σ_v with pulse length is not large or consistent enough among experiments to discourage the use of longer pulse lengths. In particular, for the relatively narrow-band instrument used in these experiments, slightly larger pulse lengths would be desirable. For example, a 30-cm pulse would put more power into

the water and increase the likelihood of detecting a fish, while still maintaining spatial resolution smaller than a typical fish's size.

6.1.4 Pulse coding

The effects of pulse coding on error and standard deviation were determined by examining experimental results in Section 4.5 and model results in Section 5.3.4.

The error was not affected by pulse coding for experimental or model results. Experimental results showed that using coded pulses had no effect on standard deviation. Model results imply that using coded pulses could increase σ_v by 1–2 cm s^{-1} (30–50%) compared to σ_v for an uncoded pulse of the same length in a narrowband instrument. In addition, the modelled coded-pulse standard deviation increases with pulse length at a greater rate than for uncoded pulses (0.011 ± 0.006 cm s$^{-1}/\mu$s compared to 0.0047 ± 0.0007 cm s$^{-1}/\mu$s). Since coded pulses do not affect error or standard deviation in the experimental data, there is no convincing reason to use coded pulses in a narrow-band instrument (such as the test instrument). However, some model results have suggested that coded pulses could be useful for target discrimination in a higher-bandwidth instrument. The combined effects of bandwidth and pulse coding will be discussed further in Section 6.1.6.

6.1.5 Multiple targets

Multiple targets presented both spatial resolution and velocity estimation challenges for the sonar. Spatial resolution problems, such as multiple targets being identified as a single target, depended on pulse length as well as target size and spacing. Velocity estimation problems arose when phase information was corrupted by particular

combinations of lag, pulse length, and target spacing, resulting in anomalously large values of error and standard deviation.

The target-array experiment results outlined in Section 4.3.1 allowed for investigation of spatial resolution and velocity accuracy when the sonar encountered groups of targets of various sizes and spacings. The lower limit on spatial resolution achieved by the test instrument of 6.6 cm was approximately equal to its spatial sampling interval of 7.2 cm; however, even with a 7.2-cm pulse length, it was not possible to consistently resolve the 6.6-cm-spaced targets. The minimum resolvable target spacing depended on pulse length T and was equal to approximately $1.4R_T$, where $R_T = \frac{cT}{2}$ is the pulse length expressed as equivalent range.

Poor Doppler velocity error and standard deviation were observed when targets overlapped in the backscatter detected by the sonar, even though the targets were moving at the same velocity. Both towtank and model results support the need for caution when choosing pulse length and lag. The combinations of pulse lengths used with lag $\tau = 768$ μs in the target-array experiment resulted in larger values of error and standard deviation when the pulse lengths and target spacing were such that there was overlap in their backscatter and corruption of the phase information needed for Doppler velocity calculation. For example, with overlapping targets, the error was approximately 10 cm s^{-1} and the standard deviation was approximately 20–35 cm s^{-1}, compared to 1 cm s^{-1} and 5 cm s^{-1}, respectively, with no overlap. The error and standard deviation increased even when there was only partial overlap in backscatter. Model results are consistent in magnitude with the target-array results, with error as large as -25 cm s^{-1} and standard deviation as large as 40 cm s^{-1} when targets were overlapping. The sign of the error was likely related to the spacing of

the targets (recall that the wavelength λ of the 250-kHz test instrument is 0.6 cm). There was a degree of unpredictability in the increases in δ_v and σ_v, which did not vary smoothly as the target spacing was changed.

The increased Doppler velocity uncertainty was caused by the corruption of the phase information used to calculate velocity using the independent pulse-pair technique. In order to better understand the interaction among target spacing, target size, pulse length, and lag, consider an array of three equally-spaced targets insonified with a pair of pulses in a variety of arrangements. Figure 6.1 depicts the target arrangement (first row), the transmitted pulse pair (second row), the backscatter arising from the first pulse (third row) and the second pulse (fourth row), and the sum of the backscatter arising from both pulses (fifth row). The ideal situation is one with small targets and short pulse lengths in which the scatter from the first pulse for all targets is detected before that from the second pulse (column I in Figure 6.1). If the targets are more widely spaced, the second-pulse backscatter from the nearer targets will overlap with the first-pulse backscatter from the further targets (column II in Figure 6.1). If the targets are more widely spaced and, in addition, the pulse is longer, the sonar will at times be receiving backscatter from two targets simultaneously (column III in Figure 6.1). If the targets are large and widely spaced, and the pulse is longer, there will be still more overlap in backscatter (column IV in Figure 6.1). The examples shown in Figure 6.1 are for a particular combination of pulse lengths and lags, target size and spacing, but it is easy to imagine any combination of those factors which could cause interference.

The problems in Doppler velocity estimation arise when backscatter from more than one target overlaps. Targets backscatter can overlap in one of two ways: two

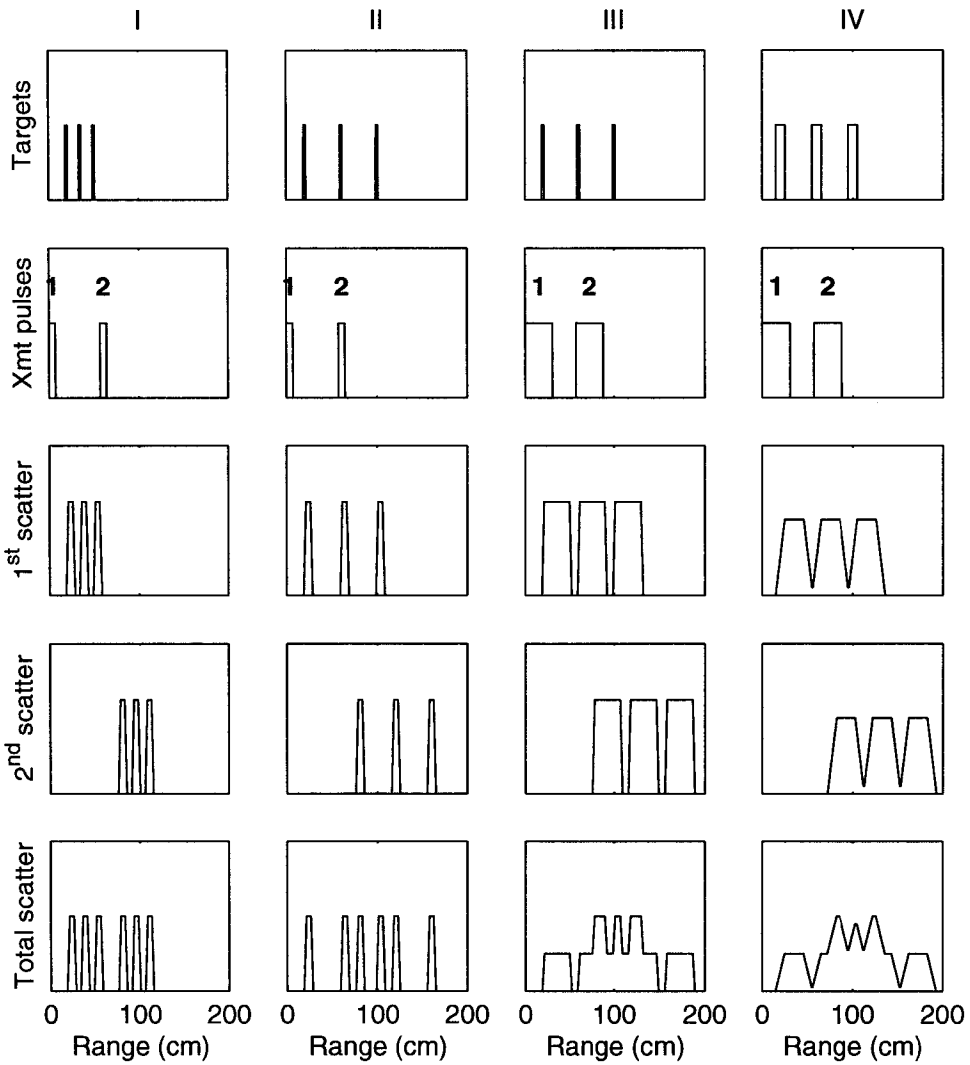

Figure 6.1: Plot of ideal backscatter envelope for $\tau = 57$ cm: Column I, 3×2.5-cm targets, 15 cm spacing, 7.1-cm pulses; Column II, 3×2.5-cm targets, 40 cm spacing, 7.1-cm pulses; Column III, 3×2.5-cm targets, 40 cm spacing, 30.9-cm pulses; Column IV, 3×10.2-cm targets, 40 cm spacing, 30.9-cm pulses. First row, targets; second row, transmit pulses; third row, backscatter from first pulse; fourth row, backscatter from second pulse; fifth row, total backscatter.

targets may occupy the same range bin at different angular positions within the beam, or two targets may occupy different range bins, but the range bins are separated by (say) the same distance as the lag. In order to avoid problems of the first type the beam should be relatively narrow; exactly how narrow the beam should be will depend on the expected fish density, as outlined below. The sample volume V_s is related to the beam angle ϕ, the range R, and the sampling interval $\delta_R = \frac{c}{2f_S}$ where f_S is the sampling frequency, by the following expression:

$$V_s = \frac{1}{3}\pi \tan^2\left(\frac{\phi}{2}\right)\left((R+\delta_R)^3 - R^3\right) \tag{6.1}$$

Since $\delta_R \ll R$, the R^3 terms in Equation 6.1 cancel and the leading significant term is in $R^2\delta_R$. The characteristic fish density N_F will be equal to the inverse of the sample volume:

$$N_F = \frac{1}{\pi \tan^2\left(\frac{\phi}{2}\right) R^2 \delta_R} \tag{6.2}$$

For example, with the 4° beamwidth of the test instrument, the 7.2-cm sampling interval translates into a sample volume of 0.24 m^3 at 30 m range and 0.99 m^3 at 60 m range. The corresponding maximum fish densities are 4 fish m^{-3} and 1 fish m^{-3}; greater fish densities will result in a higher probability of two fish occupying the same range bin at the same time. It is true that a broader beam could conceivably insonify more targets, but if the Doppler velocity estimates have unpredictable uncertainties which will not improve with further averaging, there is no advantage to having a broader beam. In other words, it is better to reliably measure the Doppler velocity of fewer fish than to insonify more fish but discard their velocity measurements.

A similar calculation to that in Equation 6.1 can be used to relate the pulse length

T and lag τ to the minimum volume 'between' fish. In this case, if the fish is within a range equivalent to the sum of the lag and pulse length, overlap will be a problem, so the equivalent expression for sample volume V_s and maximum fish density N_F is

$$\begin{aligned} V_s &= \frac{1}{3}\pi \tan^2\left(\frac{\phi}{2}\right)\left(\left(R+\frac{c(\tau+T)}{2}\right)^3 - R^3\right) \\ N_F &= \frac{1}{V_s} \end{aligned} \tag{6.3}$$

In general, the approximation used to modify Equation 6.1 is not valid when the difference between the two range terms is $c(T+\tau)/2$ instead of the much smaller δ_R, so the full expression in Equation 6.3 must be used. Equation 6.3 will result in smaller maximum fish densities than those given by Equation 6.2 and thus it is Equation 6.3 which will ultimately limit the fish densities for which Doppler fish velocity can be successfully measured.

The maximum fish densities calculated using Equation 6.3 will, of course, depend on lag and pulse length, and are plotted for three combinations of lag and pulse length in Figure 6.2. For example, at 20 m range, the maximum densities are 0.3, 0.6, and 1.3 m^{-3} for lags of 576, 1152, and 2304 μs respectively; at 60 m range, the maximum densities are 0.03, 0.07, and 0.14 m^{-3} at the same lags. These fish densities must be put into the context of expected fish concentrations: in the stationary field experiment, a situation with extremely high fish density of migrating sockeye salmon, approximately 8000 fish were identified in the data while only about 1 in 100 fish were excluded because they were one lag apart from a second fish. Higher fish densities have been observed in schooling fish, for example, 11 m^{-3} for Atlantic herring (Trevorrow and Claytor, 1998), or up to 1 m^{-3} for Atlantic cod (Rose, 1993), and in those cases it

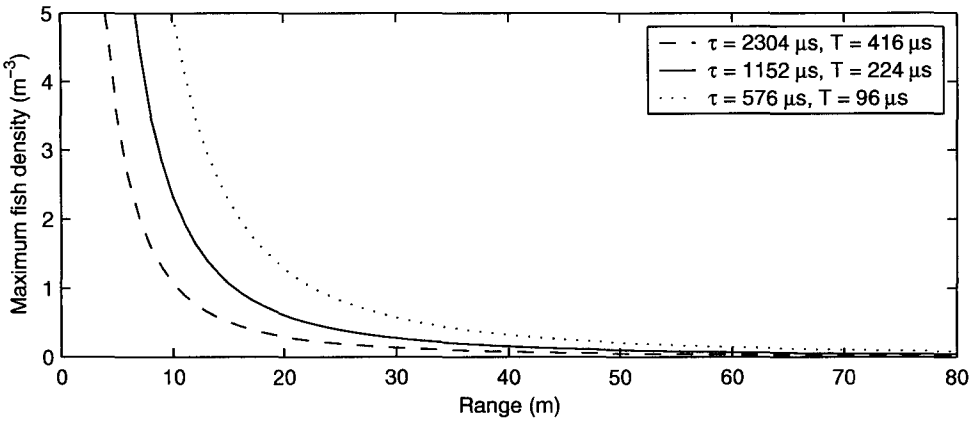

Figure 6.2: Plot of maximum fish density (m^{-3}) as a function of range (m) for some combinations of lag and pulse length used in the experiments.

would be increasingly likely that the closely-spaced fish would cause interference with Doppler measurements, depending on the particular hardware configuration used. Therefore, the particulars of a given experiment would ultimately determine whether acceptable measurements could be made.

6.1.6 Bandwidth

In Section 5.4.2, the effects of bandwidth on the error and standard deviation in Doppler velocity estimates were examined using the model. The model was originally configured to replicate the performance of the test instrument, and then expanded to examine alternative bandwidth and sampling combinations.

The transmit bandwidth in the test instrument is nominally 30 kHz but in practice the bandwidth is limited by the sample bandwidth of 10 kHz. An increase of sample bandwidth to at least equal the 30 kHz hardware limit would allow for some averaging

to take place along the pulse length resulting in a small decrease in standard deviation of 1 cm s^{-1} or 25%.

More importantly, a larger bandwidth would result in better estimates of the complex correlation coefficient ρ, which would greatly enhance the capability to differentiate fish from water. The expected values of the complex correlation coefficient for fish and water are $\rho_{fish} = 1$ (solid target with perfect correlation) and $\rho_{water} = 0.5$ (collection of targets with random positions). Model results suggest that correlation coefficient estimates could be improved, and the difference between ρ_{fish} and ρ_{water} increased, by increasing the bandwidth to 40 kHz (16% of 250 kHz) and transmitting coded pulses. Greater differences between ρ_{fish} and ρ_{water} would translate into a greater ability to discriminate fish from water, resulting in better velocity estimates and more convincing target identification. With the test instrument, the difference between ρ_{fish} and ρ_{water} was not large enough to reliably identify fish in water because the sample bandwidth was limited to 10 kHz (4% of 250 kHz).

6.1.7 Lag, SNR, and ρ

According to Zrnic's (1977) theoretical treatment, the standard deviation σ_v of independent pulse-pair Doppler velocity estimates is a function of lag τ, SNR, and complex correlation coefficient ρ. The functional relationship is given by Equation 2.32, repeated here for convenience:

$$\sigma_v = \frac{c}{4\sqrt{2}f_0\pi\tau}\frac{1}{\sqrt{M}}\sqrt{\frac{\left(1+\frac{P_N}{P_S}\right)^2 - \rho^2}{\rho^2}} \tag{6.4}$$

where f_0 is the transmit frequency, τ is the lag between the pair of pulses, P_S and P_N are the signal and noise power per sample, ρ is the magnitude of the correlation calculated from hard limited data (signal intensity removed), and M is the number of pulse pairs used to calculate the average. Therefore, the discussion of the dependence of the standard deviation on any one of lag, SNR, or ρ must include all three variables. Experimental dependence of error and standard deviation on lag are discussed in Section 4.2, and the dependence on SNR and ρ are discussed in Section 4.7. The equivalent model results are discussed in Sections 5.3.3 for lag, and Section 5.3.5 for SNR and ρ.

Experimental and modelled values of error did not depend on lag. The error did depend on SNR in both the experiments and the model. In the experiments, the dependence of error on SNR was linear over the range 0–80 dB, with a slope of -0.008 ± 0.004 cm s^{-1}/dB. The modelled results showed errors up to –40 cm s^{-1} for SNR < 15 dB which decreased rapidly to less than ± 1 cm s^{-1} for SNR > 15 dB. Experimental values of δ_v did not depend on ρ, while the dependence of modelled values of δ_v as a function of ρ was consistent with the dependence on SNR. The modelled values of δ_v were large when $\rho < 0.9875$, which corresponded to the range SNR < 15 dB; the values of δ_v decreased to less than ± 1 cm s^{-1} for $\rho > 0.9875$, which corresponded to the range SNR > 15 dB. The model results for δ_v suggest that the Doppler estimate of target velocity approaches the water velocity as SNR $\rightarrow 0$ dB.

The predicted standard deviation σ_{vP} was calculated for each target in the experiments and the model, using the actual values of lag τ, SNR, and ρ for each target, and was compared with the measured standard deviation σ_v by calculating the ratio $R_{mp} = \sigma_v/\sigma_{vP}$. Figure 6.3a is a histogram of the ratio R_{mp} for the experimental

results, and Figure 6.3b is a histogram of the ratio R_{mp} for the model results. The mean and standard deviation was $R_{mp} = 1.000 \pm 0.607$ (standard error 0.004) for the experiments and $R_{mp} = 1.023 \pm 0.409$ (standard error 0.014) for the model. The ratio R_{mp} was equal to unity within uncertainty for the experimental results, and very close ($\pm 2\%$) for the model results.

In order to determine whether the agreement of the standard deviation with predicted standard deviation was affected by the values of SNR and ρ, the ratio R_{mp} of measured to predicted standard deviation is plotted as a function of SNR and ρ as a false-colour plot in Figure 6.3c for the experimental results, and Figure 6.3d for the results (for targets with lag $\tau = 1152$ μs). In Figure 6.3c, the experimentally measured standard deviation is smaller than the predicted standard deviation for SNR < 15 dB and $\rho > 0.985$. The predicted standard deviation is very sensitive to small changes in ρ when $\rho \rightarrow 1$, and model results suggest that when SNR is less than 15 dB, ρ should be less than 0.985. It is possible that the experimentally derived estimates of ρ were too high for some targets for which SNR was less than 15 dB. In Figure 6.3d, the modelled standard deviation is approximately equal to the predicted standard deviation regardless of SNR of ρ.

The lower-than-expected experimental σ_v for SNR < 15 dB is not related to the relative water velocity. Model results from Section 5.3.2 suggest that σ_v will be smaller when $v_{fish} = v_{water}$ compared to the case when $v_{fish} \neq v_{water}$. Experimental data resulted in smaller-than-predicted standard deviations for SNR < 15 dB, which might be expected if the low-SNR data primarily originated in the towtank experiments (in which $v_{fish} = v_{water}$). However, only half of the low-SNR experimental results originate from towtank experiments, and the remainder originate from fish experiments,

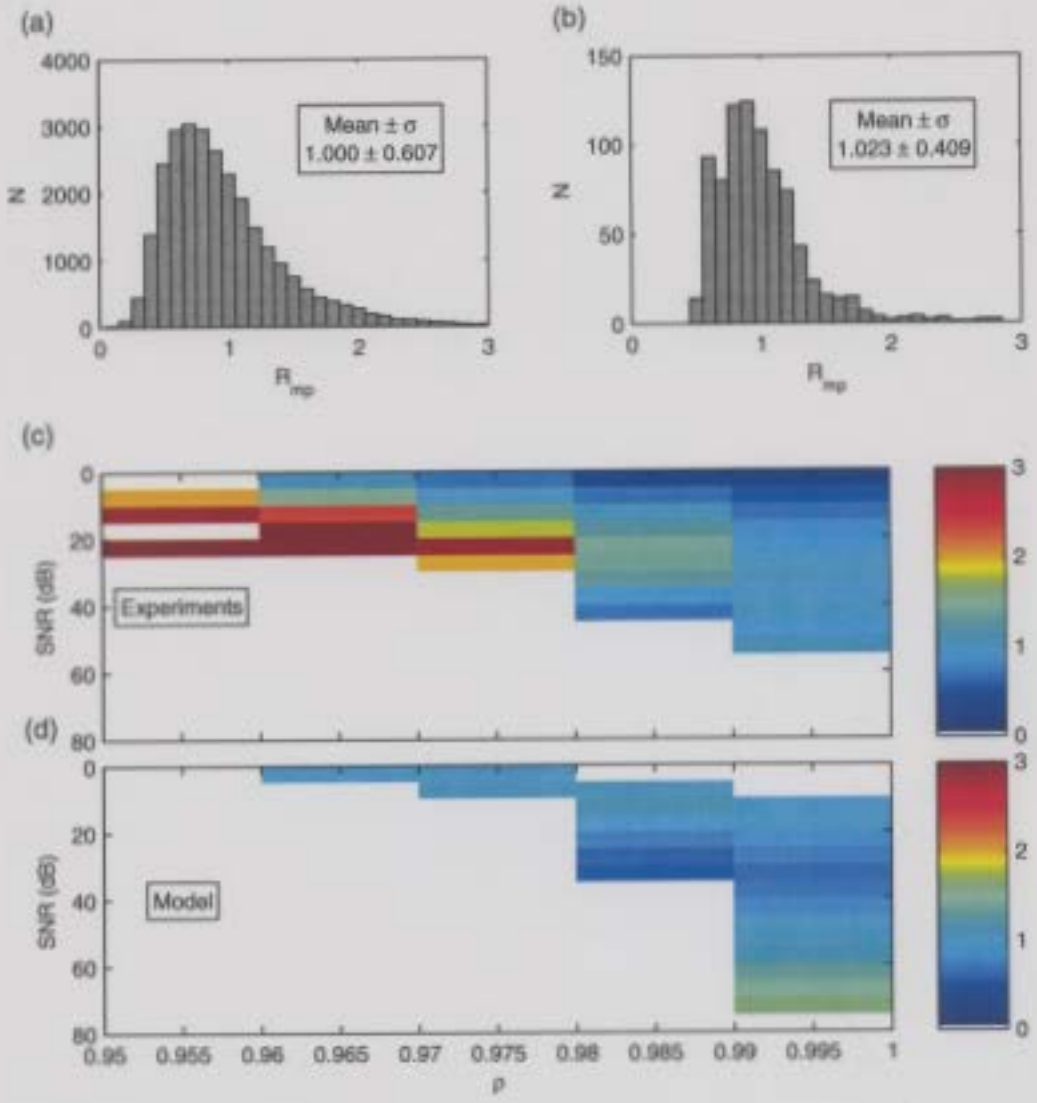

Figure 6.3: Histograms of R_{mp} for (a) experiments and (b) model results, and false-colour images R_{mp} as a function of SNR and ρ for (c) experiments and (d) model results.

where $v_{fish} \neq v_{water}$. Therefore, the relative water velocity is not the source of the decrease in standard deviation for SNR < 15 dB.

In light of the present results, some elements of the theoretical path to Equation 2.32 bear consideration. The signal being analyzed is assumed to have a Gaussian frequency distribution of spectral width w (in Hz) superimposed over white noise, with the autocorrelation r at a lag τ given by

$$r(\tau) = P_S \left[e^{-2\pi^2 w^2 \tau^2} \right] e^{i\omega_0 \tau} + P_N \delta_{\tau,0} \tag{6.5}$$

where P_S is the signal power, P_N is the noise power, and ω_0 is the mean angular frequency. The magnitude of $r(\tau)$ in Equation 6.5 for $\tau \neq 0$ is

$$|r(\tau)| = P_S \left[e^{-2\pi^2 w^2 \tau^2} \right] \tag{6.6}$$

The relationship between $r(\tau)$ and the complex correlation coefficient $\rho(\tau)$ measured in the experiments and model is

$$\rho = \frac{|r(\tau)|}{P_S} = e^{-2\pi^2 w^2 \tau^2} \tag{6.7}$$

Initially, one might believe the spectral width w to be equal to the bandwidth (30 kHz). However substitution of $w = 30 \times 10^3$ Hz in Equation 6.7 results in $\rho \to 0$, clearly not equal to observed values of ρ. The limiting spectral width in Doppler sonar measurements of fish velocity is not the sonar bandwidth; rather, it is determined by the frequency spread of the backscattered signal.

In order to explore this relationship, consider first two identical pulses, which will

result in a correlation of unity. By extension, scattering from a solid target moving at velocity v in the beam direction will give a single Doppler shift, with no further widening of the spectrum beyond the intrinsic signal bandwidth. However, scattering from a fish target in which different parts of the target are moving at different speeds will result in a range of effective Doppler shift frequencies, and consequently a spectral widening.

The spectral widening can be explained by considering a simplified model of fish motion. Assume the swimming motion of a fish of length L causes it to bend $\frac{3}{4}$ of the way along its body, near the tail, at an angle θ, as depicted schematically in Figure 6.4. The fish's body undergoes a 'wiggling' motion of frequency f_W, sometimes called the tail-beat frequency. It will take one-quarter of a wiggle cycle ($\frac{1}{4f_W}$) for the tail to move from the centre to the maximum amplitude. The movement will induce a Doppler shift due to the speed of the tail along the beam direction: if it is head-on or tail-on in the sonar beam, it has moved $\frac{L}{4} - \frac{L}{4}\cos\theta$ closer to the transducer during the $\frac{1}{4f_W}$ period of time. Therefore the velocity v_T of the tail can be calculated by estimating the change in range ΔR during a given time interval Δt

$$\begin{aligned} v_T &= \frac{\Delta R}{\Delta t} \\ &= \frac{\frac{L}{4} - \frac{L}{4}\cos\theta}{\frac{1}{4f_W}} \\ &= f_W L\,(1 - \cos\theta) \end{aligned} \tag{6.8}$$

Substituting Equation 6.8 into the Doppler shift relation (Equation 2.6), the addi-

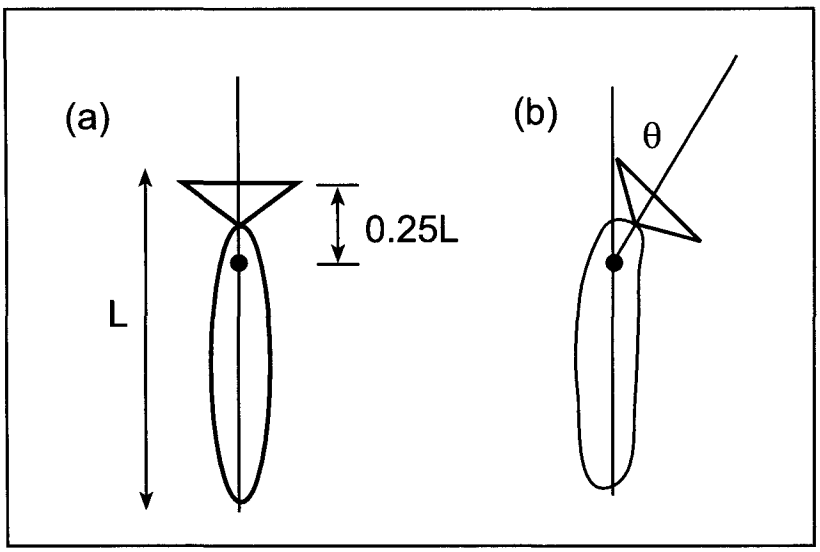

Figure 6.4: Diagram of swimming fish model, for a fish of length L (a) fish at rest, (b) fish with tail at maximum amplitude, angle θ.

tional Doppler shift because of the relative motion of the tail f_{DT} would be

$$\begin{aligned} f_{DT} &= \frac{2f}{c} v_T \\ &= \frac{2 f_0 f_W L}{c} (1 - \cos\theta) \end{aligned} \tag{6.9}$$

where f_0 is the transmit frequency and c the speed of sound. For observations at an angle to the fish's main body axis (head-tail axis), Equation 6.9 would be multiplied by an additional factor of $\cos\phi$ where ϕ is the angle relative to the head-tail axis in the vertical plane.

Figure 6.5 is a contour plot of the predicted Doppler shift as a function of tail deviation angle θ and fish length L. For fish lengths up to 1 m and tail angles θ up to 45° Equation 6.9 predicts shifts of 0–70 Hz for head or tail-on observation, corresponding to a velocity range of 0–21 cm s^{-1} ($f_0 = 250$ kHz and $c = 1500$ m s^{-1}).

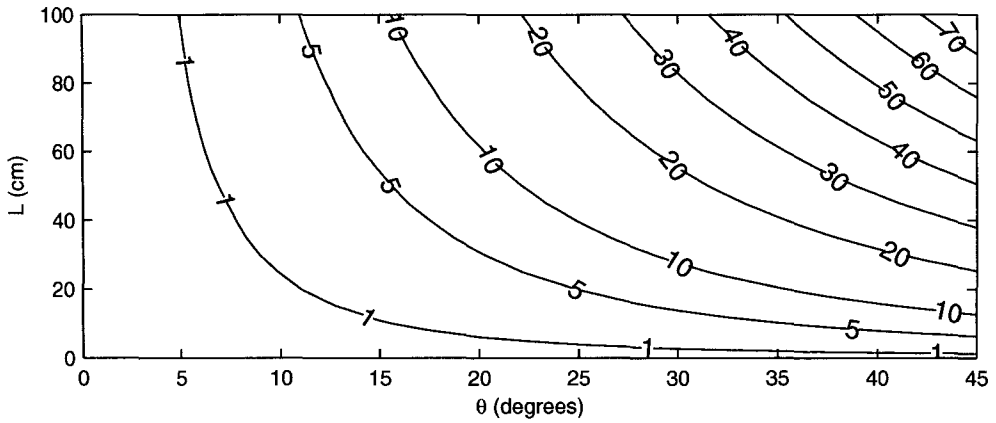

Figure 6.5: Contour plot of tail-induced Doppler shift f_{DT} as a function of fish length L and angle of maximum tail deviation θ.

Data collected in the silo tank provide an ideal opportunity to test the accuracy of Equation 6.9. In particular, several fish in the video were visible in head-on or tail-on view with their tails beating several times near the scale-calibrated plane defined by the laser beam. The tail positions had already been marked during the data analysis (Section 3.6), which made it possible to estimate values for f_W and θ. The 4-cm maximum observed displacement of the tail from the centreline of the fish, coupled with the approximate fish length of 30 cm, resulted in a value of $\theta \approx 30°$ for the angle of maximum deviation. Video observations of several tail beats resulted in a value for the tail-beat frequency of $f_W \approx 0.8$ Hz. Substitution of $\theta = 30°$, $f_W = 0.8$ Hz, $f_0 = 250$ kHz, and $L = 30$ cm into Equation 6.9 resulted in a frequency shift of 11 Hz. Substitution of $w = 11$ Hz into Equation 6.7 results in $\rho = 0.9992, 0.9969,$ and 0.9877 for lags of 576 μs, 1152 μs, and 2304 μs, respectively, which fall well within the range of observed ρ of 0.9476–0.9999.

Based on the above arguments, spectral spreading could be caused by fish motion.

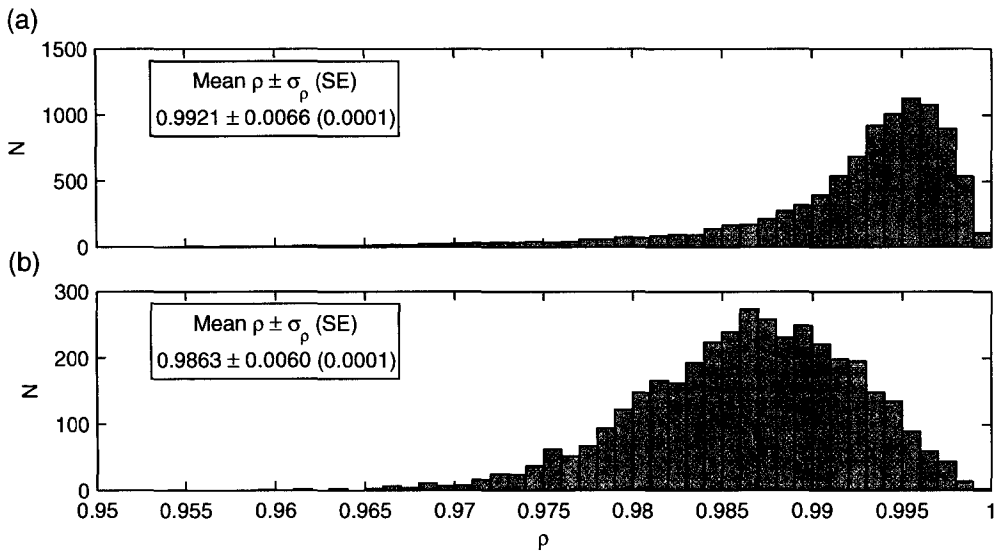

Figure 6.6: Histogram of ρ for (a) styrofoam ball and (b) fish targets for lag $\tau = 1152$ μs.

Figure 6.6a is a histogram of ρ for all styrofoam ball targets, and Figure 6.6b is a histogram of ρ for all tail-on fish targets. The mean values of ρ are 0.9921 ± 0.0001 for styrofoam balls and 0.9863 ± 0.0001 for stationary field experiment fish targets (assumed to be tail-on observations, on average), and the two values of ρ are significantly different. Furthermore, ρ is lower for fish than for styrofoam balls, which would be expected with a broader spectrum of backscattered frequencies. In addition, the values for ρ for fish covered a wider range than those for the styrofoam balls, which would be expected since many (unknown) sizes and orientations of fish were observed, while the (spherical) balls looked the same to the sonar from any orientation. Applying Equation 6.7 with the mean values of ρ gives a spectral spread of $w = 17$ Hz for the styrofoam balls and $w = 23$ Hz for the fish.

6.2 Implementation

All the preceding discussion is pointless if the results are not synthesized into a set of guidelines for implementation of a real system which could be applied in the field. Among the key considerations for a real system are beam geometry and expected fish density, pulse length and lag, bandwidth, frequency, and the ability to discriminate fish targets from water.

6.2.1 What makes a 'good' measurement?

Typical expected fish velocities are required to put the size of the error and standard deviation into context. Fish velocities vary widely, from sustained swimming at 1 body length s^{-1} to short bursts as fast as 3 body lengths s^{-1}; however, for the purposes of this discussion, a 'typical' fish swimming velocity is required. A velocity of 1 body length s^{-1} translates to 60 cm s^{-1} for a 60-cm long salmon or 30 cm s^{-1} for a 30-cm long cod. The average of all fish speeds observed in the stationary field experiment was 20 cm s^{-1}. Therefore, fish velocities might realistically fall in the range 20–60 cm s^{-1}. As a compromise, 30 cm s^{-1} will be used for a typical fish velocity in the discussion of measurement uncertainty.

There are two components to the uncertainty: the error δ_v and the standard deviation σ_v. The average value of the error for all targets in the experiments is 0.01 ± 0.02 cm s^{-1}, equal to zero within uncertainty; a more useful estimate of the size of the error is its average absolute value, which is 2 cm s^{-1}. The standard deviation depended primarily on lag τ and the average σ_v was 12.8 cm s^{-1} for $\tau = 576$ μs, 7.2 cm s^{-1} for $\tau = 1152$ μs, and 4.9 cm s^{-1} for $\tau = 1152$ μs. However, an average

of $N = 89$ velocity estimates were used to calculate the Doppler velocity, and the uncertainty in the mean $\sigma_{\overline{v}}$ is related to the standard deviation σ_v by $\sigma_{\overline{v}} = \frac{\sigma_v}{\sqrt{N}}$. For $N = 89$, $\sigma_{\overline{v}} \approx 0.1\sigma_v$. Therefore, averaging of all the velocity estimates for a single fish reduces the uncertainty arising from the standard deviation to 1.4 cm s^{-1}, 0.8 cm s^{-1}, and 0.5 cm s^{-1} for the 576-μs, 1152-μs, and 2304-μs lags, respectively.

The error and standard deviation combine to give a total uncertainty ϵ:

$$\epsilon = |\delta_v| + \left(\frac{\sigma_v}{\sqrt{N}}\right) \tag{6.10}$$

Substitution of $\delta_v = 2$ cm s^{-1}, $N = 89$, and $\sigma_v = 12.8, 7.2, 4.8$ cm s^{-1} into Equation 6.10 results in total uncertainty of 3.4 cm s^{-1} for $\tau = 576$ μs, 2.8 cm s^{-1} for $\tau = 1152$ μs, and 2.5 cm s^{-1} for $\tau = 2304$ μs.

Comparing the overall uncertainty of 2.5–3.4 cm s^{-1} with the typical swimming velocity of 30 cm s^{-1} results in a 8–11% uncertainty. The dominant term in Equation 6.10 is $|\delta_v|$ which was less than ± 1 cm s^{-1} for half the targets identified in the experiments. Substitution of $|\delta_v| = 1$ cm s^{-1} into Equation 6.10 results in ϵ ranging from 1.5–1 cm s^{-1}, or 4–6% of the fish swimming velocity.

The overall uncertainty, therefore, can range between 1.5–3.4 cm s^{-1}, depending on a variety of experimental factors. Assuming a fish swimming velocity of 30 cm s^{-1}, the percentage uncertainty for the velocity of a single fish lies between 4% and 11%. For a fish swimming faster than 30 cm s^{-1}, the relative uncertainty will be correspondingly smaller. Sampling the velocities of many fish will further reduce both components of the uncertainty (the error will average to zero, and the standard deviation is reduced by a factor of $\frac{1}{\sqrt{N}}$), and this will be explored in Section 6.2.3.

6.2.2 Beam geometry

Doppler velocity techniques can only estimate the velocity component parallel to the sonar beam. Useful data for swimming fish would have to include three velocity components, which can be measured in one of two ways: either multiple beams are aimed at a single volume of interest and simultaneously measure three components of a single fish's velocity, or multiple beams which do not encompass the same volume build a statistical description of average fish velocities in the region surrounding the instrument (similar in concept to an ADCP). However, multiple beams all aimed at the same volume would require separate instruments positioned at some distance from each other, and since the goal is to propose a simple self-contained geometry, the focus will be on the ADCP-based geometry. If the assumptions used in current velocity measurement about uniformity of movement and small vertical velocities can be made for fish, an appropriate starting point for open-ocean measurements would be four beams arranged in a 'Janus configuration', in which beams are separated by 90° in the azimuth and inclined at an angle to the vertical, as in Figure 1.1. Riverine applications would require a slightly different geometry, for example, two horizontal beams. A third beam could be oriented vertically to measure the vertical velocity, or the vertical velocity could be assumed to be small and ignored.

Figure 6.7 is a schematic diagram of the side view of two opposing beams arranged in a downward-looking Janus configuration. (Alternatively, the beams could be the two horizontal beams for a riverine measurement.) The individual transducers are capable of detecting fish at a maximum range R, and the beams are at an angle θ to the vertical. The diverging beams will limit the horizontal extent of fish schools that can be observed, and the angle θ will also affect the vertical extent V_{ext} over which

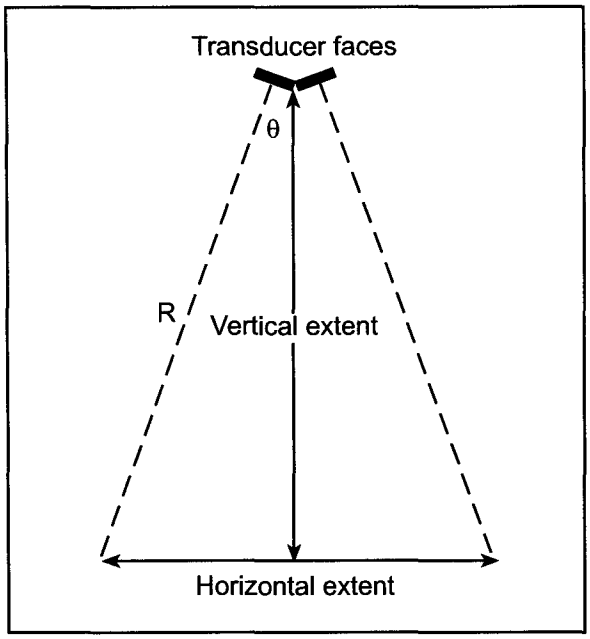

Figure 6.7: Schematic diagram of beam geometry, a side view of two of four beams in Janus configuration with angle θ relative to the vertical and range R along the beam direction.

observations can be made. Horizontal extent H_{ext} and vertical extent V_{ext} are related to maximum range R along the beam and angle θ with the vertical by

$$H_{ext} = 2R \sin \theta \tag{6.11}$$

$$V_{ext} = R \cos \theta \tag{6.12}$$

Figure 6.8a is a plot of horizontal extent H_{ext} as a function of angle θ from the vertical for a transducer capable of detecting targets to 70 m range along the beam direction, and Figure 6.8b is a plot of vertical extent V_{ext} as a function of angle θ. Fish schools vary widely in size, from tens to hundreds of metres in length and width (Ryan et al., 1996; Trevorrow and Claytor, 1998). With angle θ from the vertical ranging

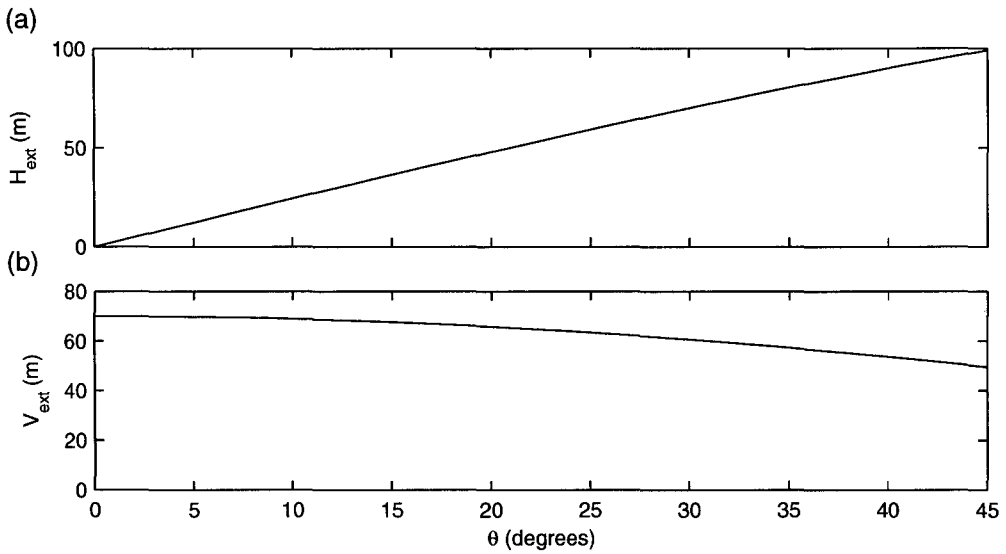

Figure 6.8: Plot of horizontal and vertical extent of sonar beams as a function of angle relative to vertical for opposing beams in a Janus configuration.

from 20–30°, the horizontal extent varies from 48–70 m, and the vertical extent varies from 60–65 m, which would be sufficient for medium-sized fish schools. The implied assumptions are that the fish movements are relatively uniform over the horizontal extent covered by the beams, and the movements of the observed fish can be taken as representative of the movements of all the fish. The preceding assumptions are already widely used by biologists when observing the movements of each individual animal is impossible or impractical.

6.2.3 Fish density

In order to assess whether a multiple-beam geometry would sample enough fish over time to make a sensible measurement of fish velocity, consider the probability of detecting a fish in a single beam in a given period of time. To calculate this probability,

consider first the fish 'flux' F_{fish}, that is, the number of fish per second passing through a volume with cross-sectional area A:

$$F_{fish} = v_{\perp} A N \tag{6.13}$$

where $v_{\perp}$ is the component of velocity normal to the beam and N is the number density of fish (fish m^{-3}). Multiplying Equation 6.13 by the observation interval in seconds (equal in this case to the pulse length T) will give the number of fish per ping F_{ping}:

$$F_{ping} = v_{\perp} A N T \tag{6.14}$$

Multiplying the result of Equation 6.14 by the pulse repetition frequency (PRF, pings s^{-1}) will result in the number of fish observed per unit time F_{time} with the given geometry and PRF:

$$F_{time} = v_{\perp} A N T \times PRF \tag{6.15}$$

The maximum PRF is related to the maximum range R_{max}: it is the inverse of the time taken for a pair of pulses to return from the farthest range bin of interest:

$$(PRF)_{max} = \frac{c}{2R_{max}} \tag{6.16}$$

Substitution of 6.16 into Equation 6.15 results in the following expression for the number of fish observed per unit time:

$$F_{time} = \frac{v_{\perp} N T c}{2R_{max}} A \tag{6.17}$$

Any one beam has a cross-sectional area A of a triangle, related to the beam angle ϕ of the beam by

$$A = \frac{1}{2} R_{max}^2 \tan \frac{\phi}{2} \tag{6.18}$$

Substitution of Equation 6.18 into Equation 6.17 results in the probability per unit time of observing a fish in a single beam:

$$F_{time} = \frac{v_\perp NTc}{4} R_{max} \tan \frac{\phi}{2} \tag{6.19}$$

The only parameter in Equation 6.19 which is directly under the user's control is the pulse length T; the maximum range R_{max} is determined by the transmit frequency as well as other environmental factors (e. g. absorption, boundary reverberation, refraction), and the beam angle is determined by the transducer size, both of which are fixed once an instrument is chosen. Application of Equation 6.19 will require typical values for the parameters: velocity $v_\perp = 50$ cm s^{-1}, pulse length $T = 100$ μs, $c = 1500$ m s^{-1}, $R_{max} = 70$ m (transmit frequency of 250 kHz), $\phi = 4 - 6°$. The number of fish observed per second F_{time} is plotted as a function of fish density N in Figure 6.9. Realistic values for N for schooling fish are 1–10 fish m^{-3}, based on observations of migrating Atlantic cod (Rose, 1993) and Atlantic herring (Trevorrow and Claytor, 1998). The region above the dotted line in Figure 6.9 indicates the values of F_{time} of 0.1–1 fish s^{-1} resulting from the observed fish densities of 1–10 fish m^{-3}.

The uncertainty in a single fish velocity measurement is between 4–11% (Section 6.2.1). Recall that the component of uncertainty arising from δ_v is, on average, equal to zero; therefore, it would be expected that averaging velocities of several fish would tend to cancel out opposing signs of δ_v, reducing the overall uncertainty.

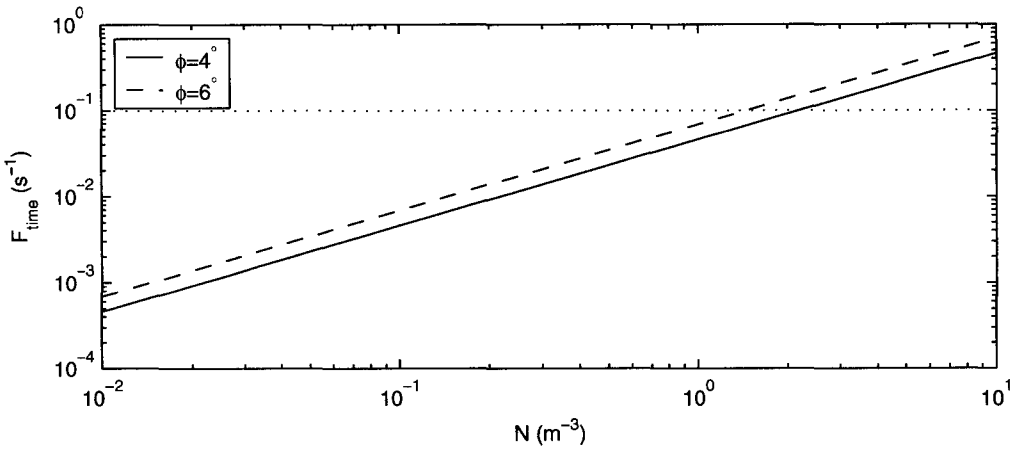

Figure 6.9: Plot of observed fish per unit time F_{time} (s^{-1}) as a function of fish density N (m^{-3}) for beamwidths of 4° (solid line) and 6° (dashed line). The dotted line corresponds to $F_{time} = 0.1$ s^{-1}.

If an uncertainty of less than 1% is desired, 100 fish would need to be observed, which translates to an averaging time of approximately 1.5–17 minutes if $F_{time} = 0.1 - 1$ fish s^{-1}. If fish were an order of magnitude more widely-spaced (0.1 fish m^{-3}), as might be expected for non-schooling fish, the averaging time for 100 fish would increase to nearly 3 hours.

Therefore, a 'reasonable' value for the observed fish per unit time F_{time} will depend on a number of factors in addition to the fish density: how long the fish motion is expected to be constant, how long the total observation time is expected to be, and how much fish-to-fish variation in velocity is expected. For example, diurnally migrating fish might be expected to have constant behaviour during daylight hours, but if behaviour is governed by semi-diurnal tides, their motion will vary on a scale of a few hours. A resident species would be available for observation year-round, while a migrating species might be present for several weeks. Milling fish will have

less uniform velocities than migrating fish, and increased averaging time would not reduce the variation in fish velocities. A range of realistic fish densities has resulted in a corresponding range of observation rates which could provide useful velocity data. The particulars of a given experiment would ultimately determine whether acceptable measurements could be made.

6.2.4 Sonar parameters

Pulse length, lag, transmit frequency, and bandwidth are among the sonar parameters that will affect fish velocity measurement. Long pulses reduce spatial resolution, but result in a higher probability of fish detection and more velocity samples from an individual fish. Long lags result in lower values of the standard deviation but risk velocity aliasing through the reduced ambiguity velocity. Lower transmit frequencies result in greater maximum range but higher standard deviations (recall Equation 2.32) and a reduced ability to detect smaller fish. Higher bandwidth allows for more samples on a particular fish and increased averaging to improve estimates of the complex correlation coefficient, which in turn can be used for target discrimination.

The pulse lengths used in the experiments ranged from 96–416 μs (7–31 cm) and were sufficient to identify fish between 30 cm and 60 cm in length in some very noisy environments. A final choice of pulse length would have to depend on expected fish density, as longer pulse lengths risk blurring together closely-spaced fish. In the context of the test instrument, pulse lengths shorter than 96 μs are not recommended, since the limited bandwidth results in a smaller peak power at very short pulse lengths. However, an instrument with wider bandwidth than 10 kHz would be capable of shorter pulses if desired and would also allow for the use of coded

pulses to assist in target discrimination.

The lags used in the experiments ranged from 576–3168 μs ($\Delta v = 47 - 261$ cm s^{-1} for a transmit frequency of 250 kHz). The data acquired with longer lags suffered from velocity aliasing in the Fraser River experiments, where the fish were swimming faster than the ambiguity velocity and directly along the beam direction. Although velocity aliasing is easy to identify in coherent Doppler data, it is difficult to de-alias the data with good results. The longer lags would provide better data if a reliable anti-aliasing scheme were developed. In the absence of such a scheme, it would be best to choose a lag with an ambiguity velocity Δv larger than the highest expected fish speed. Assuming a transmit frequency of 250 kHz, a lag of 1–2 ms is a good choice, resulting in a Δv of 75–150 cm s^{-1}. The final choice would depend on geometry and expected fish behaviour, since fish swimming fast and directly along the beam direction would be more likely to have aliased velocities at the longer lags. Furthermore, if the fish were being observed from a vertical perspective close to the bottom or surface, the choice of lag would affect how far from the boundary the fish must be to obtain a good measurement of its velocity. Measurements made within one lag of the boundary will not produce useful velocity estimates.

A bandwidth of 16% or greater (relative to the transmit frequency) is required to allow for phase coding and increased averaging along the pulse length, which would improve estimates of both velocity and the complex correlation coefficient (for target discrimination); however, a truly broadband instrument (bandwidth of 50%) is not necessary. The bandwidth of the test instrument (4%) is insufficient for a stand-alone system, primarily because it does not offer sufficient discrimination between water and fish for automated target identification, although Doppler velocity estimates were

acceptable.

A transmit frequency between 200–300 kHz would allow for a maximum range of 60–90 m, with standard deviations $\sigma_v = 3$ cm s^{-1} if the lags are chosen so that the ambiguity velocity $\Delta v = 75$ cm s^{-1}. One might consider decreasing the transmit frequency in order to increase range, but the standard deviation σ_v depends inversely on frequency. For example, halving the frequency would double the observed standard deviation σ_v, and require 4 times as much averaging to obtain velocity estimates of equivalent quality. On the other hand, increasing the frequency would decrease the maximum range of the instrument. Therefore, it appears that a transmit frequency of between 200-300 kHz is a good balance between minimizing σ_v and maximizing range. In fact, the test system, with a transmit frequency of 250 kHz, has worked well to obtain Doppler velocities from fish ranging from 30-cm cod to 60-cm salmon at ranges as large as 70 m.

In order to make a truly effective stand-alone system, it would be necessary to find a reliable method of target discrimination. A bandwidth of 40 kHz and the use of coded pulses would allow for automated discrimination of water and fish targets. For a long-term deployment, it would be preferable not to store every data point with the intention of analyzing it in a post-processing stage, but rather have the system do some on-board processing, which would reduce storage requirements to tens of bytes of storage per fish rather than hundreds of bytes per fish and thousands of bytes which are ultimately discarded because they correspond to samples of water velocity. Doppler processing of water velocity could also take place on-board, with pulses more suited to water velocity estimation interleaved with the fish-finding pulses, again eliminating the need to store all the raw data.

Parameter	Value
Transmit frequency	200 – 300 kHz
Bandwidth	16% of transmit frequency
Expected maximum range	60 – 90 m
Maximum ping rate	8 – 12 Hz
Beam geometry (open-ocean)	Four beams (Janus configuration)
Beam angle with vertical	20–30°
Beam geometry (riverine)	Two beams
Angle between beams	40–60°
Beam width (–3 dB)	4–6°
Pulse length	100–500 μs
Pulse coding	Barker or other phase code
Ambiguity velocity	0.75–1.5 m s^{-1}
Lag	Based on ambiguity velocity
Other	On-board storage
	Fish detection algorithm
	Water velocity calculation

Table 6.1: Summary of suggested sonar parameters for implementation of Doppler sonar fish velocity measurement.

6.3 Summary of recommendations

A number of recommendations for Doppler sonar system specifications have arisen from the experimental, model, and theoretical results. The recommendations are explained in detail in Sections 6.2.2, 6.2.3, 6.2.4, and are summarized in Table 6.1.

A transmit frequency of 200–300 kHz would result in a measurement range of 60–90 m. For riverine measurements, the sonar could be arranged looking horizontally with two beams separated by 40–60°, while for an open-ocean application, four beams could be used in a Janus configuration with angles of 20–30° from the vertical. Pulse lengths of 100–500 μs would allow for measurements on fish of length 7.5 cm or greater. The expected maximum swimming velocity would assist in determining the lag, and the lag and aiming direction would determine how close to a boundary

successful measurements could be made. For long-term moored deployments, on-board storage and processing must be considered, and water velocity calculation would be necessary to determine fish velocity relative to water. A coherent Doppler sonar system designed with the specifications outlined in Table 6.1 should be able to make useful and accurate measurements of fish swimming velocity in realistic conditions.

Chapter 7

Conclusions

The advantages and limitations of coherent Doppler sonar techniques applied to measurements of fish swimming velocity have been investigated through examination of experimental, model, and theoretical results. The quality of Doppler velocity estimates was assessed by evaluating the error and the standard deviation, using a range of sonar parameters and environmental conditions likely to be encountered during real-life measurements. Experiments were performed using a purpose-made coherent sonar with a transmit frequency of 250 kHz and a bandwidth of 10 kHz. Two types of experiments were performed: towtank tests with styrofoam balls simulating fish targets, and field and laboratory trials with live, free-swimming fish. A computer model was developed to simulate the operation of a coherent Doppler sonar, and was used to confirm and extend experimental results. Experimental and model results were compared to theoretical predictions to test the validity of the underlying theoretical model. Finally, the results were synthesized to suggest ranges of parameters suitable for designing a Doppler sonar system capable of making useful measurements of fish

velocity.

Velocity calculation using a coherent Doppler sonar consists of the transmission of two closely spaced pulses separated by a lag, followed by collection of backscatter intensity and phase information. The Doppler frequency shift is estimated from the phase difference between the two backscattered pulses. The pair of pulses introduces a fundamental limit on the maximum velocity which can be measured, known as the ambiguity velocity, which depends inversely on the lag and the transmit frequency. Furthermore, the single-ping standard deviation in a Doppler velocity estimate depends inversely on both the lag and the transmit frequency. The combination of the dependence of ambiguity velocity and standard deviation on the lag and the transmit frequency is the source of a fundamental trade-off when using coherent sonar techniques: increasing the lag reduces the standard deviation but correspondingly lowers the ambiguity velocity, and vice versa. Therefore, one key consideration is an appropriate choice of lag and transmit frequency.

Sonar spatial resolution is limited by the minimum spatial sampling interval of the sonar. Experimental results showed that resolution equal to the sampling interval was achievable for transmit pulses comparable in length to the sampling interval.

The effects of lag, pulse length, pulse coding, target velocity, water velocity, SNR, and complex correlation coefficient on error and standard deviation were investigated using experimental and model results. The error did not depend strongly on any of the experimental or sonar parameters. The average error for the all targets observed in the experiments was 0.01 ± 0.02 cm s^{-1}, and the average magnitude of the error was 2.21 ± 0.02 cm s^{-1}.

The standard deviation depended inversely on lag, as predicted by theoretical

results. Agreement of experimental standard deviation with model results and theoretical predictions was within ± 1 cm s^{-1} when SNR was greater than 15 dB. However, the experimental standard deviation was up to a factor of 2 smaller than either the modelled or the predicted standard deviation when the SNR was less than 15 dB. The disagreement suggested that neither the model nor the theory accurately reflected the real-life low-SNR environment.

The experimental standard deviation did not depend on pulse length or pulse coding, although the modelled standard deviation nearly doubled from 2.7 cm s^{-1} to 4.5 cm s^{-1} over the same range of pulse lengths (96–416 μs, with a lag of 1152 μs). Modelled standard deviations from coded pulses were 1–2 cm s^{-1} higher than those from uncoded pulses of the same length, again inconsistent with experimental results. The reason for the discrepancies between the model and experimental behaviour of standard deviation as a function of pulse length is not clear. It is possible that additional sources of uncertainty in the experiment (e.g. tank reverberation, surface and bottom reflections, electronic noise) obscured the dependence of standard deviation on pulse length and coding that was demonstrated with the model.

The experimental standard deviation did not depend on target velocity for styrofoam targets, but it did depend on fish swimming speed. Coherent sonar model results, combined with a theoretical model of fish motion about its centre of mass, suggest that the increase in standard deviation with fish swimming speed was caused by the spectral spread in backscattered frequencies introduced by a target which experiences motion about its centre of mass.

Standard deviation depended on the absolute difference between the water and target velocities, increasing from a minimum of 2.5 cm s^{-1} to 4.8 cm s^{-1} (for a lag of

1152 μs) when the difference between target and water velocities was 100 cm s^{-1}. The target velocity measurement is 'contaminated' by water velocities when the difference between the two velocities is large: a wider range of phase shifts (upon which the velocity measurements depend) is observed when a wider range of target velocities is present, and the result is an increase in the fish velocity standard deviation.

The average single-ping standard deviation ranged between 5–13 cm s^{-1} for lags between 576–2304 μs (ambiguity velocities between 64–257 cm s^{-1}). However, with an average of 89 velocity samples per fish, the uncertainty in the mean velocity for an individual fish is equal to the standard deviation multiplied by a factor of $1/\sqrt{89} \approx 0.1$. The resulting uncertainty in the mean Doppler velocity after averaging will be between 0.5–1.4 cm s^{-1}. Assuming a 30-cm s^{-1} typical fish velocity and combining the typical error and standard deviation results in overall uncertainties between 2.5–3.4 cm s^{-1} or 8–11%. In order to further reduce the velocity uncertainty (to less than 1%), it would be necessary to observed 50–100 fish whose motions are expected to be relatively uniform.

The computer model allowed for investigation of the consequences of increasing the sonar bandwidth, which was not possible with the test instrument. Increasing the sonar bandwidth from 4% to 50% of the transmit frequency resulted in approximately constant uncertainty in Doppler velocity estimates. However, increased averaging at higher bandwidths results in significantly improved estimates of the complex correlation coefficient ρ for bandwidths greater than 16%. The improved estimates of ρ resulted in a greater ability to distinguish fish from water based on ρ alone, an important capability for automated target identification. By comparion, the 4% bandwidth of the test instrument resulted in complex correlation coefficients for water and fish

which were nearly identical, and it was not possible to identify targets solely through image processing.

Following the examination of experimental, model, and theoretical results, a set of system specifications was proposed which should allow for useful measurements of fish velocity in the field. A Doppler sonar for fish velocity measurement should have a transmit frequency of 200–300 kHz with at least a 16% bandwidth, which would result in a maximum range of 60–90 m and maximum ping rates of 8–12 Hz. Four relatively narrow beams (4–6°) in the Janus configuration (as in ADCPs), at an angle of 20–30° to the vertical, would provide measurements of all three independent components of fish velocity. Pulse length should be between 100–500 μs (7.5–37.5 cm), depending on expected fish spacing and size. The lag should be chosen to result in an ambiguity velocity Δv of 0.75–1.5 m s^{-1}, which would allow for measurement of 'typical' fish velocities without velocity aliasing. An instrument designed for long-term deployment would have to take into account efficient methods for on-board storage of data, and possibly for real-time calculations of both fish velocity and water velocity, to reduce the amount of space needed for data storage. An instrument designed with these specifications should be capable of velocity measurements with typical uncertainties of 2–4 cm s^{-1}, which would be correspondingly reduced by averaging velocity measurements for multiple fish.

7.1 Suggestions for future work

Future work is needed in three areas: signal processing, field testing, and model extension. A new instrument is necessary with specifications which conform to those

suggested in Section 6.3: a transmit frequency of 200–300 kHz, bandwidth of at least 16%, beam width of 4–6°, the flexibility to independently control sonar parameters (lag, pulse length and coding, pulse repetition frequency), and access to the raw sampled intensity and phase data for later analysis. In particular, the new instrument needs to have multiple beams to begin investigations of three-dimensional velocity measurements and the associated implied assumptions.

Improvements in signal processing would centre around the development of truly automated target discrimination routines, and the development of a robust anti-aliasing scheme. Target discrimination is not a trivial problem. The fisheries acoustics community approaches target discrimination on a ping-to-ping basis: if a ping contains a target satisfying certain strength and shape conditions, the next ping is examined for a similar signal 'near' the range at which the first signal was observed. The target discrimination method used in this thesis was to treat the backscatter time-series as images, and apply image-processing techniques to locate fish in the backscatter. This approach has been suggested before in fisheries acoustics (Balk and Lindem, 2000) but has not seen much use. The image-processing approach used in this project worked extremely well although it is substantially different from the approach favoured by the fisheries acoustics community; however, it needs further refinement and testing before it could be reliably used on a stand-alone system. The addition of a robust anti-aliasing scheme would allow for longer lags to be used, resulting in smaller values of the standard deviation for a given frequency.

With a multiple-beam instrument, it would be possible to make three-dimensional velocity measurements. Open-ocean observations of migrating fish schools would be the next logical step to follow the Fraser River field work which was done during the

salmon migration. An instrument with on-board storage could make measurements of long-term fish traffic through a particular area; careful choice of deployment location could provide interesting results. Even without on-board storage, a deployment of a few days or a week in a strategically chosen location observing fish with well-known behavioural patterns, such as the annual herring migration observed off the coast of Norway by Zedel et al. (2000), would provide an interesting dataset. A separate experiment in which individual fish are observed by two independent methods, similar to the silo tank experiment, would provide additional confirmation of the accuracy of the Doppler technique for estimating individual fish swimming velocity. It is necessary to keep in mind that any method of fish velocity measurement is subject have its own sources of uncertainty.

Two particular aspects of the model would be of interest for further investigation. The original model design consisted of a one-dimensional model with point targets. The additional effects of a beam pattern, as well as targets with internal structure, should provide a closer reproduction of the signal observed by a real instrument, and possibly provide more insight into instrument and model results.

Bibliography

Ahn, B. Y. and Park, S. B. (1991). Estimation of mean frequency of variance of ultrasonic Doppler signal by using second-order autoregressive model. *IEEE Transactions on Ultrasonics, Ferroelectrics, and Frequency Control*, 38:172–182.

Bainbridge, R. (1958). The speed of swimming fish as related to size and to the frequency and amplitude of the tail beat. *Journal of Experimental Biology*, 35:109–133.

Balk, H. and Lindem, T. (2000). Improved fish detection in data from split-beam sonar. *Aquatic Living Resources*, 13:297–303.

Barber, W. D., Eberhard, J. W., and Karr, S. G. (1985). A new time domain technique for velocity measurements using Doppler ultrasound. *IEEE Transactions on Biomedical Engineering*, BME-32:213–229.

Benoit-Bird, K. J. and Au, W. W. L. (2002). Dynamics of the Hawaiian mesopelagic boundary community studied with active acoustic moorings. In *ICES Symposium on Acoustics in Fisheries and Aquatic Sciences*, Montpellier, France.

Bradley, S. E., Deines, K. L., and Rowe, F. D. (1991). Acoustic correlation current profiler. *IEEE Journal of Oceanic Engineering*, 16(4):408–414.

Brumley, B. H., Cabrera, R. G., Deines, K. L., and Terray, E. A. (1990). Performance of a broadband aoucstics Doppler current profiler. In *Proceedings of the IEEE Fourth Working Conference on Current Measurement*, pages 283–289, New York. IEEE Press.

Brumley, B. H., Cabrera, R. G., Deines, K. L., and Terray, E. A. (1991). Performance of a broad-band acoustic Doppler current profiler. *IEEE Journal of Oceanic Engineering*, 16(4):402–407.

Brumley, B. H., Heuchling, P. R., Koehler, R. L., and Terray, E. A. (1987). Coded pulse-coherent Doppler sonar. In *IEEE Oceans '87 Proceedings*, pages 89–92.

Bugnon, F. J. and Whitehouse, I. A. (1991). Acoustic Doppler current meter. *IEEE Journal of Oceanic Engineering*, OE-16(4):420–426.

Cabrera, R. G., Deines, K. L., Brumley, B. H., and Terray, E. A. (1987). Development of a practical coherent acoustic Doppler current profiler. In *IEEE Oceans '87 Proceedings*, pages 93–97.

Chapman, R. (2003). UNESCO sea water equation of state calculator. `http://ioc.unesco.org/oceanteacher/resourcekit/M3/Converters/SeaWaterEquationOfState/Sea%20Water%20Equation%20of%20State%20Calculator.htm`.

Demer, D. A., Barange, M., and Boyd, A. J. (2000). Measurements of three-dimensional fish school velocities with an acoustic Doppler current profiler. *Fisheries Research*, 47:201–214.

Farnett, E. and Stevens, G. H. (1990). Pulse compression radar. In Skolnik, M. I., editor, *Radar Handbook*, pages 10.15–10.19. McGraw-Hill Book Company, New York.

Foster, S. G., Embree, P. M., and O'Brien Jr., W. D. (1990). Flow velocity profile via time-domain correlation: Error analysis and computer simulation. *IEEE Transactions on Ultrasonics, Ferroelectrics, and Frequency Control*, 37(2):164–175.

Freitag, H. P., McPhaden, M. J., and Pullen, P. E. (1992). Fish-induced bias in acoustic Doppler current profiler data. In *IEEE Oceans '92 Proceedings*, pages 112–117.

Hansen, D. S. (1986). Oceanic incoherent Doppler sonar spectral analysis by conventional and finite-parameter modeling methods. *IEEE Journal of Oceanic Engineering*, OE-11(1):26–41.

Hendershot, R. G., Acker, W. C., and Sullivan, R. (1984). Doppler techniques applied to fisheries hydroacoustics. In *IEEE Oceans '84 Proceedings*, pages 15–20.

Hester, F. J. (1967). Identification of biological sonar targets from body motion Doppler shifts. In Tavolga, W. N., editor, *Symposium on Marine Bioacoustics, Vol. 2*, pages 59–74, New York. Pergamon Press.

Holliday, D. V. (1974). Doppler structure in echoes from schools of pelagic fish. *The Journal of the Acoustical Society of America*, 55:1313–1322.

Holliday, D. V. (1977). Two applications of the Doppler effect in the study of fish schools. *Rapports et Procès-Verbaux des Réunions, Conseil International pour l'Exploration de la Mer*, 170:21–30.

Johnston, S. V. and Hopelain, J. S. (1990). The application of dual-beam target tracking and Doppler-shifted echo processing to assess upstream salmonid migration in the Klamath river, California. *Rapports et Procès-Verbaux des Réunions, Conseil International pour l'Exploration de la Mer*, 189:210–222.

Kieser, R., Mulligan, T., and Ehrenberg, J. (2000). Observation and explanation of systematic split-beam angle measurement errors. *Aquatic Living Resources*, 13(5):275–281.

Lagö, T. L. (1999). *A novel signal model and estimation method for acoustic Doppler current meters.* PhD thesis, Lund University.

Levin, M. J. (1965). Power spectrum parameter estimation. *IEEE Transactions on Information Theory*, 11:100–107.

Lhermitte, L. and Serafin, R. (1984). Pulse-to-pulse coherent Doppler signal processing techniques. *Journal of Atmospheric and Oceanic Technology*, 1:293–308.

Lhermitte, R. (1983). Doppler sonar observation of tidal flow. *Journal of Geophysical Research*, 88(C1):725–742.

Lhermitte, R. and Lemmin, U. (1990). Probing water turbulence by high frequency Doppler sonar. *Geophysical Research Letters*, 17(10):1549–1552.

Luengo, C. L., Rieger, B., van Ginkel, M., and van Vliet, L. J. (2003). DIPimage toolbox for Matlab, version 1.4.2. Pattern Recognition group, Faculty of Applied Physics, Delft University of Technology.

MacLennan, D. N. and Simmonds, E. J. (1992). *Fisheries Acoustics.* Chapman & Hall, New York.

Mason, R. L., Gunst, R. F., and Hess, J. L. (2003). *Statistical Design and Analysis of Experiments.* John Wiley & Sons, New Jersey.

Matlab (2002). Matlab, version 6.5.0.180913a Release 13. The Mathworks, Inc.

Medwin, H. and Clay, C. S. (1998). *Fundamentals of Acoustical Oceanography.* Academic Press, Toronto.

Miller, K. S. and Rochwarger, M. M. (1970a). Estimation of spectral moments of time series. *Biometrika*, 57(3):513–517.

Miller, K. S. and Rochwarger, M. M. (1970b). On estimating spectral moments in the presence of colored noise. *IEEE Transactions on Information Theory*, IT-16(3):303–309.

Miller, K. S. and Rochwarger, M. M. (1972). A covariance approach to spectral moment estimation. *IEEE Transactions on Information Theory*, IT-18(5):588–596.

Mullison, J., George, R., Huhta, C., and Cabrera, R. (1997). Testing and deployment of a new acoustic Doppler current meter. In *IEEE Oceans '97 Proceedings*, volume 1, pages 115–119.

Olsen, K., Angell, J., Pettersen, F., and Lø vik, A. (1983). Observed fish reactions to a surveying vessel with special reference to herring, cod, capelin, and polar cod. *FAO Fisheries Report*, 300:131–138.

Peretto, L., Pasini, G., and Muscas, C. (2001). Signal spectrum analysis and period estimation by using delayed signal sampling. *IEEE Transactions on Instrumentation and Measurement*, 50(4):920–925.

Pincock, D. G. and Easton, N. W. (1978). The feasibility of Doppler sonar fish counting. *IEEE Journal of Oceanic Engineering*, OE-3:37–40.

Pinkel, R. (1986). Doppler sonar measurements of ocean waves and currents. *Marine Technical Society Journal*, 20:58–67.

Pinkel, R., Plueddemann, A., and Williams, R. (1987). Internal wave observations from FLIP in MILDEX. *Journal of Physical Oceanography*, 17:1737–1757.

Pinkel, R. and Smith, J. A. (1987). Open ocean surface wave measurement using Doppler sonar. *Journal of Geophysical Research*, 92(C12):12967–12973.

Pinkel, R. and Smith, J. A. (1992). Repeat-sequence coding for improved precision of Doppler sonar and sodar. *Journal of Atmospheric and Oceanic Technology*, 9:149–163.

Plimpton, P. E., Freitag, H. P., and McPhaden, M. J. (1997). ADCP velocity errors from pelagic fish schooling around equatorial moorings. *Journal of Atmospheric and Oceanic Technology*, 14:1212–1223.

Plueddemann, A. J. and Pinkel, R. (1989). Characterization of the patterns of diel migrations using a doppler sonar. *Deep-Sea Research, Part A*, 36:509–530.

Rickey, D. W. (2000). Medical ultrasound course notes. University of Manitoba, Winnipeg, Manitoba.

Rose, G. A. (1993). Cod spawning on a migration highway in the north-west Atlantic. *Nature*, 366:458–461.

Rowe, F. D., Deines, K. L., and Gordon, R. L. (1986). High resolution current profiler. In Appell, G. F. and Woodward, W. E., editors, *Proceedings of the IEEE Third Working Conference on Current Measurement*, pages 184–189, New York. IEEE Press.

Ryan, S., Department of Fisheries and Oceans, The Evening Telegram, NFFAUW, Human Resources Development Canada, and DataDisk Inc. (1996). Cod migration.
ttfamily http://www.cdli.ca/cod/codmig.htm.

Sachidananda, M. and Zrnić, D. S. (2000). Clutter filtering and spectral moment estimation for Doppler weather radars using staggered pulse repetition time (PRT). *Journal of Atmospheric and Oceanic Technology*, 17(3):323–331.

Seim, H. E., Gregg, M. C., and Miyamoto, R. T. (1995). Acoustic backscatter from turbulent microstructure. *Journal of Atmospheric and Oceanic Technology*, 12:376–380.

Sirmans, D. and Doviak, R. J. (1973). Pulsed-Doppler velocity isotach displays of storm winds in real time. *Journal of Applied Meteorology*, 12:694–697.

Slotte, A., Hansen, K., Dalen, J., and Ona, E. (2002). Acoustic mapping of pelagic fish distribution and density in relation to a seismic shooting area off the Norwegian west coast. In *ICES Symposium on Acoustics in Fisheries and Aquatic Sciences*, Montpellier, France.

Smith, J. (1989). Doppler sonar and surface waves: Range and resolution. *Journal of Atmospheric and Oceanic Technology*, 6:680–696.

Sutton, D. W. and Jaffe, J. S. (1992). Acoustic bedload velocity estimates using a broadband pulse-pulse time correlation technique. *Journal of the Acoustical Society of America*, 92(3):1692–1698.

Theriault, K. B. (1986). Incoherent multibeam Doppler current profiler performance: Part I - estimate variance. *IEEE Journal of Oceanic Engineering*, OE-11:7–15.

Trevorrow, M. and Claytor, R. R. (1998). Detection of Atlantic herring *Clupea harengus* schools in shallow waters using high-frequency sidescan sonars. *Canadian Journal of Fisheries and Aquatic Sciences*, pages 1419–1429.

Trevorrow, M. V. and Farmer, D. M. (1992). The use of Barker codes in Doppler sonar measurements. *Journal of Atmospheric and Oceanic Technology*, 9:699–704.

Trevorrow, M. V. and Teichrob, R. C. (1994). Self-contained acoustics platforms for probing ocean surface processes. *IEEE Journal of Oceanic Engineering*, 19(3):483–492.

Wadsworth Jr., H. M., editor (1990). *Handbook of Statistical Methods for Engineers and Scientists.* McGraw-Hill, Toronto.

Waite, J. W. and Belcher, E. O. (1985). Sonar detection of riverine fish using the pulse pair covariance Doppler frequency estimator. In *IEEE Oceans '85 Proceedings*, pages 700–706.

Wilson, C. D. and Firing, E. (1992). Sunrise swimmers bias acoustic Doppler current profiles. *Deep-Sea Research*, 39:885–892.

Wilson Jr., T. C., Lwiza, K. M. M., and Allen, G. L. (1997). Performance comparison of RDI ADCPs broadband versus narrowband. In *IEEE Oceans '97 Proceedings*, volume 1, pages 120–125.

Xie, Y., Cronkite, G., and Mulligan, T. J. (1997). A split-beam echosounder perspective on migratory salmon in the Fraser River: a progress report on the split-beam experiment at Mission, B. C., in 1995. Techical Report 8, Pacific Salmon Commission.

Xie, Y., Mulligan, T. J., Cronkite, G. M. W., and Gray, A. P. (2002). Assessment of potential bias in hydroacoustic estimation of Fraser River sockeye and pink salmon at Mission, B. C. Techical Report 11, Pacific Salmon Commission.

Zedel, L., Cabrera, R., Lohrmann, A., and Hay, A. (1995). Single beam, high resolution pulse-to-pulse coherent Doppler profiler. In Anderson, S. P., Appell, G. F., and Williams III, A. J., editors, *Proceedings of the IEEE Fifth Working Conference on Current Measurement*, pages 199–204. William S. Sullwood Publishing.

Zedel, L. and Hay, A. E. (1999). A coherent Doppler profiler for high-resolution particle velocimetry in the ocean: Laboratory measurements of turbulence and particle flux. *Journal of Atmospheric and Oceanic Technology*, 16:1102–1117.

Zedel, L., Hay, A. E., Cabrera, R., and Lohrmann, A. (1996). Performance of a single beam, pulse-to-pulse coherent Doppler profiler. *IEEE Journal of Oceanic Engineering*, 21(3):290–297.

Zedel, L. and Knutsen, T. (2000). Measurement of fish velocity using Doppler sonar. In *IEEE Oceans 2000 Proceedings*, volume 3, pages 1951–1956.

Zedel, L., Knutsen, T., and Patro, R. (2003). Acoustic Doppler current profiler observations of herring movement. *ICES Journal of Marine Science*, 60:846–859.

Ziomek, C. D. (2002). *Specifications for the NI PXI/PCI-5411/5431.* National Instruments and ZTEC, Inc. Appendix: Techniques in digital communication.

Zrnic, D. S. (1977). Spectral moment estimates from correlated pulse pairs. *IEEE Transactions on Aerospace and Electronic Systems*, AES-13:344–354.

Appendix A

A.1 Target identification parameters

Speed of sound in all cases was calculated using measured temperature, salinity of 0 PSU for fresh water and measured PSU for salt water, depth of 0 m, and the UNESCO speed of sound calculator available on the World Wide Web (Chapman, 2003).

Intensity thresholds will seem inconsistent due to the fact that in some experiments, a background profile was subtracted to reduce the effect of surface or bottom sidelobes.

A.1.1 Target-array experiment (IOT, 2001)

Group name	Tank position (m)	Target sizes (cm)	Target spacing (cm)	Angle
A	50	3 × 2.5	5	45°
B	52	3 × 2.5	10	45°
C	54	3 × 2.5	20	45°
D	56	3 × 2.5	40	45°
E	58	3 × 2.5	60	45°
F	62	3 × 7.6	20	45°
G	64	3 × 7.6	40	45°
H	66	3 × 7.6	60	45°
I	68	3 × 10.2	20	45°
J	70	3 × 10.2	40	45°
K	72	3 × 10.2	60	45°
L	74	7.6, 2.5, 10.2	10	45°
M	76	7.6, 2.5, 10.2	15	45°
N	78	7.6, 2.5, 10.2	20	45°
O	82	7.6, 2.5, 10.2	40	45°
P	84	7.6, 2.5, 10.2	60	45°
Q	86	10.2, 7.6, 2.5	40	45°
R	88	2.5, 7.6, 10.2	40	45°
T	92	4 × 2.5	10	0°
U	94	4 × 2.5	15	0°
V	96	4 × 2.5	20	0°
W	98	4 × 2.5	40	0°
X	102	3 × 5.1	10	45°
Y	104	3 × 5.1	30	45°
Z	106	3 × 12.7	20	45°
AA	108	3 × 12.7	30	45°

Table A.1: Position, size, spacing, and angle relative to tank bottom, for styrofoam targets used in the target-array experiment

Lag (μs)	Δv (cm s^{-1})	Pulse length (μs)	Pulse code	Group name
768	193	96	+ + −	IOT01D
		160	+ + + − +	IOT01E
		224	+ + + − − + −	IOT01F
		352	+ + + − − − + − − + −	IOT01G
		416	+ + + + + − − + + − + − +	IOT01H
1632	91	128	+ + −+	IOT01A
2400	62	128	+ + −+	IOT01B
3168	47	128	+ + −+	IOT01C

Table A.2: Lags, ambiguity velocities Δv, pulse lengths, and pulse codes used in the target-array experiment.

Parameter	Value
Connectivity	2
Maximum target size	no limit
Minimum target size	10 samples
Correlation threshold	0.9
Intensity threshold	70 dB
Gaussian filter sigma	no filter used
Speed of sound	1485 m s^{-1}
Definition of velocity outlier	more than $\pm 2\sigma_v$ from $\overline{v}$
Noise samples	samples between targets at the same range

Table A.3: Summary of target identification parameters for the target-array experiment.

A.1.2 Short-range experiment (OERC, 2003)

Tank position (m)	Target description	Diameter(s) (cm)
9	Ball	12.7
11	Ball	12.7
13	Ball	12.7
15	Ball	7.6
17	Ball	7.6
19	Ball	7.6
21	Ball	5.1
23	Ball	5.1
25	Ball	5.1
27	Ball	2.5
29	Ball	2.5
31	Ball	2.5
33	Egg	12.0 (large) 8.7 (small)
35	Egg	9.7 (large) 7.3 (small)

Table A.4: Position, shape, and size of styrofoam targets used in the short-range experiment.

Lag (μs)	Δv (cm s^{-1})	Pulse length (μs)	Pulse code	Group name
576	257	96	None	OERC03AT01
		96	+ + −	OERC03AT02
		224	None	OERC03AT03
		224	+ + + − − + −	OERC03AT04
		416	None	OERC03AT05
		416	+ + + + + − − + + − + − +	OERC03AT06
768	193	96	None	OERC03AR07
		96	+ + −	OERC03AR08
1152	129	96	None	OERC03AT07
		96	+ + −	OERC03AT08
		128	None	OERC03AR01
		128	+ + −+	OERC03AR02
		160	None	OERC03AR03
		160	+ + + − +	OERC03AR04
		224	None	OERC03AT09
		224	+ + + − − + −	OERC03AT10
		352	None	OERC03AR05
		352	+ + + − − − + − − + −	OERC03AR06
		416	None	OERC03AT11
		416	+ + + + + − − + + − + − +	OERC03AT12
1728	86	96	None	OERC03AR09
		96	+ + −	OERC03AR10
2304	64	96	None	OERC03AT13
		96	+ + −	OERC03AT14
		224	None	OERC03AT15
		224	+ + + − − + −	OERC03AT16
		416	None	OERC03AT17
		416	+ + + + + − − + + − + − +	OERC03AT18

Table A.5: Lags, ambiguity velocities Δv, pulse lengths, and pulse codes used in the short-range experiment.

Parameter	Value
Connectivity	2
Maximum target size	no limit
Minimum target size	no limit
Correlation threshold	0.9
Intensity threshold	80 dB
Gaussian filter sigma	no filter used
Speed of sound	1485 $\mathrm{m\,s^{-1}}$
Definition of velocity outlier	more than $\pm 2\sigma_v$ from $\overline{v}$
Noise samples	samples between targets at the same range

Table A.6: Summary of target identification parameters for the short-range experiment.

A.1.3 Long-range 1 experiment (OERC, 2003)

Tank position (m)	Target description	Diameter (cm)
29	Ball	2.5
31	Ball	5.1
33	Ball	7.6
35	Ball	12.7

Table A.7: Position, shape, and size of styrofoam targets used in the long-range 1 experiment.

Lag (μs)	Δv (cm s^{-1})	Pulse length (μs)	Pulse code	Group name
1152	129	96	None	OERC03BT19
		96	$++-$	OERC03BT20
		224	None	OERC03BT23
		224	$+++--+-$	OERC03BT24
		416	None	OERC03BT21
		416	$+++++--++-+-+$	OERC03BT22

Table A.8: Lags, ambiguity velocities Δv, pulse lengths, and pulse codes used in the long-range 1 experiment.

Parameter	Value
Connectivity	2
Maximum target size	no limit
Minimum target size	no limit
Correlation threshold	0.9
Intensity threshold	70 dB
Gaussian filter sigma	no filter used
Speed of sound	1485 m s^{-1}
Definition of velocity outlier	more than $\pm 2\sigma_v$ from $\overline{v}$
Noise samples	noise profile as a function of range

Table A.9: Summary of target identification parameters for the long-range 1 experiment.

A.1.4 Long-range 2 experiment (IOT, 2003)

Lag (μs)	Δv (cm s^{-1})	Pulse length (μs)	Pulse code	Group name
576	257	96	None	IOT03T01
		96	+ + −	IOT03T02
		224	None	IOT03T03
		224	+ + + − − + −	IOT03T04
		416	None	IOT03T05
		416	+ + + + + − − + + − + − +	IOT03T06
1152	129	96	None	IOT03T07
		96	+ + −	IOT03T08
		224	None	IOT03T09
		224	+ + + − − + −	IOT03T10
		416	None	IOT03T11
		416	+ + + + + − − + + − + − +	IOT03T12
2304	64	96	None	IOT03T13
		96	+ + −	IOT03T14
		224	None	IOT03T15
		224	+ + + − − + −	IOT03T16
		416	None	IOT03T17
		416	+ + + + + − − + + − + − +	IOT03T18

Table A.10: Lags, ambiguity velocities Δv, pulse lengths, and pulse codes used in the long-range 2 experiment.

Parameter	Value
Connectivity	2
Maximum target size	no limit
Minimum target size	10 samples
Correlation threshold	0.9
Intensity threshold	70 dB
Gaussian filter sigma	no filter used
Speed of sound	1480.8 m s^{-1}
Definition of velocity outlier	more than $\pm 2\sigma_v$ from $\overline{v}$
Noise samples	noise profile as a function of range

Table A.11: Summary of target identification parameters for the long-range 2 experiment.

A.1.5 Mobile field experiment (Fraser River, 2001)

Lag (μs)	Δv (cm s^{-1})	Pulse length μs	Pulse code	Number of fish	Group name
576	257	96	None	44	FR01F
		96	$++-$	15	FR01G
		224	None	7	FR01H
		224	$++-+--+-$	13	FR01I
		416	None	26	FR01J
		416	$+++++--++-+-+$	15	FR01K
1152	129	96	None	42	FR01A
		96	$++-$	3	FR01B
		224	None	1	FR01D
		224	$++-+--+-$	11	FR01E

Table A.12: Lags, ambiguity velocities Δv, pulse lengths, pulse codes, and number of fish identified in the mobile field experiment.

Parameter	Value
Connectivity	1
Maximum target size	no limit
Minimum Feret 2 diameter	3 pixels
Maximum Feret 2 diameter	20 pixels
Minimum ratio of Feret 1 to Feret 2	2
Minimum range extent	equal to pulse length
Minimum time in beam	2 s
Minimum target size	based on ninimum range and time
Correlation threshold	0.9
Intensity threshold	$\overline{I} + \sigma_I$
Gaussian filter sigma	no filter used
Speed of sound	1469 m s^{-1}
Definition of velocity outlier	more than $\pm 2\sigma_v$ from $\overline{v}$
Minimum number of samples per target	10
Noise samples	'box' around fish ± 3 samples in time and range

Table A.13: Summary of target identification parameters for the mobile field experiment.

A.1.6 Stationary field experiment (Fraser River, 2002)

Date	Time (PDT)	Heading
14 August	14:13	60°
19 August	13:00	32°
19 August	20:38	Sonar fell over
20 August	13:41	Sonar was righted and re-aimed to 32°
21 August	17:30	46°
22 August	17:30	52°

Table A.14: Summary of transducer heading and movement during the stationary field experiment.

Lag (μs)	Δv (cm s^{-1})	Pulse length μs	Pulse code	Number of fish	Group name
576	255	96	None	493	FR02A
		96	+ + −	485	FR02B
		224	None	500	FR02C
		224	+ + + − − + −	544	FR02D
		416	None	551	FR02E
		416	+ + + + + − − + + − + − +	557	FR02F
1152	128	96	None	546	FR02G
		96	+ + −	1056	FR02H
		224	None	546	FR02I
		224	+ + + − − + −	548	FR02J
		416	None	551	FR02K
		416	+ + + + + − − + + − + − +	548	FR02L
2304	64	96	None	476	FR02M
		96	+ + −	498	FR02N
		416	None	380	FR02Q
		416	+ + + + + − − + + − + − +	534	FR02R

Table A.15: Lags, ambiguity velocities Δv, pulse lengths, pulse codes, and number of fish identified in the stationary field experiment.

Parameter	Value
Connectivity	2
Maximum target size	no limit
Minimum Feret 2 diameter	1 pixels
Maximum Feret 2 diameter	10 pixels
Minimum ratio of Feret 1 to Feret 2	2
Minimum range extent	equal to pulse length
Minimum time in beam	2 s
Minimum target size	based on minimum range and time
Correlation threshold	0.9
Intensity threshold	$\overline{I} + \sigma_I$
Gaussian filter sigma	1.00 for pulses $\geq 224\mu$s
	0.75 for pulses $< 224\mu$s
Speed of sound	1471 m s^{-1}
Definition of velocity outlier	more than $\pm 2\sigma_v$ from $\overline{v}$
Minimum number of samples per target	10
Noise samples	'box' around fish ± 3 samples in time and range

Table A.16: Summary of target identification parameters for the stationary field experiment.

A.1.7 Silo tank experiment (OSC, 2003)

Parameter	Value
Connectivity	1
Maximum target size	no limit
Minimum target size	5 pixels
Correlation threshold	0.9
Intensity threshold	200 dB
Gaussian filter sigma	no filter used
Speed of sound	1505 $\mathrm{m\,s^{-1}}$
Definition of velocity outlier	more than $\pm 2\sigma_v$ from $\overline{v}$
Minimum number of samples per target	no limit
Noise samples	'box' around fish ± 3 samples in time and range

Table A.17: Summary of target identification parameters for the silo tank experiment.

A.2 Experimental linear fit parameters

A.2.1 Accuracy as a function of lag

$\delta_v = a_0 + a_1\tau$					
Experiment	a_0 (**cm s^{-1}**)	a_1 ($\times 10^{-6}$) (**cm s^{-1}/μs**)	**R**	**F**	**p** ($\alpha = 0.01$)
Target array	-0.03 ± 0.46	20 ± 210	0.051	0.107	0.77
Stationary field	0.1 ± 7.9	20 ± 5200	0.002	2.39×10^{-3}	0.97
Short-range	-0.3 ± 1.7	180 ± 1140	0.078	0.253	0.65
Long-range 2	-0.2 ± 1.6	40 ± 1040	0.200	0.249	0.71

Table A.18: Slope, intercept, linear correlation coefficient, F-value, and p-value for linear fits of δ_v as a function of lag.

A.2.2 Accuracy and precision as a function of tow velocity

$\delta_v = a_0 + a_1 v_{tow}$						
Experiment		a_0 (**cm s^{-1}**)	a_1 ($\times 10^{-3}$) (**cm s^{-1}/cm s^{-1}**)	**R**	**F**	**p** ($\alpha = 0.01$)
Target array		-0.1 ± 0.4	3 ± 8	0.050	0.738	0.40
Short-range		0.21 ± 0.09	19 ± 1	0.994	1220	4×10^{-9}
Long-range 1		0.3 ± 0.2	16 ± 3	0.972	208	7×10^{-6}
Long-range 2		-0.1 ± 0.2	15 ± 3	0.964	159	1×10^{-5}
$\sigma_v = a_0 + a_1 v_{tow}$						
Experiment	**Lag** (μs)	a_0 (**cm s^{-1}**)	a_1 ($\times 10^{-3}$) (**cm s^{-1}/cm s^{-1}**)	**R**	**F**	**p** ($\alpha = 0.01$)
Short-range	576	5.9 ± 2.0	2 ± 30	0.002	0.015	0.91
	1152	3.1 ± 0.7	6 ± 10	0.249	1.99	0.21
	2304	1.5 ± 1.9	40 ± 70	0.762	6.39	0.13
Long-range 1	1152	4.6 ± 0.3	5 ± 5	0.507	6.18	0.05
Long-range 2	576	11.4 ± 0.8	9 ± 12	0.354	3.29	0.12
	1152	5.7 ± 1.3	1 ± 20	0.004	0.026	0.88
	2304	3.1 ± 0.4	10 ± 20	0.884	15.2	0.06

Table A.19: Slope, intercept, linear correlation coefficient, F-value, and p-value for linear fits of δ_v and σ_v as a function of tow velocity.

A.2.3 Accuracy and precision as a function of fish velocity

$\delta_v = a_0 + a_1 v_{fish}$					
	a_0 (cm s^{-1})	a_1 (cm s^{-1}/cm s^{-1})	R	F	p ($\alpha = 0.01$)
	0.7 ± 0.7	0.01 ± 0.02	0.078	2.20	0.15
$\sigma_v = a_0 + a_1 \lvert v_{fish} \rvert$					
Lag (μs)	a_0 (cm s^{-1})	$a_1(\times 10^{-3})$ (cm s^{-1}/cm s^{-1})	R	F	p ($\alpha = 0.01$)
576	13 ± 2	230 ± 60	0.916	87.1	1×10^{-5}
1152	7.8 ± 0.6	90 ± 10	0.940	252	3×10^{-11}
2304	5.3 ± 0.6	80 ± 20	0.898	61.9	1×10^{-4}

Table A.20: Fit parameters for δ_v as a function of v_{fish} and σ_v as a function of $|v_{fish}|$ for the stationary field experiment.

A.2.4 Accuracy as a function of pulse length and coding

$\delta_v = a_0 + a_1 T$						
Experiment	Code?	a_0 (cm s^{-1})	$a_1(\times 10^{-3})$ (cm s^{-1}/μs)	R	F	p ($\alpha = 0.01$)
Target array	C	0.5 ± 0.5	-2 ± 2	0.776	13.8	0.02
Stationary field	NC	0.1 ± 9.1	-0.3 ± 33	0.011	0.01	0.93
	C	0.8 ± 3.1	-2 ± 11	0.859	6.11	0.25
Short-range	NC	-0.05 ± 1.88	-2 ± 7	0.074	0.32	0.60
	C	0.6 ± 0.7	-2 ± 3	0.505	4.07	0.11
Long-range 1	NC	0.3 ± 0.2	-0.1 ± 0.6	0.892	8.25	0.21
	C	0.6 ± 2.5	-1 ± 9	0.756	3.10	0.33
Long-range 2	NC	-0.1 ± 2.2	-0.3 ± 8.0	0.208	0.26	0.70
	C	0.2 ± 1.1	-1 ± 4	0.937	14.9	0.16

Table A.21: Slope, intercept, linear correlation coefficient, F-value, and p-value for linear fits of δ_v as a function of pulse length.

Experiment	**No code** $\delta_v \pm \sigma_{\delta_v}$ **(cm s^{-1})**	**Code** $\delta_v \pm \sigma_{\delta_v}$ **(cm s^{-1})**	$\lvert\delta_{vNC} - \delta_{vC}\rvert$ **(cm s^{-1})**	$\sigma_{NC,C}$ **(cm s^{-1})**	**Agree within** $\pm 2\sigma_{NC,C}$**?**
Stationary field	0.01 ± 0.07	0.35 ± 0.07	0.34	0.09	No
Short-range	-0.3 ± 0.3	0.08 ± 0.12	0.42	0.3	Yes
Long-range 1	0.30 ± 0.05	0.30 ± 0.05	0.003	0.07	Yes
Long-range 2	-0.19 ± 0.03	-0.13 ± 0.05	0.06	0.06	Yes

Table A.22: Mean values of $\delta_v \pm$ standard error σ_{δ_v}(cm s^{-1}) for uncoded (NC) and coded (C) pulses, absolute value of the difference, combined error $\sigma_{NC,C} = \sqrt{\sigma^2_{\delta_{vNC}} + \sigma^2_{\delta_{vC}}}$, and agreement.

A.2.5 Precision as a function of pulse length and coding

$\sigma_v = a_0 + a_1 T$							
Experiment	**Code?**	**Lag** (μs)	a_0 (cm s^{-1})	$a_1(\times 10^{-3})$ (cm s^{-1}/μs)	**R**	**F**	**p** ($\alpha = 0.01$)
Target array	C	768	4 ± 1	2 ± 5	0.378	1.82	0.27
Mobile field	C	576	7 ± 34	2 ± 121	0.063	0.07	0.84
Stationary field	NC	576	17 ± 12	-1 ± 44	0.109	0.12	0.79
	C	576	18 ± 4	-1 ± 13	0.582	1.39	0.45
	NC	1152	10 ± 1	-0.7 ± 5.0	0.742	2.87	0.34
	C	1152	11 ± 8	-4 ± 30	0.781	3.56	0.31
Short-range	NC	576	7 ± 6	-0.3 ± 22	0.033	0.03	0.89
	C	576	4 ± 5	2 ± 18	0.718	2.55	0.36
	NC	1152	2.0 ± 0.8	6 ± 3	0.868	26.2	7×10^{-3}
	C	1152	2.3 ± 0.3	1 ± 1	0.698	9.25	0.04
	NC	2304	0.2 ± 4.2	7 ± 15	0.974	38.1	0.10
	C	2304	1 ± 1	-0.04 ± 4.00	0.014	0.01	0.92
Long-range 1	NC	1152	4 ± 4	2 ± 15	0.756	3.11	0.33
	C	1152	4 ± 4	4 ± 15	0.903	9.27	0.20
Long-range 2	NC	576	6 ± 9	21 ± 33	0.986	68.0	0.08
	C	576	10 ± 4	9 ± 12	0.987	77.9	0.07
	NC	1152	3 ± 1	7 ± 4	0.998	470	0.03
	C	1152	9 ± 32	-10 ± 113	0.534	1.14	0.48
	NC	2304	2 ± 1	4 ± 5	0.991	108	0.06
	C	2304	2.5 ± 0.4	3 ± 1	0.998	529	0.03

Table A.23: Slope, intercept, linear correlation coefficient, F-value, and p-value for linear fits of σ_v as a function of pulse length.

Experiment	**Lag** (μs)	**No code** $\sigma_v \pm \sigma_{\sigma_v}$ (cm s^{-1})	**Code** $\sigma_v \pm \sigma_{\sigma_v}$ (cm s^{-1})	$\sigma_{vNC} - \sigma_{vC}$ (cm s^{-1})	$\sigma_{NC,C}$ (cm s^{-1})	**Agree within** $\pm 2\sigma_{NC,C}$?
Mobile field	576	10 ± 1	7.4 ± 0.7	2.6	1.2	Yes
	1152	5.9 ± 0.9	4.8 ± 0.5	1.1	1.2	Yes
Stationary field	576	16.6 ± 0.2	17.3 ± 0.2	-0.7	0.2	No
	1152	9.8 ± 0.1	10.18 ± 0.08	-0.4	0.1	No
	2304	6.6 ± 0.1	6.37 ± 0.07	0.2	0.1	Yes
Short-range	576	6.9 ± 0.7	4.8 ± 0.1	2.1	0.7	No
	768	3.5 ± 0.2	3.28 ± 0.07	0.2	0.2	Yes
	1152	3.4 ± 0.2	2.58 ± 0.04	0.8	0.2	No
	1728	1.8 ± 0.1	1.6 ± 0.1	0.1	0.1	Yes
	2304	2.1 ± 0.4	1.14 ± 0.03	1.0	0.4	No
Long-range 1	1152	4.5 ± 0.1	4.53 ± 0.09	-0.03	0.1	Yes
Long-range 2	576	11.3 ± 0.2	12.0 ± 0.2	-0.7	0.2	No
	1152	5.3 ± 0.1	6.9 ± 0.2	-1.6	0.1	No
	2304	2.96 ± 0.08	3.2 ± 0.1	-0.2	0.09	No

Table A.24: Mean values of $\sigma_v \pm$ standard error σ_{σ_v}(cm s^{-1}) for uncoded (NC) and coded (C) pulses, difference, combined error $\sigma_{NC,C} = \sqrt{\sigma^2_{\sigma_{vNC}} + \sigma^2_{\sigma_{vC}}}$, and agreement.

A.2.6 Accuracy as a function of range

$\delta_v = a_0 + a_1 R$					
Experiment	$\mathbf{a_0}$ $(\mathbf{cm\,s^{-1}})$	$\mathbf{a_1}$ $(\mathbf{cm\,s^{-1}/m})$	**R**	**F**	**p** $(\alpha = 0.01)$
Stationary field	0.004 ± 0.323	0.009 ± 0.008	0.138	5.29	0.03
Long-range 1	0.8 ± 0.8	-0.03 ± 0.04	0.186	3.20	0.10
Long-range 2	0.1 ± 0.2	-0.0004 ± 0.0034	0.001	0.048	0.83

Table A.25: Slope, intercept, linear correlation coefficient, F-value, and p-value for fits of δ_v as a function of range.

A.2.7 Accuracy and precision as a function of SNR

$\delta_v = a_0 + a_1 \mathrm{SNR}$					
	$\mathbf{a_0}$ $(\mathbf{cm\,s^{-1}})$	$\mathbf{a_1}$ $(\mathbf{cm\,s^{-1}/dB})$	**R**	**F**	**p** $(\alpha = 0.01)$
	0.2 ± 0.2	-0.008 ± 0.004	0.317	15.3	4×10^{-4}
$\delta_v = a_0 + a_1 \rho$					
	$\mathbf{a_0}$ $(\mathbf{cm\,s^{-1}})$	$\mathbf{a_1}$ $(\mathbf{cm\,s^{-1}})$	**R**	**F**	**p** $(\alpha = 0.01)$
	150 ± 202	-150 ± 210	0.304	3.07	0.12

Table A.26: Slope, intercept, linear correlation coefficient, F-value, and p-value for fits of δ_v to SNR and ρ in Figures 4.12a and 4.13a.

A.3 Model linear fit parameters

A.3.1 Accuracy and precision as a function of target velocity

$\delta_v = a_0 + a_1 v_{tow}$				
a_0 ($\mathrm{cm\,s^{-1}}$)	a_1 ($\times 10^{-3}$) ($\mathrm{cm\,s^{-1}/cm\,s^{-1}}$)	**R**	**F**	**p** ($\alpha = 0.01$)
0.006 ± 0.076	-2 ± 1	0.511	9.39	0.01
$\sigma_v = a_0 + a_1 v_{tow}$				
a_0 ($\mathrm{cm\,s^{-1}}$)	a_1 ($\times 10^{-3}$) ($\mathrm{cm\,s^{-1}/cm\,s^{-1}}$)	**R**	**F**	**p** ($\alpha = 0.01$)
3.6 ± 0.8	-1 ± 13	0.004	0.033	0.86

Table A.27: Slope, intercept, linear correlation coefficient, F-value, and p-value for linear fits of δ_v and σ_v as a function of towspeed.

A.3.2 Accuracy and precision as a function of target σ_v

$\delta_v = a_0 + a_1 \sigma_{vT}$					
a_0 ($\mathrm{cm\,s^{-1}}$)	a_1 ($\mathrm{cm\,s^{-1}/cm\,s^{-1}}$)	a_2 ($/\mathrm{cm\,s^{-1}}$)	**R**	**F**	**p** ($\alpha = 0.01$)
-0.03 ± 0.09	-0.03 ± 0.02	–	0.026	13.5	3×10^{-4}
$\sigma_v = a_0 + a_1 \sigma_{vT} + a_2 \sigma_{vT}^2$					
a_0 ($\mathrm{cm\,s^{-1}}$)	a_1 ($\mathrm{cm\,s^{-1}/cm\,s^{-1}}$)	a_2 ($/\mathrm{cm\,s^{-1}}$)	**R**	**F**	**p** ($\alpha = 0.01$)
15 ± 1	-0.04 ± 0.70	0.96 ± 0.06	0.952	4950	0

Table A.28: Results of fits of δ_v and σ_v as function of target standard deviation σ_{vT}: fit parameters, linear correlation coefficient, F-value, and p-value.

A.3.3 Accuracy and precision as a function of water velocity

$\delta_v = a_0 + a_1 v_{water}$					
a_0 (cm s^{-1})	a_1 (cm s^{-1}/cm s^{-1})	a_2 (/cm s^{-1})	R	F	p ($\alpha = 0.01$)
0.01 ± 0.12	0.001 ± 0.002	–	0.217	1.94	0.21
$\sigma_v = a_0 + a_1 \lvert v_{fish} - v_{water} \rvert + a_2 \lvert v_{fish} - v_{water} \rvert^2$					
a_0 (cm s^{-1})	a_1 (cm s^{-1}/cm s^{-1})	a_2 (/cm s^{-1})	R	F	p ($\alpha = 0.01$)
2.5 ± 0.2	0.038 ± 0.007	-0.00016 ± 0.00005	0.991	220	8×10^{-5}
$\delta_v = a_0 + a_1 \sigma_{vW}$					
a_0 (cm s^{-1})	a_1 (cm s^{-1}/cm s^{-1})	a_2 (/cm s^{-1})	R	F	p ($\alpha = 0.01$)
-0.09 ± 0.09	-0.5 ± 1.5	–	0.076	0.658	0.44
$\sigma_v = a_0 + a_1 \sigma_{vW}$					
a_0 (cm s^{-1})	a_1 (cm s^{-1}/cm s^{-1})	a_2 (/cm s^{-1})	R	F	p ($\alpha = 0.01$)
3.9 ± 0.1	-1 ± 2	–	0.173	1.67	0.23

Table A.29: Results of fits of δ_v as a function of water velocity v_{water}, σ_v as a function of the absolute difference between fish and water velocity $|v_{fish} - v_{water}|$, and δ_v and σ_v as functions of water velocity standard deviation σ_{vW}: fit parameters, linear correlation coefficient, F-value, and p-value.

A.3.4 Accuracy and precision as a function of lag

$\delta_v = a_0 + a_1 \tau$					
v_{fish}	$a_0 \pm \sigma_{a_0}$ (cm s^{-1})	$a_0 \pm \sigma_{a_0}$ ($\times 10^{-3}$ cm s^{-1}/μs)	R	F	p ($\alpha = 0.01$)
50 cm s^{-1}	-0.04 ± 0.16	-0.01 ± 0.09	0.002	0.0213	0.89
$0.5\Delta v$	-0.2 ± 0.3	0.08 ± 0.13	0.103	1.61	0.22
$\sigma_v = a_0 + a_1 \sigma_{vP}$					
v_{fish}	$a_0 \pm \sigma_{a_0}$ (cm s^{-1})	$a_0 \pm \sigma_{a_0}$ (cm s^{-1}/cm s^{-1})	R	F	p ($\alpha = 0.01$)
50 cm s^{-1}	0.8 ± 0.2	0.61 ± 0.04	0.992	1290	9×10^{-13}
$0.5\Delta v$	-0.03 ± 0.12	0.76 ± 0.02	0.997	5070	0

Table A.30: Slope, intercept, linear correlation coefficient, F-value, and p-value for fits of δ_v and σ_v. For $v_{fish} = 50$ cm s^{-1}, only the data points for $\tau \leq 2688$ μs were fit to avoid the aliased data points.

A.3.5 Accuracy and precision as a function of pulse length and coding

$\delta_v = a_0 + a_1 T$					
Code?	a_0 **(cm s^{-1})**	$a_1(\times 10^{-3})$ **(cm s^{-1}/μs)**	**R**	**F**	**p** ($\alpha = 0.01$)
No code	-0.14 ± 0.07	0.01 ± 0.19	0.001	0.0152	0.90
Code	-0.2 ± 0.5	-1 ± 2	0.249	1.66	0.25
$\sigma_v = a_0 + a_1 T$					
Code?	a_0 **(cm s^{-1})**	$a_1(\times 10^{-3})$ **(cm s^{-1}/μs)**	**R**	**F**	**p** ($\alpha = 0.01$)
No code	2.5 ± 0.3	4.7 ± 0.7	0.923	214	1×10^{-11}
Code	2 ± 1	11 ± 6	0.806	20.7	6×10^{-3}

Table A.31: Slope, intercept, linear correlation coefficient, F-value, and p-value for linear fits of δ_v and σ_v as a function of pulse length for the narrowband model.